Local structure and phase transition in compositionally complex magnetocalorics

Lokale Struktur und Phasenübergang in komplexen magnetokalorischen Legierungen
Zur Erlangung des Grades eines Doktors der Naturwissenschaften (Dr. rer. nat.)
Genehmigte Dissertation von David Koch aus Darmstadt
Tag der Einreichung: 10. Oktober 2023, Tag der Prüfung: 12. Januar 2024

Prof. Dr. Wolfgang Donner: Gutachter 1
PD. Dr. Markus E. Gruner: Gutachter 2
Darmstadt, Technische Universität Darmstadt

TECHNISCHE UNIVERSITÄT DARMSTADT

Materials and Earth Sciences Department
Material Science
Structure Research

Local structure and phase transition in compositionally complex magnetocalorics
Lokale Struktur und Phasenübergang in komplexen magnetokalorischen Legierungen

Accepted doctoral thesis by David Koch

Date of submission: 10. Oktober 2023
Date of thesis defense: 12. Januar 2024

Darmstadt, Technische Universität Darmstadt

Bitte zitieren Sie dieses Dokument als:
URN: urn:nbn:de:tuda-tuprints-265832
URL: http://tuprints.ulb.tu-darmstadt.de/26583
Jahr der Veröffentlichung auf TUprints: 2024

Dieses Dokument wird bereitgestellt von tuprints,
E-Publishing-Service der TU Darmstadt
http://tuprints.ulb.tu-darmstadt.de
tuprints@ulb.tu-darmstadt.de

Erklärungen laut Promotionsordnung

§ 8 Abs. 1 lit. c PromO

Ich versichere hiermit, dass die elektronische Version meiner Dissertation mit der schriftlichen Version übereinstimmt.

§ 8 Abs. 1 lit. d PromO

Ich versichere hiermit, dass zu einem vorherigen Zeitpunkt noch keine Promotion versucht wurde. In diesem Fall sind nähere Angaben über Zeitpunkt, Hochschule, Dissertationsthema und Ergebnis dieses Versuchs mitzuteilen.

§ 9 Abs. 1 PromO

Ich versichere hiermit, dass die vorliegende Dissertation selbstständig und nur unter Verwendung der angegebenen Quellen verfasst wurde.

§ 9 Abs. 2 PromO

Die Arbeit hat bisher noch nicht zu Prüfungszwecken gedient.

Darmstadt, 10. Oktober 2023

D. Koch

Zusammenfassung

Magneto-funktionale Materialien spielen eine entscheidende Rolle in der modernen Gesellschaft bei der Verfolgung von Nachhaltigkeit durch erneuerbare Energiequellen. Unter diesen Materialien bieten Festkörperkühlsysteme auf der Grundlage des magnetokalorischen oder multikalorischen Effekts einen vielversprechenden Ansatz zur Reduzierung des Energieverbrauchs in Kühlungsanwendungen. Die weltweite Nachfrage nach Kühlungslösungen steigt stetig an und betont die Notwendigkeit von energieeffizienten Alternativen zu konventionellen Kompressortechnik. Ni-Mn-Z-basierte Heusler-Legierungen, wobei Z ein Hauptgruppenelement ist, sind aufgrund ihrer martensitischen Phasenübergänge und einzigartigen funktionellen Eigenschaften vielversprechende Kandidaten für die Festkörperkühlung. Diese Übergänge, von einer Hochtemperaturphase (Austenit) zu einer Niedrigtemperaturphase (Martensit), waren seit den 1990er Jahren Gegenstand umfangreicher experimenteller und theoretischer Forschung. Zusätzlich weisen diese Legierungen die charakteristische $L2_1$-Heusler-Struktur auf.

Im Jahr 2015 öffnete die Entdeckung des "all-d-Heusler"-Systems Ni(Co)MnTi, das ohne Hauptgruppenelemente auskommt und ebenfalls über einen einstellbaren magneto-strukturellen Phasenübergang verfügt, neue Forschungsmöglichkeiten. Diese Legierungen, frei von p-Elektronen, warfen Fragen nach den Ursprüngen struktureller Instabilität und Ordnungsmechanismen auf. Im Vergleich zu traditionellen Heusler-Legierungen sind all-d-Heusler-Verbindungen weniger spröde, was eine verbesserte mechanische Stabilität und Bearbeitbarkeit bietet und sie zu vielversprechenden Kandidaten für die Festkörperkühlung macht. Die Aufnahme von Co in höheren Mengen erhöht jedoch die Komplexität der Zusammensetzung und führt zu Herausforderungen bei der Entschlüsselung der chemischen Ordnung in diesen chemisch komplexen magnetokalorischen Legierungen.

Diese Arbeit zielt darauf ab, die chemische Ordnung im Ni-Co-Mn-Ti-System auf langen und kurzen Längenskalen zu untersuchen und ihre Wechselwirkung mit struktureller Instabilität zu erforschen. Das Verständnis dieses Materialsystems hat das Potenzial, zur Entdeckung weiterer Systeme mit martensitischen Phasenübergängen aus ressourcen-unkritischen 3-d-Metallen beizutragen.

Zur Untersuchung der Struktur und des Phasenübergangs dieses komplexen Systems werden fortschrittliche Streutechniken, wie Labor-Röntgenbeugung, Neutronenbeugung und Hochenergie-Röntgenbeugung an einer Synchrotronquelle, eingesetzt. Während die langreichweitige Ordnung in polykristallinen Materialien untersucht werden kann, sind einkristalline Proben unerlässlich, um die kurzreichweitige Ordnung und anisotrope elastische Vorläufer des martensitischen Phasenübergangs zu untersuchen.

Wichtige Erkenntnisse umfassen das Fehlen von langreichweitiger $L2_1$ Ordnung in Ni(Co)MnTi im Gegensatz zu klassischen Heusler-Verbindungen. Die Aufnahme von Co führt zu einer Sensitivität der Legierung auf Änderungen der langreichweitigen Ordnung, was eine Möglichkeit zum Einstellen der magnetischen und strukturellen Phasenübergänge bietet. Darüber hinaus ermöglicht Co die Modifikation der Martensitstrukturen. Diese Modifikation verbessert die Phasenkompatibilität und reduziert die thermische Hysterese.

Darüber hinaus enthüllt die Untersuchung der diffuse Röntgenstreuung in Einkristallen ein komplexes Verhalten der elastischen Moduli für ferromagnetische $Ni_{37}Co_{13}Mn_{33}Ti_{17}$ mit einer am Phasenübergang divergierenden Zener-Anisotropiekonstanten. Ein weiches Phonon im TA_2-Phononenzweig, wie in Ni-Mn-Z, wird nachgewiesen, obwohl keine p-d-Hybridisierung vorhanden ist. Kurzreichweitige $L2_1$ Ordnung kann durch Wärmebehandlung bei niedrigen Temperaturen induziert werden und beeinflusst die Phasenübergangstemperaturen und das weiche Phonon, wodurch die Bedeutung der lokalen Ordnung für die physikalischen Eigenschaften deutlich wird.

Zusammenfassend trägt diese Arbeit zu einem umfassenden Verständnis des Ni-Co-Mn-Ti-Systems bei und beleuchtet seine komplexen Phasenübergänge, die chemische Ordnung und das Zusammenspiel zwischen Magnetismus und Gitterwechselwirkungen. Die gewonnenen Erkenntnisse eröffnen Wege für die Gestaltung verbesserter magnetokalorischer Materialien aus 3-d-Metallen mit potenziellen Anwendungen in der Festkörperkühlung und energieeffizienten Kühlsystemen.

Abstract

Magneto-functional materials play a pivotal role in modern society's pursuit of sustainability through renewable energy sources. Among these materials, solid-state cooling systems based on the magnetocaloric or multicaloric effect offer a promising way for reducing energy consumption in cooling applications. The global demand for cooling solutions is steadily rising, emphasizing the need for energy-efficient alternatives to conventional vapor compression techniques. Ni-Mn-Z-based Heusler alloys, where Z is a main group element, represent a promising candidate for solid-state cooling due to their martensitic phase transitions and unique functional properties. These transitions, from a high-temperature cubic phase (austenite) to a low-symmetry low-temperature phase (martensite), have been the subject of extensive experimental and theoretical research since the 1990s. Additionally, these alloys exhibit the characteristic $L2_1$ atomic structure, which is typical for Heusler alloys.

In 2015, the discovery of the "all-d-Heusler" system Ni(Co)MnTi, which lacks main group elements and features a tunable magneto-structural phase transition, opened new ways for research. These alloys, free of p-electrons, presented intriguing questions regarding the origins of structural instability and ordering mechanisms. Compared to traditional Heusler alloys, all-d-Heusler compounds are less brittle and more ductile, offering improved mechanical stability and machinability, making them promising candidates for solid-state refrigeration.However, the inclusion of Co in substantial amounts adds complexity to the composition, introducing challenges in unraveling the chemical ordering in these compositionally complex magnetocaloric alloys.

This thesis aims to investigate chemical ordering in the Ni-Co-Mn-Ti system at both long and short length scales and explore its interaction with structural instability. Understanding this material system has the potential to lead to the discovery of more systems with martensitic phase transitions composed of abundant 3-d metals. To investigate the structure and phase transition of this complex system, advanced scattering techniques, including laboratory x-ray diffraction, neutron diffraction, and high-energy x-ray diffraction at a synchrotron source, are employed. While long range order can be studied in polycrystalline materials, single crystalline

samples are essential for probing short-range order and anisotropic elastic precursors related to the martensitic phase transition.

Key findings include the absence of long range $L2_1$ order in Ni(Co)MnTi, in contrast to Ni-Mn-Z Heusler compounds. The inclusion of Co introduces sensitivity to the degree of chemical long range order, offering a means to tune phase transitions. Additionally, Co allows to modify the martensite structures. This modification enhances phase compatibility and improves thermal hysteresis.

Furthermore, the investigation of diffuse x-ray scattering in single crystals unveils a complex behavior of the elastic moduli for ferromagnetic $Ni_{37}Co_{13}Mn_{33}Ti_{17}$ with a diverging Zener anisotropy constant approaching the phase transition. A soft mode in the TA_2 phonon branch is found, even though no p-d hybridization is present. Short-range $L2_1$ order can be induced by low-temperature annealing and shows an influence on the phase transition temperatures and soft mode behaviors, emphasizing the significance of local order on physical properties.

In conclusion, this thesis contributes to a comprehensive understanding of the Ni-Co-Mn-Ti system, shedding light on its complex phase transitions, chemical ordering, and the interplay between magnetism and lattice interactions. The insights gained pave the way for the design of improved magnetocaloric materials composed of abundant 3-d metals, with potential applications in energy efficient solid-state refrigeration.

List of Abbreviations

BSE	Backscattering electron
EBSD	Electron backscattering diffraction
bcc	Body centered cubic
DESY	Deutsches Electronen Synchrotron
fcc	Face centered cubic
HEA	High entropy alloys
LRO	Long range order
NPD	neutron powder diffraction
ROI	Region of interest
RSM	Reciprocal space map
SRO	Short range order
TDS	Thermal diffuse scattering
XRD	X-ray diffraction

List of symbols

A	Zener anisotropy ratio
C_{11}, C_{12}, C_{44}, C'	Elastic constants of the austenite phase
c	Concentration
$\frac{e}{a}$	Valence electrons per atom
f	Form factor
F	Structure factor
h k l m	Miller Indices

$\hbar$	Reduced Plancks constant
I	Intensity
k	Reduced wavevector
k_b	Boltzmann constant
L	Bragg Williams long range order parameter
m	Mass
meV	Millielectronvolt
q	Scattering vector
q_{mod}	Modulation wavevector
r	Atomic position
r.l.u.	Reciprocal lattice units
ΔS	Transition entropy change
T	Temperature
ΔT	Adiabatic temperature change
T_c	Curie temperature
T_m	Martensitic phase transition temperature
U	Transformation stretch matrix
Z	Main group element,e.g. Al, Ga, In, Sn, Sb
α	Warren Cowley short range order parameter
β	Monoclinic angle
ϵ	Phonon eigenvector
ω	Phonon frequency
ϕ	Sample rotation angle
$\lambda_{1,2,3}$	Eigenvalues of the transformation stretch matrix

Contents

1 Introduction

1.1 Motivation

Magneto-functional materials are an important part of today's society and are expected to become increasingly important for a sustainable society based on renewable energy sources. Solid-state cooling, based on the magnetocaloric or multicaloric effect, is one promising technique where these materials are used to reduce the total energy consumption spent on cooling applications.[1] The predicted increase in global cooling demand over the next few years intensifies the importance of an energy-efficient alternative to today's commonly used vapor compression techniques. [2] One of the most promising compounds for solid-state cooling are Ni-Mn-Z-based Heusler alloys, which undergo a magneto-structural phase transition, leading to their functional properties. Z is typically a main group element like Al, Ga, In, Sn, or Sb. These martensitic phase transitions, from a cubic high-temperature phase (austenite) to a low-symmetry low-temperature phase (martensite), have been under constant investigation from both experimental and theoretical perspectives since the 1990s and continue to be heavily researched today. [3–23] The lattice instability leading to this phase transition is connected to a certain type of electronic instability originating from p-d hybridization induced by the main group element. These alloys also exhibit the characteristic $L2_1$ atomic structure in the austenite phase, which is typical for Heusler alloys and is therefore also called the "Heusler Structure". In 2015, Wei et al. discovered a new Heusler-like material system that is free from main group elements. [24] The so called „all-d-Heusler "system Ni(Co)MnTi, which also exhibits a tuneable magneto-structural phase transition, has been the subject of increasing research since then. [25–38] As no main group element is used in these alloys, there are also no p-electrons present. Therefore, the origin of the structural instability and the type of ordering was unclear. Compared to the long-known Ni-Mn-Z Heusler alloys, there are some major differences. First, even though the all-d-metal Heusler alloys have a tunable martensitic phase transition, they are less brittle. This significantly enhances mechanical stability under cyclic conditions and improves machinability, making all-d-Heusler compounds promising candidates for solid-state refrigeration. Since a substantial

amount of Co is needed to achieve ferromagnetism in these alloys, the compound becomes more compositionally complex compared to Ni-Mn-Z Heusler alloys. This complexity is enhanced by the fact that the elements used are all 3-d metals and, therefore, do not have large differences in the number of electrons. As a result, the all-d-Heusler alloys are related not only to Ni-Mn-Z Heusler alloys in some sense but also to High entropy alloys (HEA), which have been an emerging research field since 2004. [39–41] These typically consist of five elements in similar ratios and form disordered cubic (fcc + bcc) lattices, where the large configurational entropy stabilizes the cubic phase. Even though there is no long range chemical order, on a shorter length scale, atoms can form preferred local structures. [42] Unlike the all-d-Heusler alloys, cubic HEAs do not exhibit a martensitic phase transition. Recently, hexagonal HEAs with a structural phase transition have also been discovered.[43–45] These compounds contain the semiconductors Ge and Si and undergo a different structural phase transition related to the phase transition in $MM'X$ compounds, which are not part of this thesis. The aim of this thesis is to investigate chemical ordering in the compositionally complex Ni-Co-Mn-Ti system on long and short length scales, and to explore how this ordering interacts with structural instability. Understanding this material system has the potential to lead to the discovery of more material systems with martensitic phase transitions, composed of inexpensive and abundant 3-d metals. Additionally, tuning the chemical order and crystal structures can be used to enhance the thermal hysteresis and adjust the phase transition temperature of both the magnetic and structural phases. This enables optimized alloy design, improving the overall properties of the Ni-Co-Mn-Ti system.

For the investigation of the structure and phase transition of the Ni-Co-Mn-Ti system, advanced scattering techniques are used, which combine laboratory x-ray diffraction with neutron diffraction and high-energy x-ray diffraction at a synchrotron source. While long range order can be investigated in a polycrystalline material, short range order and anisotropic physical properties, such as elastic precursors of the martensitic phase transition, require a single crystalline sample. This allows us to improve our understanding of the physics of the compositionally complex all-d-Heusler system, especially in relation to the main group element-containing Ni-Mn-Z Heusler alloys and the disordered HEA.

1.2 Structure of this Thesis

This thesis is structured as follows: First, a brief introduction to the magnetocaloric effect and relevant materials will be provided. Ni-Mn-Z Heusler alloys will then be discussed in detail, with a focus on the martensitic phase transition and chemical ordering in Heusler alloys. Additionally, the all-d-Heusler with a magneto-structural phase transition and the relevant scattering techniques will be introduced. Since the basics of x-ray diffraction are well-covered in regular studies and textbooks, the focus will explicitly be on the investigation of chemical ordering and diffuse scattering.

The results section begins by describing the investigation of long range structural properties in polycrystalline materials with varying compositions. The primary objective is to elucidate the attainable long range atomic arrangements within all-d-Heusler alloys and explore how these long range ordering patterns interact with the martensitic phase transition. This section will encompass a detailed discussion of chemical ordering phenomena and their influence on both the martensitic and magnetic phase transitions. Furthermore, the examination of compatibility between the austenite and martensite phases will be explored, shedding light on their structural relationship. By presenting these findings, the aim is to provide a comprehensive understanding of the complex interplay between long range atomic ordering, phase transitions, and material compatibility in all-d-Heusler alloys.

The second segment of the results delves into the investigation of single crystals characterized by specific compositions. This exploration involves an in-depth analysis of x-ray diffuse scattering, a technique that offers valuable insights into the local structure via short range order (SRO) diffuse scattering and provides information about elastic precursors via thermal diffuse scattering (TDS). The objective here is to address whether, in addition to long range ordering, local atomic arrangements can take place in these compositionally complex materials. Such local arrangements could have additional implications for influencing phase transitions. Furthermore, this analysis aims to elucidate the underlying elastic mechanisms governing the phase transition, shedding light on these aspects within the context of the well-established Ni-Mn-Z Heusler alloys.

2 State of the Art

2.1 Magnetocaloric effect and materials

The magnetocaloric effect is a solid-state cooling technique that also does not rely on environmentally damaging refrigerants, unlike conventional vapor gas compression cooling devices, and it has the potential to be more energy-efficient than conventional refrigeration techniques.[1] The process relies on the adiabatic magnetization/demagnetization of a magnetocaloric material, which leads to a temperature change in the material. The magnetocaloric cooling cycle is displayed in Figure 2.1 (a). The magnetocaloric material with temperature T is adiabatically magnetized (1). This leads to an alignment of magnetic moments in the material and, therefore, a reduction of the magnetic entropy. Since the process is adiabatic, the total entropy cannot change and the lattice entropy has to increase, leading to an increase in the temperature of the material. After the removal of the excess heat (2), the magnetic field is removed, and the material demagnetizes (3), resulting in the opposite effect it cools down. After absorbing heat (4), the cycle can start again. This effect can be utilized in any heat pump, such as air conditioning, refrigeration, or heat pump heating. The effect has been long known for ultra-low-temperature cooling with paramagnetic salts[46], and is maximized if large magnetic entropy changes, and therefore magnetization change, can be achieved by applying a magnetic field. This is usually the case close to a magnetic phase transition. G.V. Brown then first built a device working close to room temperature in 1976, bringing the magnetocaloric effect closer to everyday applications. [47] This effect was based on Gadolinium as a magnetocaloric material, which has a large magnetocaloric effect due to a Curie temperature T_c close to room temperature. This is a second-order phase transition, schematically shown in Figure 2.1 (b). Gadolinium, as a rare earth metal, is not suitable for large-scale commercial applications due to its low availability and high costs. The investigation of further magnetocaloric materials was enhanced by the discovery of the giant magnetocaloric effect in $Gd_5(Si_2Ge_2)$ by Pecharsky et.al. [48–51] Since this material again relies on Gadolinium, it is still not suitable for large-scale usage. Nevertheless, the large effect does not depend on a T_c close to room temperature but on a first-order phase

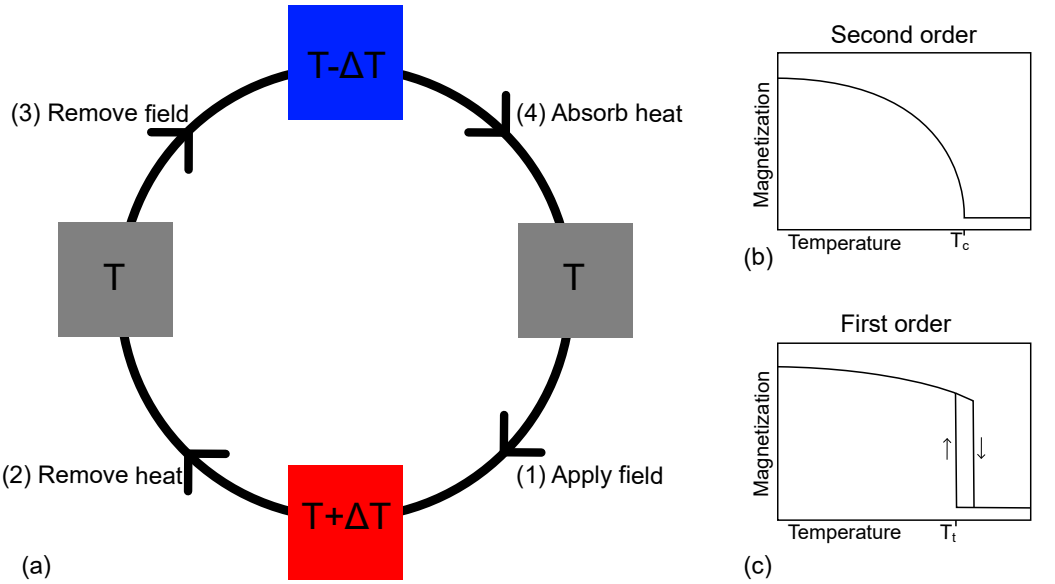

Figure 2.1: (a) Magnetocaloric refrigeration cycle, inspired by [52]. (b) Second order magnetic phase transition with Curie temperature T_c. (c) First order magnetic phase transition with transition temperature T_t during cooling. A thermal hysteresis is observed in this case, with the arrows indicating the cooling and heating parts of the cycle, respectively.

transition with a significant magnetization change. Thus, this material has stimulated research into first-order phase transition materials as potential magnetocaloric materials. A first-order magnetic phase transition is schematically shown in Figure 2.1 (c), characterized by not a continuous change but an abrupt change of magnetization over temperature. Additionally, the first-order phase transition leads to thermal hysteresis. The transition in $Gd_5(Si_2Ge_2)$ not only changes the magnetic properties but is also coupled with a change in the crystal structure from orthorhombic to monoclinic. In the case of a first-order phase transition, the total entropy change ΔS_{tot} does not only consist of the magnetic entropy change but can be described as a sum of different entropy contributions, which can lead to a larger total entropy change.

$$\Delta S_{tot} = \Delta S_m + \Delta S_{lat} + \Delta S_{el} \tag{2.1}$$

Where ΔS_m is the magnetic contribution to the total entropy change, ΔS_{lat} is the lattice contribution, and ΔS_{el} is the electronic contribution. The magnitude and direction of each entropy change can vary for different material systems.

Besides a large magnetocaloric effect, which can be described by an entropy change or adiabatic temperature change, there are different properties that should be met for a material suitable for cyclic performance in a magnetocaloric device. One very important additional

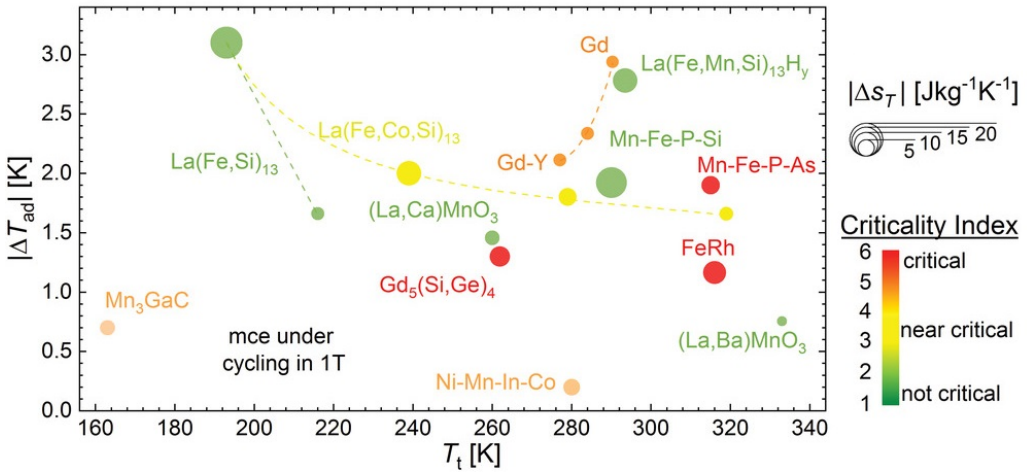

Figure 2.2: Performance of magnetocaloric materials in a cyclic magnetic field of 1 T. The key parameters considered are the adiabatic temperature change, transition entropy change (indicated by the size of the circle), criticality (represented by the color code), and the working range. This figure was adapted from [53] under the terms of the CC-BY 4.0 license(https://creativecommons.org/licenses/by/4.0/).

parameter is the thermal hysteresis, which limits the cyclic performance of the material, since the material does not transform back completely to the initial state after the first cycle. Reducing the thermal hysteresis as much as possible is, therefore, crucial for magnetocaloric materials. Additional factors for the performance of a magnetocaloric effect can include, for example, thermal conductivity for efficient heat transfer, mechanical stability, and low cost of raw materials. Further factors are discussed in more detail in Gottschall et al. [53].

There are several compounds with a first-order phase transition that are investigated in the field of magnetocaloric cooling. They differ in the magnitude of the magnetocaloric effect, the working range, used elements, and more. An overview of known magnetocaloric materials and their performance range under reversible conditions at a magnetic field of 1 T is shown in Figure 2.2. The most promising ones for applications close to room temperature are $La(Fe,Si)_{13}$ and Fe_2P-based compounds. [54] $La(Fe,Si)_{13}$ based materials exhibit an iso-structural itinerant metamagnetic phase transition. [55, 56] They exhibit a large magnetocaloric effect and low thermal hysteresis, but they suffer from poor mechanical stability and corrosion resistance.[57, 58] Fe_2P-based compounds also exhibit excellent magnetocaloric properties due to a structural transition with significant changes in lattice parameters. [59, 60] Compositionally tuning lead to a good cyclic performance due to a low thermal hysteresis and an overall small volume change, which prevents cracking. [61, 62]

Besides these two compounds, Heusler alloys(e.g. Ni-Co-Mn-In in Figure 2.2) are investigated

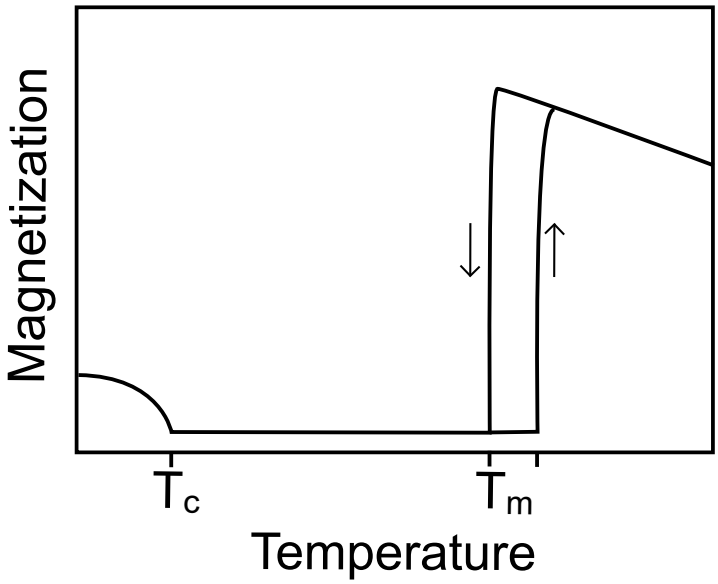

Figure 2.3: Schematic drawing of the magnetization as an order parameter at a martensitic phase transition in Heusler alloys. The arrows indicate cooling and heating process, respectively.

for solid state refrigeration, which will be introduced in more detail in the following section.

2.2 Heusler Alloys

The first "Heusler" alloys were reported by Friedrich Heusler in 1903 and were composed of Cu, Mn, and Al . [63] These alloys exhibited ferromagnetism at room temperature without containing ferromagnetic elements. Later, Otto Heusler described these alloys using four face-centered cubic (fcc) sublattices. [64] Heusler alloys have the general chemical formula X_2YZ, where X and Y are transition metals, and Z is a main group element. Nowadays, Heusler alloys are the subject of research due to a variety of functional properties, such as spin polarization, half-metallicity, or properties linked to a martensitic phase transition to a low-symmetry state. [65] A martensitic phase transition is a diffusionless first order structural phase transition, driven by shear distortions of the lattice. This change in the crystal structure during the martensitic phase transition can be accompanied with a change in magnetization, schematically shown in Figure 2.3. Depending on the composition, the T_c of the high-temperature phase (austenite; not shown), T_c of the low-temperature phase (martensite), and the phase transition temperature can be shifted. While T_c is a second-order phase transition, the martensitic phase transition at T_m is a first-order phase transition and has a significant thermal hysteresis.

This phase transition, often found in Ni-Mn-based Heusler alloys, cannot only be induced

by temperature but also by a magnetic field. This gives rise to a magnetocaloric effect. [14, 15, 66] Since the driving force for the magnetocaloric effect is a difference in magnetization between austenite and martensite, maximizing this is essential for achieving good magnetocaloric performance. The volume and length changes during the phase transition also enable driving the phase transition using mechanical stimuli, such as isostatic pressure or uniaxial stress. This allows the phase transition to be exploited using the elastocaloric effect by applying uniaxial stress [18, 23] or by applying isostatic pressure, which is then referred to as the barocaloric effect. [67] The hysteresis is one major issue for Ni-Mn-based Heusler alloys, as the phase transition can often only be partially induced after the first cycle, drastically reducing the cyclic performance, as shown in Figure 2.2. The performance of a single loop is much higher. Combinations of different stimuli, known as a multicaloric effect, are also possible and can be used to overcome the issue of incomplete phase transitions due to thermal hysteresis. [68, 69] The mechanism behind the giant magnetocaloric effect in Heusler alloys differs from that in the $La(Fe,Si)_{13}$ and Fe_2P compounds mentioned above. The martensitic phase transition leads to an inverse magnetocaloric effect. This means that the material does not heat up when a magnetic field is applied, as shown in Figure 2.1, but rather cools down. After removing the magnetic field, the alloy heats up. In contrast to the classical first-order magnetic phase transition, the low-temperature structure is usually less magnetic than the high-temperature structure. Therefore, the high-temperature phase can be induced by the magnetic field. The inverse magnetocaloric effect originates from the different entropy contributions to the total entropy change of the phase transition in Equation 2.1. For these Heusler systems, ΔS_m and ΔS_{lat} have opposite directions, with $|\Delta S_{lat}| > \Delta S_m$. ΔS_{el} is negligibly small. [17]A large difference in magnetization or magnetic entropy change is important for driving the phase transition with a magnetic field, but it also reduces the total entropy change leading to the cooling effect[19] Besides these caloric effects, these phase transitions can be used in applications such as ferromagnetic shape memory alloys [70] and magnetoresistivity [12].

2.2.1 Martensitic phase transition in Ni-Mn-based Heusler alloys

The martensitic phase transition is the origin of the giant magnetocaloric effect in Ni-Mn-based Heusler alloys. In Heusler alloys, the austenite is cubic, while the martensite has a low-symmetry structure. The martensitic phase transition is based on a shear motion along a specific crystallographic direction. The precursors leading to this phase transition can be explored by an investigation of the phonon modes in the solid. For that, the modes can be split into two regions: the long wave limit and a short wave region, were both factors are discussed in the following parts.

NiMn-based Heusler alloys have a tunable phase transition temperature, which provides a broad temperature window for potential applications. The most investigated material is Ni_2MnGa, where the martensitic phase transition temperature is around 190 K and can be shifted by adjusting the composition. [11, 16]This composition dependence of the phase transition can be explained using the valence electron concentration $\frac{e}{a}$, according to the Hume-Rothery mechanism. The Hume-Rothery mechanism is used to describe the observed crystal structure in metallic compounds by the number of valence electrons in the system.[71] This is also used for HEA to predict which cubic structure is present for a certain composition, were high $\frac{e}{a}$ is favoring a fcc structure and low $\frac{e}{a}$ a bcc structure. [72] For Ni-Mn-Z Heusler alloys, which possess a bcc-like structure, this leads to a linear dependence of the phase transition temperature with $\frac{e}{a}$, were lower $\frac{e}{a}$ is stabilizing the bcc structure and therefore reducing the phase transition temperature. The phase transition takes place when the Fermi surface hits the Brillouin zone boundary, leading to Fermi surface nesting. This electronic instability is leading to anomalies in the phonon modes. For the Ni-Mn-Ga system, the electronic instability is caused by p-d hybrid states between Ga and Ni. [9, 10] For different main group elements, the slope of this linear dependence of the martensitic phase transition temperature with $\frac{e}{a}$ varies, but they all exhibit linear behavior. [11] The phonon anomaly in Ni_2MnGa is visible at the TA_2 phonon branch along [110] direction. This phonon branch softens around 1/3[110], when approaching the phase transition. [73, 74] The magnitude of the softening and the exact position of this anomaly may vary slightly when altering the composition and the main group element.[13, 75] This anomaly can be observed not only with inelastic neutron scattering but also with diffuse x-ray scattering. [3, 4, 76, 77]

Elastic constants in shape memory alloys

Besides the phonon dispersion, elastic properties are used to investigate the precursors of the phase transition. The austenite is cubic and therefore has three independent elastic constants, with the elastic tensor shown in equation 2.2. Additional elastic constants, like C' and the Zener

anisotropy ratio A can be derived from this matrix. In the austenite, the two shear elastic moduli C_{44} and C' are the relevant moduli responsible for the stability of the cubic high-temperature phase. C_{44} represents the resistance against shear motion within the (100) planes and C' the resistance against [-110] shear motion in [110] planes. In bcc shape memory materials, C_{44} is usually large, and C' is small. [78] To describe the interplay between both shear elastic moduli, the Zener anisotropy factor A is used. [79]The anisotropy factor can be used as a fingerprint method to describe the stability of the cubic structures; it increases as the phase transition is approached. [78] Changes in the elastic constants can also be used to investigate the nature of the phase transition. For example, measurements of the elastic constants of Ni_2MnGa revealed an additional phase transition into a pre-martensitic state. Both C_{44} and C' drop around 20 K above the martensitic phase transition, demonstrating that the elastic constants are well-suited as fingerprint methods for investigating the mechanism of the phase transition. [80] Such a phase transition is not a general observation in Ni-Mn-Heusler alloys. Ni-Mn-In, for example, does not exhibit a pre-martensitic transition but shows an increase in anisotropy as expected. [75]

$$C_{ij} = \begin{pmatrix} C_{11} & C_{12} & C_{12} & 0 & 0 & 0 \\ C_{12} & C_{11} & C_{12} & 0 & 0 & 0 \\ C_{12} & C_{12} & C_{11} & 0 & 0 & 0 \\ 0 & 0 & 0 & C_{44} & 0 & 0 \\ 0 & 0 & 0 & 0 & C_{44} & 0 \\ 0 & 0 & 0 & 0 & 0 & C_{44} \end{pmatrix} \tag{2.2}$$

$$C' = \frac{C_{11} - C_{12}}{2} \tag{2.3}$$

$$A = \frac{C_{44}}{C'} \tag{2.4}$$

The elastic constants are related to the initial slope of the phonon dispersion at the Γ point. This slope is equal to the velocity of sound v_s in a certain direction, where the C' value corresponds to the TA_2 phonon branch, as shown in Equation 2.5, with the phonon frequency ω, phonon wavevector k the density ρ. [81, 82]

$$v_s = \frac{\omega}{k} = \sqrt{\frac{C'}{\rho}} \tag{2.5}$$

2.2.2 Ordering in Heusler alloys

The high-temperature phase of Heusler compounds typically has a body-centered cubic (bcc)-like atomic arrangement, composed of four interpenetrating face-centered cubic (fcc) lattices. The atomic positions are as follows: $A(0,0,0)$, $B(\frac{1}{4},\frac{1}{4},\frac{1}{4})$, $C(\frac{1}{2},\frac{1}{2},\frac{1}{2})$, and $D(\frac{3}{4},\frac{3}{4},\frac{3}{4})$. Depending on the composition and thermal history of the sample, different atomic ordering schemes are known, resulting in different symmetries of the crystalline lattice. The most common ones are depicted in Figure 2.4. In (a), the structure has only one distinct lattice site (all positions are equivalent), which is then equivalent to the bcc structure, also known as the A2 structure according to the Strukturbericht designation or tungsten structure. In (b), the B2 or CsCl-superstructure is shown, where two distinct lattice sites ($A+C; B+D$ equivalent) are present. The typical Heusler structure is shown in (c), where three different lattice sites with a doubling of the unit cell parameter ($B+D$ equivalent) are present. This structure is known as the $L2_1$ structure and is the typical ground state for most Heusler compounds. If the alloy contains more than three elements, even more complex ordering can occur, as shown in (d) with four different lattice sites (no equivalent position). The investigation of different ordering schemes can be conducted through a diffraction experiment, as explained in more detail in section 3.

All known Ni-Mn-Heusler alloy systems that exhibit a martensitic phase transition show an A2, B2, and $L2_1$ ordering sequence after cooling from the melt. Sometimes, the B2 structure remains stable up to the melting temperature, suppressing the A2 phase.[20]

While the characteristic ground-state structure for Heusler compounds is the $L2_1$ ordering, some degree of disorder can be induced by quenching from a specific temperature. For example, in Ni-Mn-Al alloys, the $L2_1$ transition temperature is quite low, leading to a suppression of the order. [20] However, this order can be restored through proper heat treatment. [5] The B2 ordering in Ni-Mn-Al leads to an antiferromagnetic austenite instead of a ferromagnetic austenite, underscoring the significance of the ordering scheme for the magnetic properties of Heusler alloys. [6, 83] In Ni-Mn-In alloys, which have a higher $B2 - L2_1$ transition temperature, it is often observed that $L2_1$ ordering cannot be completely avoided during quenching. [22] For these Heusler systems, it is known that chemical disorder influences the electronic structure and, consequently, the martensitic phase transition. [21, 65]

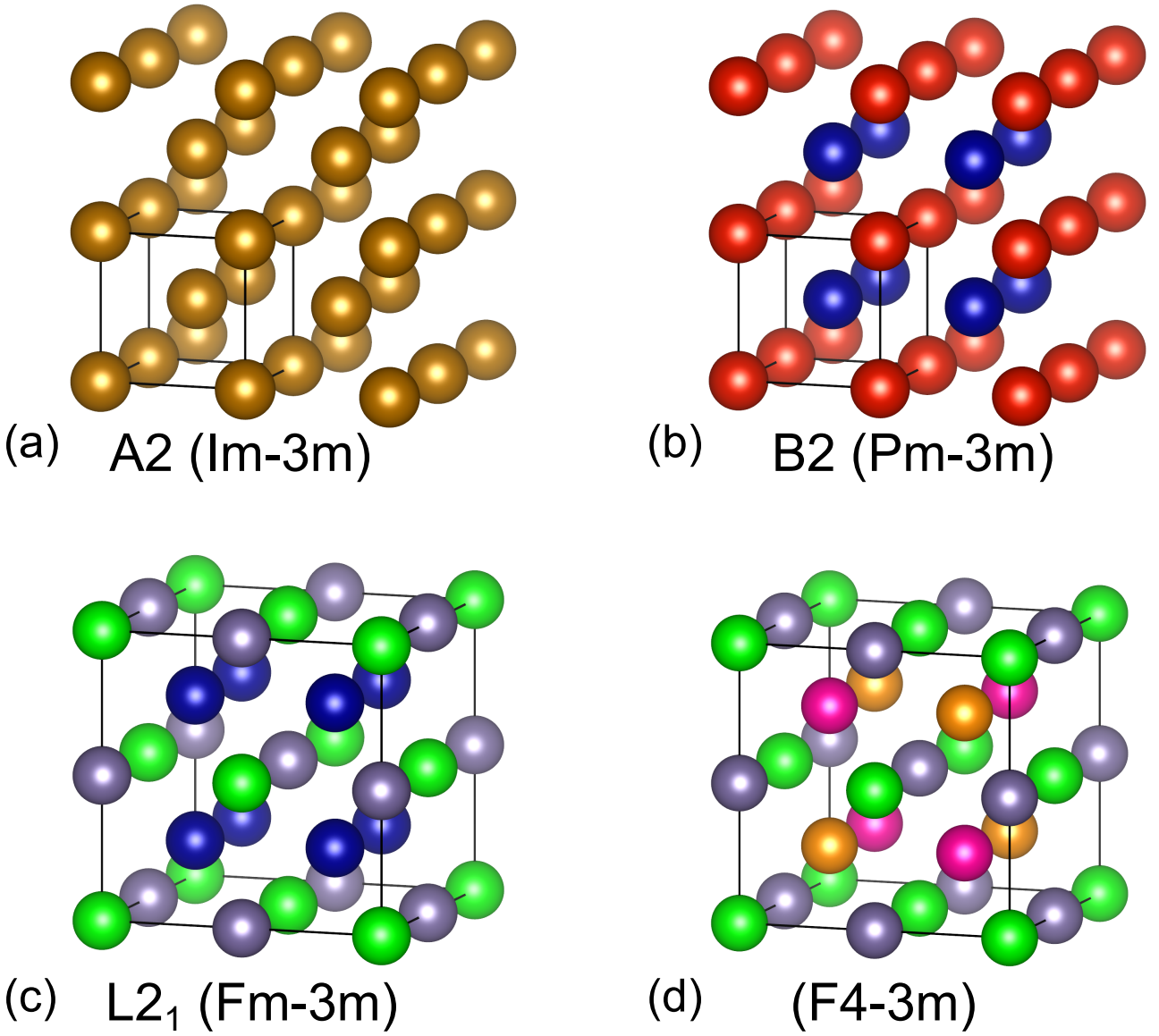

Figure 2.4: Common superstructures for Heusler compounds, each marked with a corresponding unit cell outlined by black lines. (a) A2 or tungsten structure with the space group $Im\bar{3}m$. (b) B2 or CsCl structure with the space group $Im\bar{3}m$. (c) $L2_1$ or Heusler structure with the space group $Fm\bar{3}m$. (d) Superstructure with four distinct lattice sites and space group $F4\bar{3}m$. This structure does not have a nomenclature according to the Strukturbericht designation but is also known as LiMgPdSn structure[65].

2.2.3 Martensite structures

The phonon softening in the austenite leads to diverse and complex crystal structures in the martensite, which can vary depending on used elements and exact compositions and phase transition temperatures. The simplest structure is the $L1_0$ tetragonal martensite. In Figure 2.5 the relationship between the cubic $L2_1$ austenite unit cell and the $L1_0$ unit cell of the martensite is shown. The $L1_0$ martensite is the ground state of the Ni-Mn-based Heusler alloys with martensitic phase transition. [84]

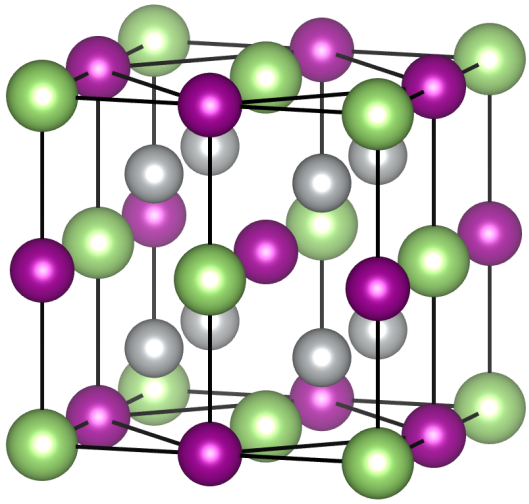

Figure 2.5: Cubic $L2_1$ unit cell and relation to the unmodulated tetragonal $L1_0$ unit cell.

However, due to kinetic restrictions at low temperatures, it is experimentally only found for high transition temperatures. At lower transition temperatures, modulated structures are observed, which can additionally be orthorhombic or monoclinic distorted. This modulation involves a periodic displacement of atomic positions along the austenite [110] direction with a displacement in the [-110] direction. It is initiated by the soft phonon modes of the austenite mode close to the martensitic phase transition. The exact atomic arrangement in these modulated structures can be complex. To describe such a complex structure, the concept of adaptive martensite can be employed. [85, 86] Within this concept, the martensite is modeled using a nanotwinned local structure of unmodulated (e.g., tetragonal $L1_0$) building blocks. This nanotwinning is visualized in Figure 2.6.

However, to describe a diffraction pattern of such a complex modulated structure, the use of a model based on unit cells is extremely beneficial, as it significantly reduces the number of free parameters. To achieve this, incommensurate crystallography can be employed [88]. Within this approach, a superspace model is used. A structure in superspace is described by a conventional

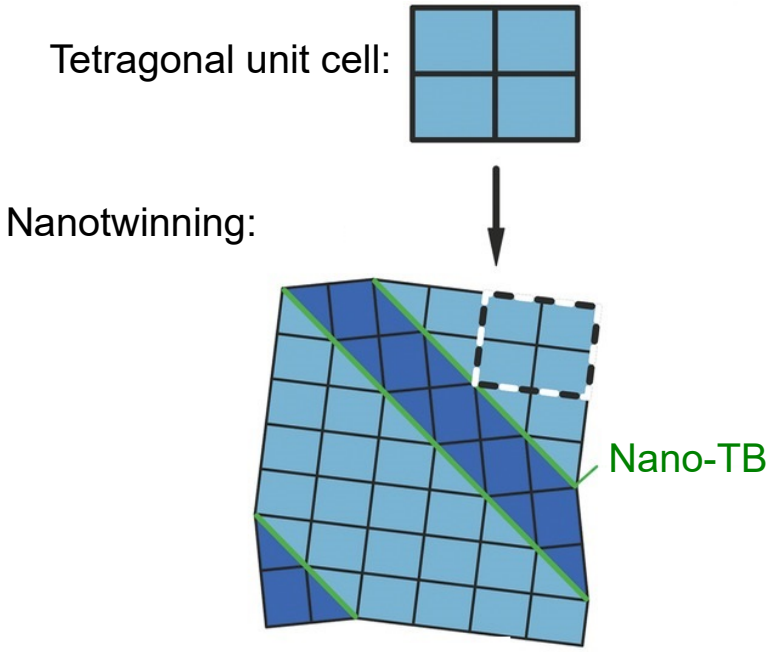

Figure 2.6: Schematic drawing of the building process of a nanotwinned structure out of tetragonal building blocks, adapted from [87] under the terms of the CC-BY 4.0 license(https://creativecommons.org/licenses/by/4.0/).

unit cell plus a periodic modulation of the structure in d dimensions, resulting in a (3+d)-dimensional crystallography. This modulation can involve atomic occupancy and/or atomic displacement. For a modulated structure with a modulation in one direction, this leads to four, instead of three, Miller indices to describe a reflection (hklm), where m $\neq$0 indicates reflections originating purely from modulation. A detailed textbook covering all the fundamentals of incommensurate crystallography is provided in [89]. To evaluate such modulated structures, the most commonly used software is the JANA software suite, specialized in applying classical crystallography tools to modulated crystal structures. [90] In the case of Heusler martensite structures, a superspace approach with modulation along the c direction is often employed. [23, 69, 91–93] Instead of using a nanotwin description for atomic positions, sinusoidal waves are commonly utilized. This choice is practical because they are easy to implement, and a more detailed description of atomic displacement is often challenging due to the minimal impact on the diffraction pattern. Depending on the length of the modulation vector, different nomenclatures are used. The most common martensites are described as "5M" or "7M" structures, indicating that the modulation repeats itself after five or seven unit cells, respectively. However, the modulation wavelength does not need to be restricted to multiples of a unit cell. In such cases, the modulation is called incommensurate (IC); otherwise, it is termed commensurate. An

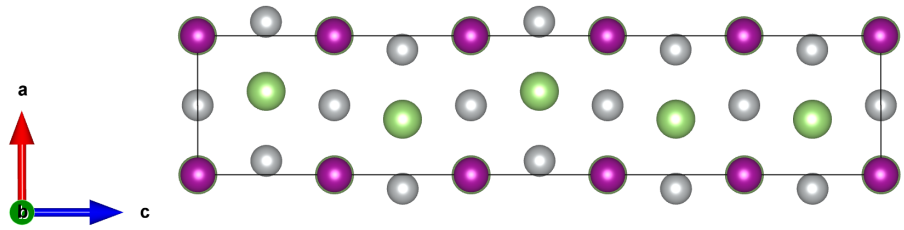

Figure 2.7: A-C plane of a ”4O” modulated structure, visualized using the JANA2006 software package and VESTA[90, 94].

example of an orthorhombic martensite with a periodicity of four unit cells is labeled as "4O", as shown in Figure 2.7. It's important to note that the naming of martensite structures is not consistently standardized.

2.2.4 Compatibility

The martensite structure is not only of fundamental interest but also has direct effects on the physical properties of the alloy, especially on the hysteresis. A low hysteresis of the martensitic phase transition requires low interface strain between the austenite and martensite to minimize the energy barrier of the phase transition, leading to hysteresis. The transformation between the austenite unit cell and the martensite unit cell can be described using a transformation matrix F, a rotation matrix R, and a stretch matrix U. [95]

$$F = RU \tag{2.6}$$

The compatibility of both phases is given by the middle eigenvalue of U, λ_2, which should be as close to 1 as possible, which indicates that the plane at the interface has low stress. A good geometric compatibility allows for a low thermal hysteresis, beneficial for cyclic applications.[95, 96] The geometric compatibility is one major factor for the hysteresis in Ni-Mn-based Heusler alloys, used several times in literature to minimize hysteresis. [97–100] Nevertheless, it is not the only relevant factor. e.g. magnetism, microstructures and homogeneity can play an important role in the hysteresis as well. [54] For the cubic to monoclinic phase transition in Heusler alloys the U matrix can be defined as follows, according to [98].

$$U = \begin{pmatrix} \tau & \rho & 0 \\ \rho & \sigma & 0 \\ 0 & 0 & \xi \end{pmatrix} \tag{2.7}$$

The matrix elements are calculated using the lattice parameter of the austenite unit cell, denoted as a_0, and the unit parameters of the average martensite cell, which are represented as a, b, c, β. The reduced parameters for the calculation are $\alpha = \frac{\sqrt{2}a}{a_0}$ and $\gamma = \frac{\sqrt{2}c}{a_0}$.

$$\xi = \frac{b}{a_0} \tag{2.8}$$

$$\tau = \frac{\alpha^2 + \gamma^2 + 2\alpha\gamma(sin\beta - cos\beta)}{2\sqrt{\alpha^2 + \gamma^2 + 2\alpha\gamma sin\beta}} \tag{2.9}$$

$$\rho = \frac{\alpha^2 + \gamma^2 + 2\alpha\gamma(sin\beta + cos\beta)}{2\sqrt{\alpha^2 + \gamma^2 + 2\alpha\gamma sin\beta}} \tag{2.10}$$

$$\sigma = \frac{\alpha^2 - \gamma^2}{2\sqrt{\alpha^2 + \gamma^2 + 2\alpha\gamma sin\beta}} \tag{2.11}$$

Since 2015 it is also known that the main group element can be substituted with the d-metal Titanium. These alloys and especially the Ti-containing all-d-Heusler alloys will be discussed in more detail in the next section.

2.2.5 all-d-Heusler alloys

Since 2015, Wei et al. introduced the concept of the "all-d-Heusler" alloys, which are obtained by substituting the classical main group element in Ni-Mn-Z alloys by Titanium.[24] This leads to a tunable martensitic phase transition, where the same electronic Hume-Rothery behavior with $\frac{e}{a}$ is observed as in Ni-Mn-Z Heusler alloys. [25] The cubic austenite of these all-d-Heusler alloys is usually paramagnetic, but a ferromagnetic austenite can be achieved by introducing 12-17 at.% Co into the alloy [24, 27]. One advantage of all-d-Heusler alloys is that they have inherently better mechanical properties than Ni-Mn-Z Heusler alloys, where weak mechanical properties and brittleness are one major drawback. This improved mechanical behavior of all-d-Heuslers is attributed to a different type of bonding, as d-d hybridization is introduced instead of p-d hybridization. The improved mechanical properties, along with good tunability of the phase transition and relatively large volume changes during the martensitic phase transition, are especially beneficial for cyclic applications or mechanical stimuli, such as baro, elasto, or multicaloric cooling .[24, 25, 27–30, 37, 101] Synthesis of all-d-Heusler alloys by now is done via arc melting, melt spinning, or directional solidification. By the latter, only strongly textured samples are obtained; no single crystals are reported to the authors' knowledge. [31–33, 102] Chemical ordering in all-d-Heusler alloys is not fully understood, which has several reasons. Since more than 10 at.% Co is usually present in these alloys, four instead of three elements

are present, which could lead to more complex ordering schemes (e.g., no equivalent positions; $F\bar{4}3m$). Co is also used in Ni-Mn-Z Heusler alloys to enhance ferromagnetism, but usually not to more than 5 at.%. Due to its low content, ordering effects related to Co are often neglected, with the assumption that it occupies the Ni site. Consequently, it remains unknown which ordering schemes occur experimentally and how they affect the electronic structure and lattice instability leading to the martensitic transition.

Since for Ni_2MnGa, it is known that the instability is caused by p-d hybrid states between Ni and Ga[9, 10], some questions arise for the Ti-containing all-d-Heusler in respect to the Ni-Mn-Z Heusler alloys . By now, it is unclear how the hybridization exactly looks like and what electronic states cause the electronic instability leading to martensitic phase transition. Therefore, it is also unknown if the instability/phonon softening is the same as for the Ni-Mn-Z Heusler alloys. Within this thesis, these new and unknown aspects of the all-d-Heusler should be tackled. On one side, the experimentally obtained ordering and the effect on the magnetic properties and martensitic phase transition are investigated. In addition to the long range chemical ordering, possible short range ordering is investigated, which is also known to have an influence on magnetofunctional properties; for example, in Fe-Ga, it has a strong influence on the magnetostrictive properties. [103–105] On the other side, the elastic/vibrational properties are investigated, providing insights into the phase transition, also in relation to Ni-Mn-Z Heusler alloys.

3 Diffraction methods

X-ray diffraction (XRD) is a very common technique to study the atomic structure of crystalline or amorphous materials, providing insights into atomic positions, distances, and symmetries. This makes x-ray diffraction especially powerful for investigating structural phase transitions, like the first-order phase transitions in magnetocaloric materials discussed in Chapter 2.1. A brief summary of important concepts is given here. Detailed textbooks covering the fundamentals of x-ray diffraction are provided in [106, 107]. While the average structure, e.g., Long range order (LRO) (see Section 3.1), can be investigated using Bragg reflections, which produce a sharp signal in the experiment, the local structure (static or dynamic) can be investigated using diffuse scattering, leading to broad features with relatively weak intensities, as discussed in Section 3.2.

The fundamental equation of x-ray diffraction is the Bragg equation, which connects the distance between lattice planes d to the position of the scattering angle θ. n is an integer order of the reflection, and λ the wavelength used.

$$n\lambda = 2dsin(\theta) \tag{3.1}$$

In a Laue experiment, polychromatic radiation is used, otherwise the radiation is monochromatic with a wavelength between $\sim 1 \cdot 10^{-11} - 2 \cdot 10^{-10} m$ or $0.1 - 2$ Å. The intensity of a certain Bragg reflection depends on different factors, e.g. Lorentz-factor polarization or thermal vibrations. The most important factor is the structure factor F_{hkl} with:

$$F_{hkl} = \sum_i f_i \cdot exp^{2\pi i(hx_i + ky_i + lz_i)} \tag{3.2}$$

Here, h, k, and l are the Miller indices of the Bragg reflection, while x, y, and z represent the atomic positions within the unit cell, and f_i stands for the atomic scattering factor of atom i. If the structure factor is 0, the reflection is considered "forbidden", leading to specific extinction rules that depend on the symmetry. For example, in the body-centered cubic structure, as shown in Figure 2.4 (a), only reflections that satisfy the condition h + k + l = 2n are allowed.

The intensity I of the Bragg reflection is then calculated as follows:

$$I_{hkl} \sim |F_{hkl}|^2 \tag{3.3}$$

X-ray tubes and synchrotrons are the most common sources of x-rays. X-ray tubes are typically used in laboratory environments and rely on the characteristic radiation of specific anode materials, such as Cu or Mo. Synchrotron x-ray sources, utilizing bending magnets, wigglers, or undulators, provide tunable x-ray energy with high brilliance, enabling more sophisticated experiments.

For polycrystalline samples, Rietveld refinement can be employed, which is a mathematical description of the complete diffractogram. [108] This refinement process includes factors such as profile parameters, background, multiplicity, lattice parameters, and geometric factors of the diffraction setup. These parameters can be refined using a least-squares algorithm. Various software packages are available for performing Rietveld refinement. [90, 109]

3.1 Long Range Order

A thermodynamic description of the long range order/disorder transition, such as that between the different states shown in Figure 2.4, can be accomplished using the Bragg-Williams or Mean Field model. [110] Within this model, the energy of mixing for a binary compound with species A and B is described as follows:

$$E_{mix} = \frac{e_{AA} + e_{BB} - 2e_{AB}}{4} \tag{3.4}$$

Here, e_{AA} and e_{BB} represent the energies for AA and BB pairs, while e_{AB} represents the energy for the mixed pair of A and B. If the alloy exhibits an ordering tendency, E_{mix} is negative. However, at high temperatures, the alloy will form a random solid solution due to configurational entropy. To quantify the degree of ordering, the Bragg-Williams long range order Parameter, denoted as L, can be used.

$$L = \frac{R - W}{N/2} \tag{3.5}$$

Here, R counts the atoms on the right (ordered) sites, and W represents the atoms at the wrong site, with N being the total number of sites. In a perfectly ordered state, the order parameter is L=1, while in a completely random state, L=0. For an alloy that tends to order, there exists a critical ordering temperature below which long range ordering increases. This behavior is comparable to the second-order phase transition shown in Figure 2.1 (b). Since this

model only considers the average position of an atom and doesn't account for cluster effects, it is also referred to as the point approximation.
The evaluation of the degree of long range chemical order can be achieved through a diffraction experiment. In the case of binary compositions or compositions with multiple elements, it is possible to distinguish between reflections that do not change with the degree of chemical order and reflections that arise solely due to chemical order. These reflections are referred to as fundamental reflections and superstructure reflections, respectively. To determine the intensity of a reflection, one must consider the structure factor specific to that reflection, which differs for fundamental and superstructure reflections. The intensity of superstructure reflections typically arises from differences in the atomic scattering factor f of the relevant species, while the intensity of fundamental reflections is the sum of the atomic scattering factors. This discussion pertains to the Heusler structure $L2_1$, as shown in Figure 2.4 (c). The Heusler structure belongs to the space group $Fm\overline{3}m$ with the following Wyckoff positions: 4a(0,0,0), 4b(0.5,0.5,0.5), and 8c(0.25, 0.25, 0.25). The intensity of diffraction peaks depends on the combination of h, k, and l indices, which, in turn, is related to different scattering factors within the unit cell. These relationships are summarized in Table 3.1. For simplicity, the Miller indices of the $L2_1$ structure are used. As indicated in Figure 2.4, the A2 and B2 structures have lattice parameters half the size of the $L2_1$ structure. Table 3.1 illustrates that reflections with odd h, k, l indices, such as the (111) reflection, are unique to the $L2_1$ structure, and the corresponding structure factor arises from the difference in atomic scattering factors of the A and B sites. Conversely, the typical reflections of the B2 structure, such as the (200) reflection, have a structure factor associated with the difference between the C-site and the (A+B)-site, while fundamental reflections have a structure factor that is the sum of the scattering factors of all positions.

Accurate determination of the intensities of superstructure reflections and fundamental reflections is essential for determining the long range order parameter. Therefore, optimizing the contrasts in the scattering factors between all used elements is crucial to maximize the theoretically possible intensities of the superstructure reflections. This optimization can be achieved by adjusting the wavelength close to absorption edges or by employing neutron diffraction.

Atomic scattering factors

The elements utilized within this thesis are Ni, Co, Mn, and Ti. The scattering factors for x-rays are primarily related to the number of electrons in the atoms and exhibit variations near their absorption edges, but they remain nearly energy-independent far from the absorption edges, resulting in significant contrast differences between elements when using Cu or Mo radiation, as

Table 3.1: Structure Factors of different reflections within the Heusler Structure. [111] In the last column the Strukturbericht designation of the structures in Figure 2.4(a),(b) and (c) are shown, where the respective reflection appears. The four-element structure in Figure 2.4 (d) has the same allowed reflections as the $L2_1$ structure and is for clarity omitted here.

Reflection	Structure Factor	Example	Structure
h,k,l all odd	$4(f_a - f_b)$	(111)	$L2_1$
(h+k+l)/2=2n+1	$4(2f_c - (f_a + f_b))$	(200)	B2, $L2_1$
(h+k+l)/2=2n	$4(2f_c + f_a + f_b)$	(220)	$A2$, B2, $L2_1$

Table 3.2: X-ray atomic scattering factor[112] and Neutron scattering length[113] for the elements Ni, Co, Mn Ti.

Element	f1(Cu Kalpha)[e]	f1(Mo Kalpha)[e]	f(neutron)[fm]
Ti	22.2384	22.2929	-3.438
Mn	24.4617	25.3486	-3.73
Co	24.6213	27.3568	2.49
Ni	25.0030	28.3564	10.3

indicated by Table 3.2. Additionally, x-ray scattering factors decrease with increasing scattering vector.

In contrast, when using neutron diffraction, the atomic scattering factor is not dependent on the number of electrons. Instead, it varies more randomly from element to element, differs between isotopes and can be negative as well. This property makes neutron diffraction particularly valuable for distinguishing neighboring elements compared to x-ray scattering. Another advantage of neutrons is that the scattering factor does not decrease with increasing scattering vector, leading to higher intensity at large angles. As a result, neutron diffraction enables the measurement of more superstructure reflections.

The decrease of the form factor for x-rays is modeled using a series of Gaussian functions, where the parameters are tabulated in the international tables of crystallography. [114]

$$f = A_1 e^{-B_1(\frac{q}{4\pi})^2} + A_2 e^{-B_2(\frac{q}{4\pi})^2} + A_3 e^{-B_3(\frac{q}{4\pi})^2} + A_4 e^{-B_4(\frac{q}{4\pi})^2} + C \tag{3.6}$$

3.2 Diffuse Scattering

In general, a diffraction pattern can be divided into two parts: Bragg scattering and diffuse scattering. Diffuse scattering arises from all kinds of deviations from a perfectly long range ordered crystal structure, such as substitutional(Short range order (SRO)) or displacive(Thermal diffuse scattering (TDS), size effect, Huang) disorder. [115]

$$I_{tot} = I_{Bragg} + I_{diffuse} \tag{3.7}$$

$$I_{diffuse} = I_{d1} + I_{d2} + I_{d3} + ... \tag{3.8}$$

The diffuse scattering itself can be described as a sum of single-origin diffuse scattering. The most common types of diffuse scattering are SRO, size effect, Huang scattering, and TDS. Huang scattering and size effect diffuse scattering originate from displacive disorder induced by point defects and differences in atomic sizes, respectively, but these are not discussed further within this thesis. The contributions of TDS and SRO are discussed in more detail in the next paragraphs.

3.2.1 Short Range Order

In real physical examples, correlations between elements can also exist above the critical temperature for long range ordering. The thermodynamics of these correlations can be described by a pair approximation, as explained in detail in textbooks such as [110], which leads to correlations above the critical LRO ordering temperature. In the field of magneto-functional materials, this phenomenon has been well investigated, as seen in Fe-rich FeGa alloys [103–105]. These materials exhibit a significant magnetostriction, which depends on the degree of short range order. The development of ordered domains over 3-5 nm in size leads to a substantial reduction in magnetostriction, with the domain size depending on the thermal history and composition of the sample [103]. A binary system is ideal to discuss the effects of SRO. The correlations between two elements can be described by the Warren-Cowley short range order parameter α_{ij}. [106, 116]

$$\alpha_{ij} = 1 - \frac{P_{ij}}{c_j} \tag{3.9}$$

Here, P^{ij}_{lmn} represents the probability of finding atom j at a distance vector r from atom i, and c_j is the concentration of atom j. Depending on the sign of α, the correlation can be

positive, negative, or uncorrelated.

$$\alpha_{ij} > 0 \rightarrow \text{even neighbors favored, clustering} \tag{3.10}$$

$$\alpha_{ij} = 0 \rightarrow \text{random} \tag{3.11}$$

$$\alpha_{ij} < 0 \rightarrow \text{uneven neighbors favored, ordering} \tag{3.12}$$

The SRO diffuse scattering for a binary compound with the elements i and j can be described as shown in equation 3.13. [106] The diffuse intensity depends on the difference between the scattering factors f of both elements, their corresponding concentrations c, the scattering vector q, the position of the corresponding atom r_{ij}, and the Warren-Cowley SRO parameter as shown in Equation 3.9. In the case of only SRO, it is assumed that two atoms far from each other are purely uncorrelated, so $\alpha_{ij} = 0$. For shorter distances, SRO leads to a modulation of the intensity depending on the α values. In the special case of no correlation at all, α would be 0 for all $r_{ij} \neq 0$, and $\alpha = 1$ for $r = 0$. The equation would then reduce to equation 3.14. This is also referred to as Laue monotonic scattering, and it results in a continuous background that decreases at higher q-values for x-rays due to a reduction in the scattering factor

$$I_{SRO} = N \sum_{ij} c_i c_j (f_i - f_j)^2 \alpha_{ij} cos(q \cdot r_{ij})) \tag{3.13}$$

$$I_{Laue} = N \cdot c_i c_j (f_i - f_j)^2 \tag{3.14}$$

In the case of B2 short range ordering in a binary compound, this would result in modulations of the diffuse intensity on the spots in reciprocal space, where one would typically expect superstructure reflections for long range order. The distinctions between B2 SRO, LRO, and Laue monotonic scattering ($A2$ structure) are illustrated in Figure 3.1.

Long range chemical ordering leads to the emergence of additional superstructure peaks, with their intensity dependent on the structure factor, which is associated with differences in atomic scattering factors. Conversely, short range ordering results in diffuse scattering at the positions where potential superstructure reflections might occur.

In the case of a multi-component system, calculations can become more complex. This complexity is currently under investigation in the field of high-entropy alloys, where experimental difficulties have driven research toward theoretical approaches. However, SRO has already been observed experimentally in high-entropy alloys [42]. High-entropy alloys consist of five elements

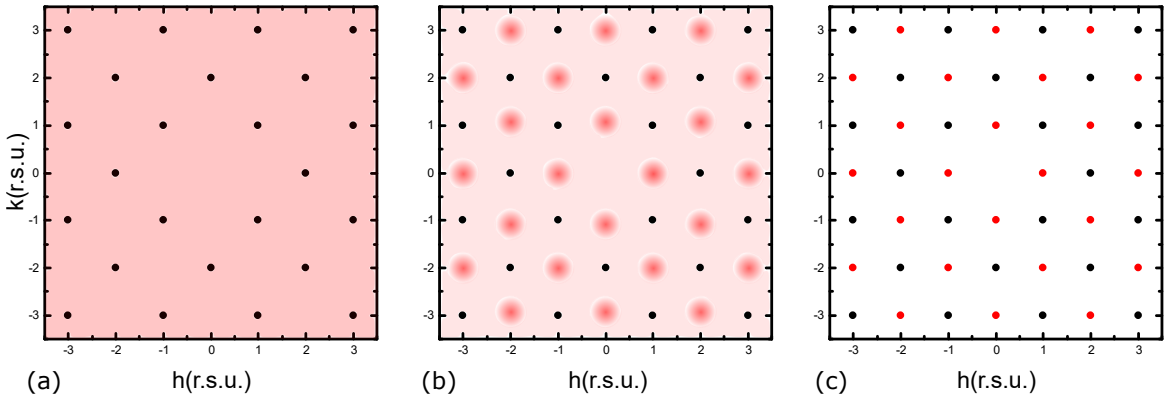

Figure 3.1: Schematic drawings of the h-k plane of a binary alloy with body centered atomic arrangement with(a) $A2$ structure and Laue monotonic scattering (b) B2 SRO (c) B2 LRO. Fundamental reflections are marked in black and ordering in red. The decrease of atomic scattering factor to higher q is omitted for clarity.

in similar concentrations. [39, 40] Due to the high configurational entropy, long range chemical ordering is suppressed, but short range ordering between different elements is proposed by theory. To completely describe SRO in such systems, correlations between all elements must be taken into consideration. [117–119]

3.2.2 Thermal Diffuse Scattering

Thermal diffuse scattering (TDS) arises from thermal vibrations, which appear static on the timescale of an x-ray, giving rise to a "static" displacive disorder. While SRO diffuse scattering typically occurs between Bragg reflections, TDS is centered around Bragg reflections. Studies on thermal diffuse scattering and its connection to lattice dynamics have a long history. Ratios of elastic constants were already determined using TDS in the 1950s and 1960s. [120] The very first phonon dispersion curves were also constructed from TDS data. [121]

However, with the availability of inelastic neutron scattering in the 1960s, the use of diffuse x-ray scattering to study lattice dynamics became less popular due to longer measurement times and more complex analysis. In the 2000s, there was a resurgence of interest in TDS. Modern synchrotron sources and area detectors significantly increased data acquisition rates, making experiments faster and more feasible. [122, 123] TDS measurements have also been used to study the magnetic shape memory alloy Ni-Mn-Ga. [76, 77, 124]

However, there were limitations related to count rates and readout noise of the detectors used. Bragg spots needed to be shielded to avoid detector damage and blooming artifacts in the data while still obtaining sufficient statistics in the diffuse scattering.

One major advancement that addresses this issue is the development of readout-noise-free

hybrid photon counting area detectors with fast or continuous readout, such as the Pilatus3 and Eiger2 detectors. [125–128] These detectors make it possible to measure weak TDS signals even near strong Bragg peaks, enabling experiments even with laboratory diffractometers. [129]

Modelling of TDS

The thermal vibrations in a solid are described via phonon modes, which can also be used to describe the diffuse scattering that arises from these thermal vibrations. The TDS intensity of a one-phonon process can be written as follows [127, 129]:

$$I_{TDS}(q) = \frac{\hbar N I_{in}}{2} \sum_{\nu} \frac{coth\left(\frac{\hbar\omega_{k,\nu}}{2k_bT}\right)}{\omega_{k,\nu}} \left|F_\nu(q)\right|^2 \tag{3.15}$$

With:

$$F_\nu(q) = \sum_s \frac{f_s(q)}{m_s^{0.5}} e^{-W_{s,q}} (q\epsilon_{q,\nu,s}) e^{-iqr_s} \tag{3.16}$$

F_ν is also referred to as the one-phonon structure factor. N represents the number of unit cells, I_{in} stands for the intensity of the incident beam, q for the total scattering vector and $coth\left(\frac{\hbar\omega_{k,\nu}}{2k_bT}\right)$ describes the phonon population using Bose-Einstein statistics, with the Boltzmann constant k_b and temperature T. Here, ω and ϵ denote the phonon eigenfrequency and eigenvector of the phonon branch ν at the reduced wavevector k. Additionally, f represents the form factor, m represents the mass, and r represents the position of the atom s in the unit cell. Higher-order phonon processes can also become important, especially at high temperatures. A comprehensive derivation of the TDS formalism, including higher-order processes, can be found in Xu et al. [123].

For small q-values, single-phonon scattering of acoustic phonons is the relevant process. For $\hbar\omega \ll k_bT$, Bose-Einstein statistics can be approximated using $\sim \frac{T}{\omega}$. Considering the factor of $\frac{1}{\omega}$ from Equation 3.15, this leads to the following approximation [127, 130].

$$I_{TDS}(q) \sim \frac{T}{\omega_{k,\nu}^2} \tag{3.17}$$

Fitting a force constant model to TDS data can be used to obtain the full phonon dispersion of a material [122, 123, 129]. However, this can become computationally demanding and challenging, especially with complex or disordered crystal structures. In proximity to the Γ point, the phonon dispersion becomes approximately linear, where the slope of this linear relationship is related to the speed of sound in that specific direction. This linear slope can be

approximated using the elastic constants of the material by equation 2.5. By comparing the TDS intensities along different crystallographic directions, the ratio between elastic constants can be obtained. These ratios can be transformed into absolute values by either rescaling to a bulk modulus or using a two-temperature method. If the temperature interval is chosen in a way that the thermal population varies significantly for different phonon branches at the Γ point, it also provides absolute values of the elastic constants. [120, 127, 128]

4 Experimental

4.1 Sample Preparation

Bulk sample synthesis was done using arc melting of high purity elements in protective Ar atmosphere. The purities of the used elements were ≥99.95 % for Ni, ≥99.9 % for Co, ≥99.9 % for Mn and ≥99.99 % for Ti. The Ar purity was ≥99.999 %. Additional cleaning steps were performed for Mn to reduce oxygen introduced into the melting chamber. This was achieved through induction melting in an alumina crucible followed by arc melting of pure Mn. Since Ti is an oxygen getter material, Ti oxide is hardly reduced during melting in an Ar atmosphere. Therefore, not only does the oxygen content of the atmosphere need to be reduced as much as possible, but also the oxide content of the pure elements.

Nevertheless, small inert Ti-O-N impurities cannot be completely avoided during the arc melting synthesis of Ni(Co)MnTi alloys. These impurities are shown in Figure 4.1 at both low and high magnifications. For the arc melting process, a Buehler MAM-1 arc furnace with a water-cooled copper crucible was utilized. The raw elements and cleaned manganese were introduced into the melting chamber and melted together at least five times. Ti getter was melted before the sample to reduce the oxygen content in the chamber. The melted button was flipped between each melting step to enhance homogeneity. Approximately 2-3 weight percent of Mn was added during the arc melting to compensate for Mn loss due to evaporation.

Heat treatment was carried out in sealed quartz ampules. The samples were wrapped in steel foil to minimize oxidation and prevent reactions with the quartz ampule. The samples were purged and flashed with Ar several times to minimize the presence of water and oxygen during the heat treatment. The final Ar pressure was 0.5 bar at room temperature. After the desired annealing time, the samples were quenched in water.

The annealing conditions of the samples varied between 1173 K and 1323 K and lasted from 4 to 10 days, depending on the intended purpose of the sample. Annealing at lower temperatures resulted in a grain size of around 100 μm, as shown in Figure 4.1 (a). In contrast, annealing at 1323 K led to abnormal grain growth, resulting in single grains several millimeters in size.

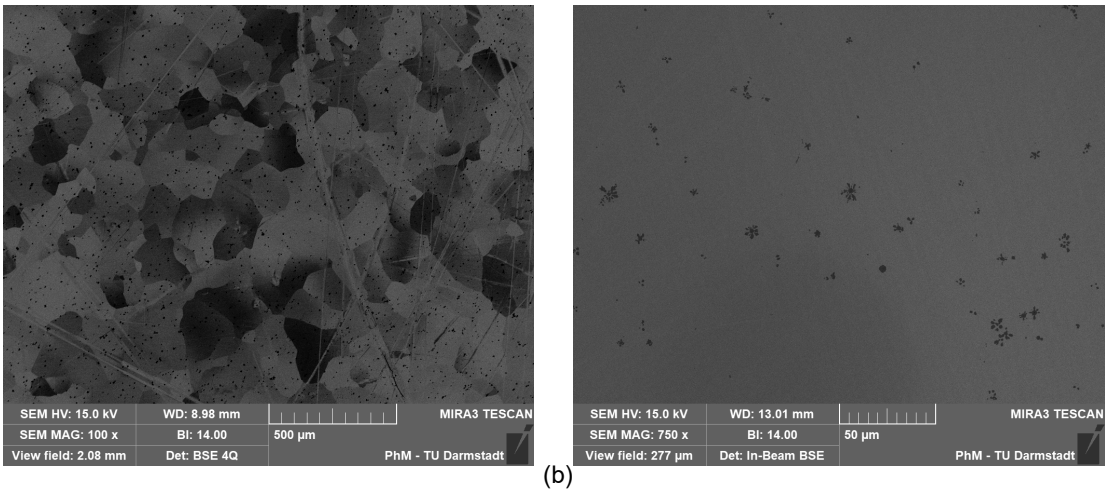

(a) (b)

Figure 4.1: BSE images of $Ni_{37}Co_{13}Mn_{33}Ti_{17}$ after annealing at 1173 K for 10 days with (a)100x and (b)750x magnification. Ti-O-N impurities are black spots due to their significantly lower density.

Polycrystalline powder samples

Powder samples were produced by annealing the bulk arc-melted sample at 1173 K for 6 days, followed by water quenching. This method is a well-established route for all-d-Heusler samples. [24] The relatively low annealing temperature was chosen to ensure that there is no Mn depletion at the sample edges, which is beneficial for achieving a chemically homogeneous powder. The influence of the annealing temperature on the microstructure can be neglected since the bulk sample will be powdered later. For powder production, the samples were cut and ball-milled using a Fritsch Pulverisette 0 with a steel mortar. The ground powder was sieved to <56 μm, packed into steel foil, and subjected to post-annealing in Ar-filled, sealed quartz ampules to achieve recrystallization of the powder. The ampule was flushed with Ar several times to reduce oxygen and water content as much as possible. The furnace was preheated to the desired temperature before inserting the sample to avoid decomposition at low temperatures. After the desired annealing time, the sample was water-quenched.

Long range order experiments

The bulk alloy was produced through arc melting, as described earlier. For the neutron diffraction experiment, the sample mass was approximately 15 g, while for other experiments, it was 5 g. To homogenize the samples, they were sealed in quartz ampules and annealed at 1173 K for 10 days and 6 days, respectively, followed by water quenching. Subsequently, the samples were cut and milled to a powder form. The powder was then annealed at specific temperatures

for one hour in sealed quartz ampules in an Ar atmosphere, followed by water quenching. In the case of samples annealed at 673 K and 573 K, they were annealed for 4 days to account for slower diffusion processes at low temperatures. As these temperatures were insufficient for recrystallization after milling, a pre-annealing step at 973 K was performed. All physical measurements were conducted on these powder samples to enable a direct comparison of the datasets.

Single crystalline samples

Single crystals were produced by taking advantage of the abnormal grain growth observed in the Co-containing samples at a temperature of 1323 K. The samples were annealed at 1323 K for 4 days, followed by water quenching. These single crystal samples were then cut into approximately 1mm thick plates. To prevent the samples from experiencing stress and deformation during the polishing process, Kulzer Technovit 5071 was used to embed the samples, and this embedding material can be dissolved in acetone. The samples were polished from both sides using SiC paper up to a grid size of 4000.

To make the grains visible for examination, the sample was etched with Kroll's etching solution for 5 minutes, which is commonly used for Ti alloys. This allowed the grains to become visible even without the use of optical microscopes. An example of this is shown in Figure 4.2 (a). The larger grains obtained can be directly used for laboratory single crystal diffraction in reflection mode, as discussed in section 5.4.1. For transmission single crystal diffraction, it is necessary to extract the corresponding grain. This is achieved by cutting the etched sample with a wire saw. Prior to cutting, visible large grains were inspected from both sides of the sample. From these large grains, cubes up to 1 mm in size are cut using a Well diamond wire saw. One crystal obtained in this manner is shown in Figure 4.2 (b). The resulting surfaces are polished from all sides, as described for the larger sample mentioned earlier. Subsequently, electrochemical etching is performed using a 30% H_3PO_4 electrolyte for 5 minutes at 7 V DC. The sample is contacted via a steel pin and a permanent magnet, with Cu used as the counter electrode. Electrochemical etching effectively removes any surface deformations still present after mechanical polishing. To ensure a single crystalline state, the single crystals are checked from all sides using Laue diffraction. A typical Laue diffraction pattern is shown in Figure 4.2, indicating that the orientation does not coincide with a specific direction due to the non-directional preparation method. A secondary heat treatment was introduced to achieve a specific degree of chemical order. For temperature-dependent studies, a temperature of 973 K was selected for 1 hour, resulting in the maximum degree of B2 order. Additional samples were annealed at 773 K for 1 hour to investigate SRO.

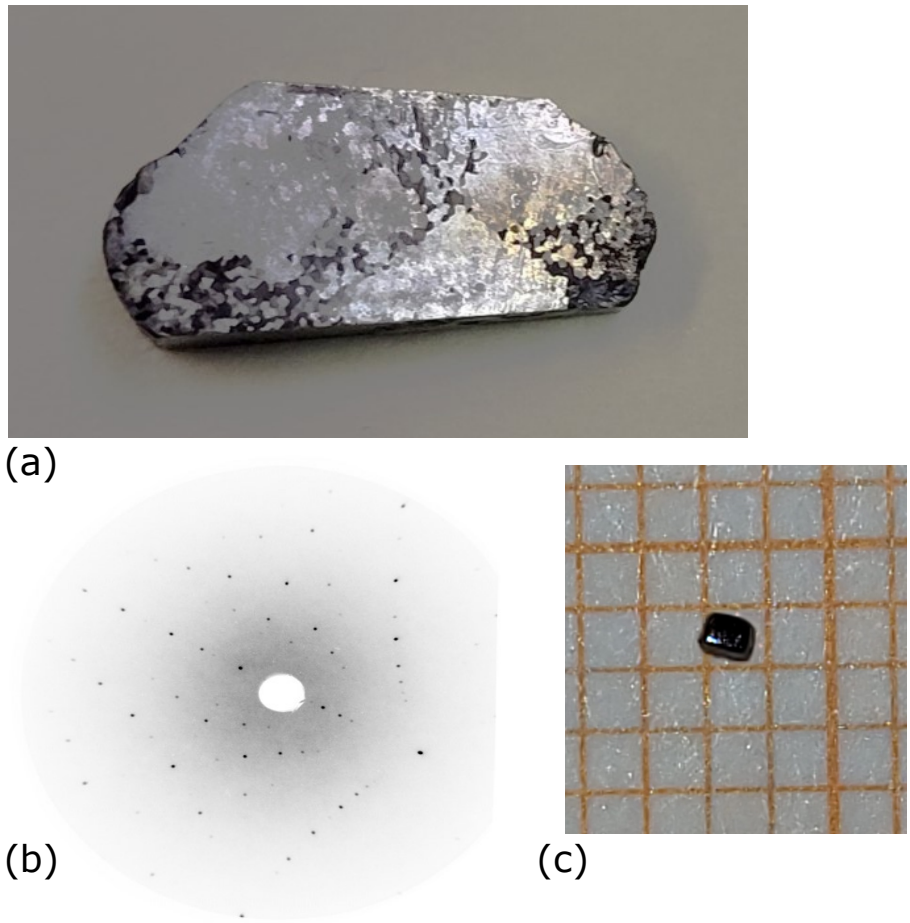

Figure 4.2: (a) Microstructure of a polycrystalline bulk sample after annealing for 4 days at 1323 K, polishing and etching with Krolls etchant for 5 minutes. Large grains can be used to cut out several single crystals (b) Size of a typical single crystal after cutting and before etching. (c) Typical Laue diffraction pattern of one site of the single crystal.

For experiments using x-ray tubes, the crystals are electrochemically etched for approximately 1 hour to reduce the crystal size to 100-200 μm without causing deformation. In the case of high-energy synchrotron diffraction, larger crystals can be utilized due to reduced sample absorption. Using larger samples provides advantages such as improved signal-to-background ratios and reduced diffuse scattering from the surface.

4.2 Diffraction

Neutron Diffraction

Many thanks to Dr. Narendirakumar Narayana and Dr. James Hester for obtaining the neutron diffraction data
Neutron powder diffraction experiments were conducted using the high-resolution diffractometer Echidna at ACNS with a wavelength of 2.43 Å [131]. The sample mass used for the measurement was approximately 2.5 g. In the neutron beam, there was a harmonic contamination of 0.3% of $\frac{\lambda}{2}$, which was corrected for during the data evaluation. Temperature control was achieved using a closed-cycle cryostat. The samples were heated above their Curie temperature, reaching up to 400 K, to enable the separation of nuclear and magnetic contributions.

4.2.1 Laboratory x-ray diffraction

Standard room temperature diffraction

Standard room temperature x-ray diffraction measurements were conducted in transmission mode using a Stoe Stadi P Diffractometer equipped with a position-sensitive detector, Ge(111) monochromator, and Mo $K_{\alpha 1}$ radiation. Powder samples smaller than 56 μm were affixed between Mylar foil using collodion. During the measurement, the samples were rotated to enhance statistics.

Temperature dependent x-ray diffraction

Temperature-dependent x-ray diffraction experiments were conducted in a transmission geometry using a custom-built setup. The setup included a Mo K_{α} radiation source, a He-closed cycle cold finger cryofurnace, and a Dectris Mythen 1K-R Detector. To correct for geometric errors, the powdered sample was mixed with NIST SRM 640d standard silicon powder. Detailed information about the setup can be found in Faske et al. [132].

The sample was affixed to a compressed graphite foil to maintain thermal contact with the cold finger. Various types of glue were employed depending on the temperature range. For temperatures below 440 K, standard cyanoacrylate glue (UHU) was used. For temperatures up to 550 K, Permabond 920 high-temperature cyanoacrylate glue was applied. For temperatures up to the maximum limit of the cryofurnace at 700 K, high-temperature varnish was used.

To convert the multi-channel analyzer data into 2θ values, raw detector frames were reconstructed using a custom Python script following the calibration procedure described by

Bergamashi et al. [133]. NIST SRM 660a LaB_6 powder served as a standard for the angular calibration.

Analysis of powder data

Rietveld analysis and the simulation of different order parameters were carried out using the FullProf software package [109]. The analysis of the martensite structure was conducted with JANA2006 [90]. For temperature-dependent data, the lattice parameter of the NIST 640d standard silicon powder was adjusted to account for the thermal expansion of silicon. Geometric errors, arising from slight sample displacements within the cryostat, were subsequently corrected with a sinusoidal shift.

Crystal structure images were generated using VESTA. [94]

Precession camera

The Buerger precession camera performs undistorted imaging of reciprocal space [134]. Precession camera images were captured using a Huber Buerger Precession camera 205 with $\lambda =$ Ag K_α radiation, a graphite monochromator, and a removable image plate as the detector on an etched $Ni_{37}Co_{13}Mn_{33}Ti_{17}$ single crystal, reduced to approximately 150 μm thickness. The sample thickness was selected to enable x-ray transmission. The crystal was affixed to a cactus needle and oriented with the precession camera due to the small crystal size that precluded Laue diffraction. A precession angle μ of 20° and a slit radius r_s of 20 mm were employed, with a camera magnification factor F of 100. The precession was conducted at a speed of 1 rotation per minute. Typical exposure times were approximately 15 minutes for sample adjustment and 1000 minutes for diffuse scattering measurements. The detector distance ($poss_I$) and the slit position s were calculated using the following equations, where p represents the lattice distance along the sample orientation, and n is the order of the layer. Using the lattice parameter of 5.915 Å, the slit distance and detector distance were calculated to achieve undistorted imaging of specific reciprocal space planes.

$$s = r_s \cdot cot(arccos(cos(\mu) - \frac{n\lambda}{p})) \tag{4.1}$$

$$poss_I = F \cdot \frac{n\lambda}{p} \tag{4.2}$$

For the 0th layer, this gives a slit distance of 55 mm and no change of the detector distance.

Laue diffraction

Laue diffraction in reflection geometry was employed for single crystal preparation and characterization. The measurements utilized a continuous x-ray spectrum from an Ag x-ray tube and a Huber 801 Laue camera equipped with an image plate detector and a 0.8 mm collimator. This setup allowed for the examination of large areas of single crystals obtained from the bulk sample. The sample was positioned at a distance of 32-40 mm from the image plate during the measurement, and a typical exposure time was approximately 10 minutes. It's worth noting that Laue diffraction only probes a few micrometers of the sample, making it crucial to ensure a deformation-free surface. Surface deformation resulting from cutting were carefully eliminated before conducting the measurements, either through grinding or etching.

Four circle diffractometer

Laboratory single crystal diffraction on bulk samples in reflection mode was carried out using a STOE four-circle diffractometer. The diffractometer utilized Cu-K_α radiation, a mirror monochromator, an energy-dispersive detector, and automated filters to control the incident intensity. The diffraction experiments were controlled using spec software. Following the determination of an orientation matrix, various analyzes, such as q-scans and reciprocal space maps, were conducted to investigate ordering and thermal diffuse scattering.

4.2.2 High Energy single crystal diffraction

High-energy single crystal x-ray diffraction (XRD) experiments were conducted at the P21.1 beamline of the Petra3 synchrotron facility at Deutsches Elektronen-Synchrotron (DESY). This beamline is specifically designed for utilizing high-energy x-rays in total scattering measurements on both single crystals and polycrystalline materials. Figure 4.3 provides an illustrative sketch of the beamline setup. The optical system of the beamline includes a single-bounce Laue monochromator, a harmonic rejection monochromator, and a second monochromator crystal, resulting in an energy resolution of $\frac{E}{\Delta E} = 10^{-3}$. To control the intensities of the direct beam, a filter box with 30 sheets of Tl foil, each 100 μm thick, was employed. The distance between the area detector and the sample could be adjusted within the range of 300 mm to 4000 mm. For detection, a Dectris Pilatus CdTe 2M detector was utilized, featuring a CdTe sensor material that ensures high quantum efficiencies for energies exceeding 30 keV. At the specific energy used in our experiment, the quantum efficiency was measured at 56%. During data collection, the crystal was rotated at a constant velocity of $1°/s$, with the detector readout occurring every 0.1 s.

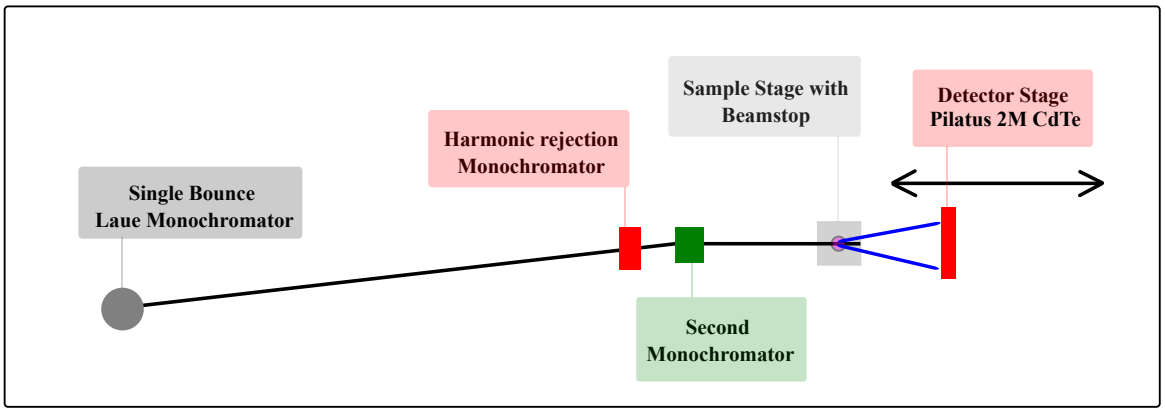

Figure 4.3: Sketch of the basic setup at the beamline P21.1 at the synchrotron Petra3 at DESY.

The P21.1 beamline was operated using the "ONLINE" software. The crystals were securely mounted on a cactus needle attached to a Huber 1001 goniometer head using epoxy glue. To maximize data quality, the measurements were conducted without the cactus needle and glue, given the large sample size. A beam size of 300 μm was employed, and the beamstop was positioned in close proximity to the sample to minimize air scattering. Precise temperature control was achieved through the use of a liquid nitrogen cryostreamer. This experimental setup is illustrated in detail in Figure 4.4 (a). For the analysis of thermal diffuse x-ray scattering, a working distance of 1000 mm was employed. To further extend the measurement time and photon flux while staying within detector limits for the study of short range order, a working distance of 2200 mm was utilized. In this case, fundamental Bragg reflections were obstructed by tungsten discs, and a step scan replaced the continuous scan method. The setup involving the blocked Bragg spots is illustrated in Figure 4.4 (b).

The raw detector frames were indexed using XDS [135], and subsequent data processing and analysis were performed using Python. The Meerkat software package facilitated the reconstruction of 3-dimensional arrays with reciprocal space coordinates.[136] Other Python packages, such as numpy, fabio, h5py, and scipy, were employed for tasks like masking, applying Laue symmetry, and conducting linescans.

Determination of elastic constants

Elastic constants are determined by fitting the thermal diffuse scattering (TDS) data around 190 fundamental Bragg reflections using the TDS2EL2 software package [127]. The elastic constants are fitted within a specified Region of interest (ROI) centered around the fundamental Bragg peaks. Frames containing Bragg peaks are excluded from the analysis due to potential artifacts. Within the software, the orientation matrix and geometrical parameters are determined. For

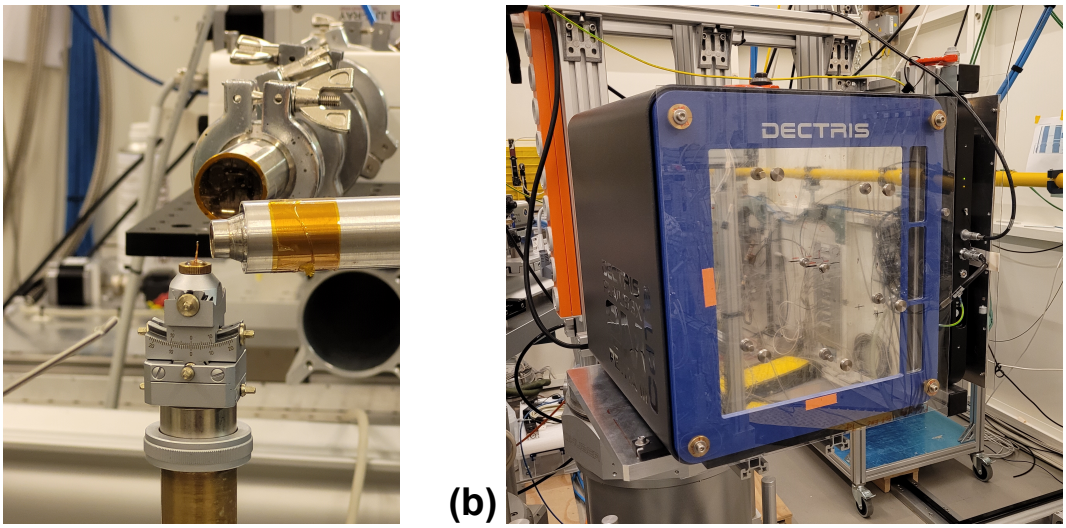

Figure 4.4: Setup of (a) cooler and beamstop (b) Dectris Pilatus CdTe 2M detector. Here shown are additional tungsten discs for blocking Bragg reflections are added to increase the possible counting time. These are removed for otherwise.

the fitting procedure, a B2 lattice model is employed instead of $L2_1$, and symmetry elements consistent with the m-3m Laue symmetry are applied. Selecting an appropriate ROI is critical, ensuring that the TDS is not influenced by scattering from the Bragg reflection at the lower boundary of the ROI while maintaining the validity of the elastic approximation at the upper boundary. This means that any possible TA_2 phonon anomaly must be excluded. Given the intrinsic structural instability, the exact position of the upper boundary cannot be confirmed through first-principle calculations but is determined based on a literature comparison with phonon dispersions of Ni-Mn-Z Heusler alloys and the approximation for low-energy phonons as described in equation 3.17. The final ROI is from 0.05 to 0.1 reciprocal lattice units in the B2 lattice. The elastic constants at 270 K are determined using a two-temperature fit of the data recorded at 290 K and 250 K. This fitting procedure effectively subtracts all features unrelated to TDS. This approach relies on the assumption that the elastic constants remain constant within this temperature range, providing relative elastic constants. In cases where the temperature interval allows for linearity, absolute elastic constants can be determined. However, at relatively high temperatures, the elastic constants are re-scaled using the measured indentation modulus.

The indentation modulus was measured on a polycrystalline sample with the same composition and different grain orientations, as described in section 4.3.2. The indentation modulus represents the average elastic modulus within the probed volume and is equivalent to the Young's modulus for an isotropic material. Changes in the elastic constants are then determined by single-temperature fits that are adjusted based on this value.

To facilitate re-scaling, established relationships between elastic constants and the elastic moduli of cubic materials are applied [137].

$$C_{11} + 2C_{12} = 3B_0 \tag{4.3}$$

$$G_v = \frac{1}{5}(3C_{44} + C_{11} - C_{12}) \tag{4.4}$$

$$Y = \frac{9B_0G_v}{3B_0 + G_v} \tag{4.5}$$

C_{11}, C_{12}, and C_{44} represent the elastic constants of the cubic solid. Additionally, B_0 stands for the bulk modulus, G_v denotes the isotropic Voigt's shear modulus, and Y corresponds to the isotropic Young's modulus. The latter, Young's modulus, is determined experimentally using the indentation modulus.

4.3 Other

4.3.1 Magnetometry

Many thanks to Benedikt Beckmann for performing the magnetization measurements.
Isofield magnetization measurements were performed on a Quantum Design Physical Properties Measurement System (PPMS-14 T). A cooling and heating rate of 2 $Kmin^{-1}$ was used. A field of 50 mT was used to determine Curie temperatures and a field of 1 T to analyze the phase transition temperatures and hysteresis. The hysteresis was determined at the inflection points of the temperature dependent magnetization.

4.3.2 Nanoindentation

Many thanks to Franziska Staab for performing the Nanoindentation analysis.
The indentation modulus of a bulk sample was determined using a G200 nanoindentation system (KLA) equipped with a diamond Berkovich tip. A continuous stiffness measurement was used at an input strain rate of 0.05 s-1 and the maximum indentation depth was set to 2000 nm. The indentation modulus was averaged over an indentation depth range of 800-2000 nm of in total 25 indents located in different oriented grains. To determine the crystal orientations of the grains which were tested by indentations, electron backscatter diffraction (EBSD) was used in a scanning electron microscope (TESCAN Mira 3). The step size during the analysis was set to 5 μm.

4.3.3 Magnetic Interaction calculations

Many thanks to Dr. Olga N. Miroshkina for performing the calculations on magnetic interactions. To investigate the effects of disorder on T_c and the martensitic phase transition, calculations on the Curie temperature and the Bain path were performed for different degrees of order. Chemical Disorder was modeled analytically within the Coherent Potential Approximation (CPA). [138, 139] For the Curie temperature, the electronic structure and magnetic properties were modelled with the help of a KorringaKohnRostoker (KKR) approach as implemented in the Munich SPR-KKR code [140, 141] in full-potential mode together with scalar relativistic corrections. The exchange-correlation functional was treated within the generalized gradient approximation (GGA) following the PBE scheme [142]. The angular momentum expansion was carried out up to $l_{max} = 3$ (f-states). Electronic self-consistency was assumed to be reached when the error in the potential functions dropped below 10^{-6}. Brillouin zone integration was carried out using the special point method with a regular k-point grid of 1250 points, which corresponds to a $39 \times 39 \times 39$ mesh in the full Brillouin zone. The Heisenberg model exchange parameters J_{ij} between pairs of atoms i and j of all different chemical types and positions within a cluster radius of four lattice constants were calculated following Liechtenstein's approach [143]. From a given set of J_{ij}, the Curie temperatures were determined within the mean field approximation.

4.3.4 Bain path calculations

Many thanks to Nuno M. Fortunato for performing Bain path calculations.
The Bain path was calculated using the exact-muffin-tin orbitals EMTO method. [144–146] For the total energy calculations the full charge density technique [147] was adopted, with the PBE functional [142] and a 13x13x13 K-mesh. The size of the potential spheres of the Ni site were chosen to be 0.95 of the ASA sphere radius and the Mn and Ti sites were set to 1.00. At each c/a point the energy minima of the energy-volume curve fit and the disordered local moment approach [148] for the magnetic ordering were used.

5 Results and Discussion

The results section of this thesis is divided into two main parts. The first part focuses on long range atomic structures, encompassing topics such as chemical long range ordering, martensite structures, and the influence of these long range structural properties on the martensitic phase transition. Some of the findings in this part have already been published.[149] Additionally, the influence of composition on the phase transition and the crystallographic compatibility between austenite and martensite will be discussed. The second part is focused on the analysis diffuse x-ray scattering in single crystals with a focus on thermal diffuse scattering and short range order diffuse scattering. For that, the very first single crystals reported so far have been grown. The analysis of the thermal diffuse scattering provides valuable insights into the elastic and vibrational properties of the instability of the cubic austenite structure, while the investigation of short range order deepens the physical understanding of the material system and influences the phase transition as well.

5.1 Chemical Long Range Order

Understanding chemical ordering in all-d-Heusler alloys remains challenging, as discussed in section 2.2.5. With over 10 at.% Co in these alloys, the presence of a fourth element adds complexity to potential ordering schemes. Additionally, Co's low concentration, often assumed to occupy the Ni site, makes its ordering effects uncertain. As a result, the specific experimental ordering patterns and their influence on electronic structure and martensitic transitions remain unclear.

Determination of chemical order

The determination of order in this system is challenging. The very similar atomic scattering factors of the 3d transition metal elements leads to a small contrast in x-ray experiments and therefore to low scattering intensities of the corresponding superstructure reflections. Often, neutron powder diffraction (NPD) can be used to resolve this dilemma, but in the special case of

Ni(Co)MnTi, Ti and Mn also possess a very similar (negative) scattering length.[149] A number of theoretical works studied the chemical ordering phenomena from the first principles: Yan et al. [31] found that $L2_1$ structure is lower in energy than the B2 configuration. However, the energy difference between these two structures is rather small and comparable to that of thermal fluctuation at room temperature. Guang et al. [34] investigated the possible partial disorder configurations in the B2 structure realized by atomic exchange on the basis of $L2_1$ and found that the most favorable ordering results when Ti atoms are exchanged with the nearest neighboring Mn atoms. As for the Co positions, it was shown by Wei et al. [25] that Co replaces Ni at a specific site which leads to an ordering between Ni and Co. [149]

Since the important properties of the all-d-Heusler alloys are connected to the martensitic phase transition, the composition and the heat treatment of the powder is optimized for best elemental contrasts while still maintaining a martensitic phase transition. It is expected that a possible ordering temperature would be at its maximum at the equiatomic ratio. [5] The optimal elemental contrast regarding a $L2_1$ order would be achieved for equal Mn and Ti content, but the stoichiometric $Ni_{50}Mn_{25}Ti_{25}$ alloy does not exhibit a martensitic phase transition. Therefore, the off-stoichiometric $Ni_{50}Mn_{27}Ti_{23}$ concentration is investigated. This alloy shows a martensitic phase transition at around 70 K, confirmed by temperature dependent XRD. The powder was heat treated at various temperatures(1173 K-573 K) and it was found that the annealing temperature has a negligible influence on the phase transition. Therefore, one would expect to obtain the maximum degree of order with the lowest annealing temperature that still provides enough thermal energy to enable the diffusion processes. Therefore, annealing temperatures from 1173 K down to 573 K are chosen. At 573 K it is expected that the thermal energy would be too low to enable diffusion in a reasonable time scale. In order to investigate possible chemical ordering, Mo K_α radiation is used; Cu radiation would lead to high fluorescence background and a weaker contrast between the corresponding elements, Co radiation would not permit transmission experiments and lead to a smaller scattering contrast. The measurement of the sample annealed at 673 K are displayed in Figure 5.1, together with the corresponding positions of the expected reflections. In general, the (111) reflection is connected to the $L2_1$ order and the (200) reflection to the B2 order. The presence of B2 order is well established in these systems, since the intensity of the corresponding superstructure reflection (200) is much higher than for the (111) reflection of the $L2_1$ order. [24] (111) texture effects can be avoided due to a powdered and continuously rotated sample; this was verified by using the intensity of the (222) reflection. The degree of $L2_1$ order in terms of the Bragg Williams order parameter is calculated, shown in equation (5.1). [110] The Structures for L=1 and L=0 are shown in Figure 5.2.

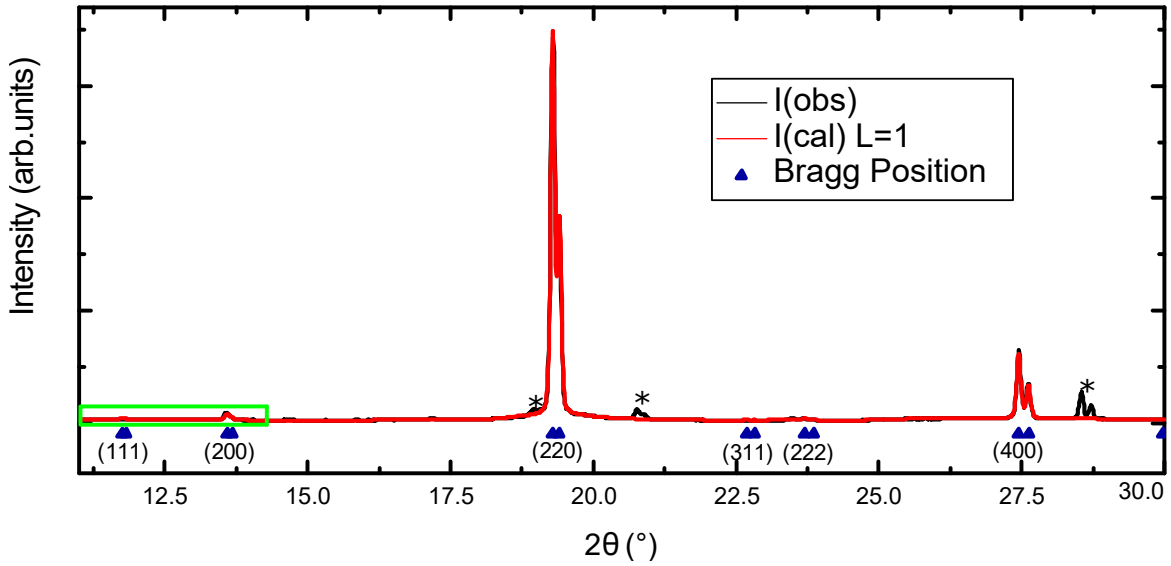

Figure 5.1: Diffraction pattern of $Ni_{50}Mn_{27}Ti_{23}$, heat treated at 673 K, together with the simulation for an $L2_1$ order parameter of L=1. The area of interest for ordering reflections is marked in green. The reflections marked with an asterisk are originating from the aluminum foil sample support and a minor (Ni,Mn)Ti_3 $P6_3/mmc$ side phase.

$$L = \frac{Ti_{Ti} - Ti_{Mn}}{N/2} \tag{5.1}$$

Since the concentration of Ti and Mn is not the same, the order parameter is calculated with respect to the lower concentration element Ti. In Kröger-Vink notation, Ti_{Ti} is a Ti atom on the ordered Ti-site and Ti_{Mn} a Ti-atom on the ordered Mn-site. N is the number of corresponding lattice sites. The diffraction pattern for each order parameter is simulated using the FullProf software package.[109]

From Figure 5.3 it can be inferred that the sample does not show any long range order larger than L=0.2, where the lower limit of the determination is set by the background level. Most likely, no $L2_1$ order is present at all. Annealing at higher temperature, which enables more diffusion, or for longer time at lower thermal energies, which is closer to the ground state, leads to the same result, which is shown in Figure 5.4.

The missing $L2_1$ order at all annealing treatments confirms theoretical investigations done so far on this system.[27, 31, 34] In order to induce a magneto-structural phase transition in the Ni-Mn-Ti alloy, Co is added for its ferromagnetic activation effect. The same kind of analysis as for $Ni_{50}Mn_{27}Ti_{23}$ in Figure 5.3 is performed; from these ordering between Mn and Ti can be excluded on the basis of the scattering data. Ordering is also less likely for lower concentrations

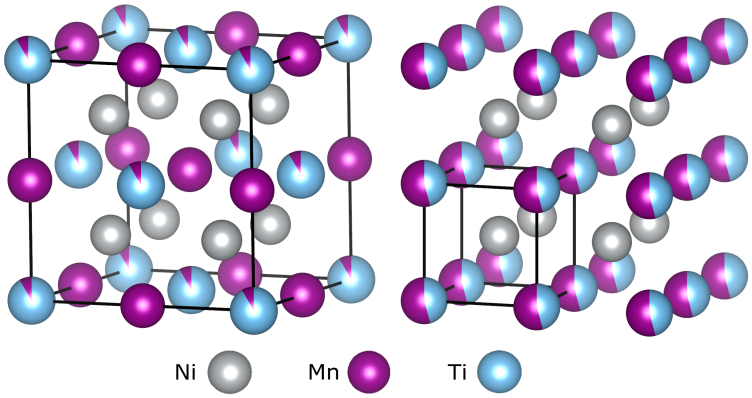

Figure 5.2: Crystal structures for an order parameter of L=1 and L=0 with the corresponding change in unit cell size.

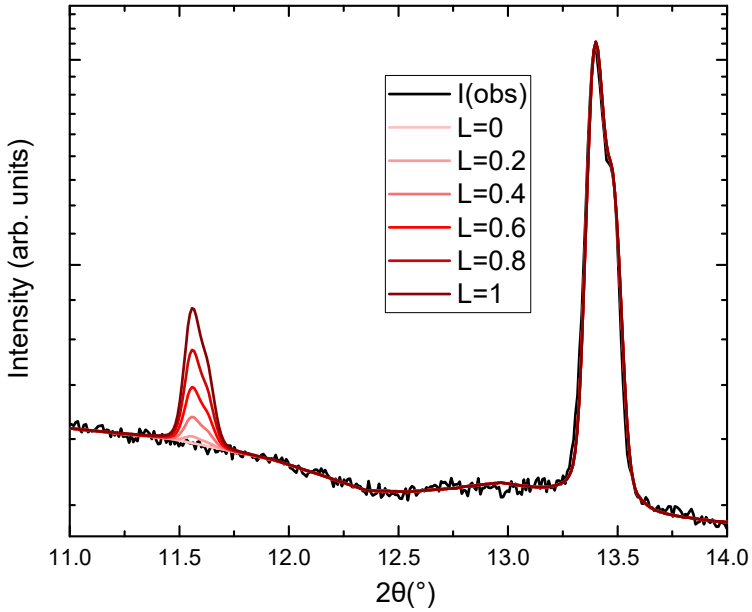

Figure 5.3: The area marked in red in Figure 5.1 with different simulated order parameters for $Ni_{50}Mn_{27}Ti_{23}$. Intensity is given in a log scale in order to pronounce the effect of small order parameters.

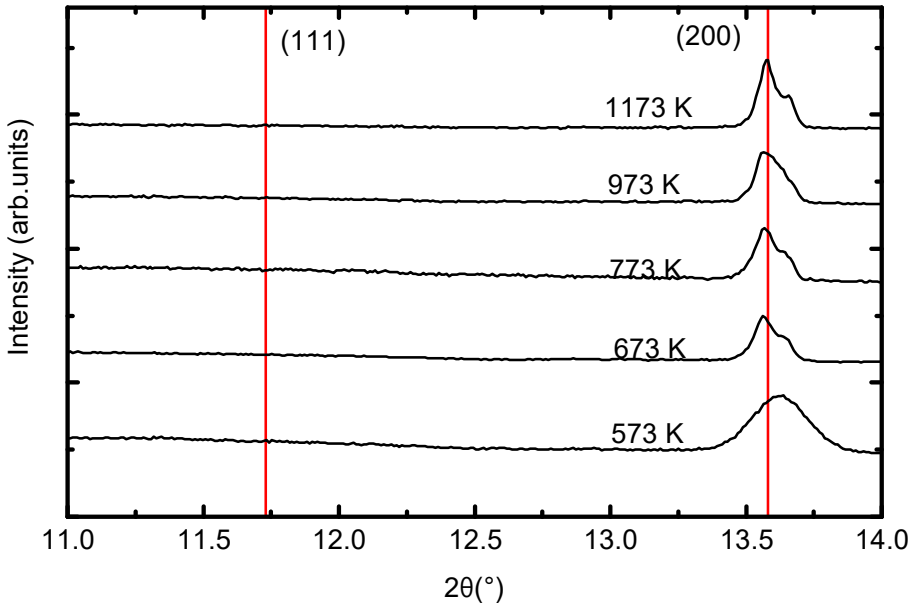

Figure 5.4: Area of the ordering reflections as in Figure 5.3 for $Ni_{50}Mn_{27}Ti_{23}$ for annealing temperatures between 573 K and 1173 K. the position of potential (111) and (200) reflections is marked.

of one element, since a hypothetical ordering temperature would decrease further within a mean field model for atomic ordering.[110] Compared to Ni-Mn-Z Heusler alloys, the amount of Co that is needed to induce a magneto-structural phase transition is quite large (12-17 at.% [24, 27]), which in turn makes it easier to investigate its position in the alloy. Wei et al. predicted that Co replaces Ni on a specific site, which would assume an ordering between Ni and Co. [25] For Co, the neutron scattering contrast in relation to all other elements is very pronounced. Therefore, NPD experiments can give some valuable insights into the position of the Co atom. Since Mn and Ti have a negative scattering length, the intensity of the superstructure reflections are even higher than the intensity of the fundamental reflections. To investigate this atomic ordering and the influence of the annealing protocol, NPD on two samples held at 400 K, which were annealed at 1173 K and 973 K, but were made from of the same powder with the composition $Ni_{37}Co_{13}Mn_{33}Ti_{17}$ is performed. The low temperature structure of this composition can be described as a 6M(IC) monoclinic structure. This is elaborated in more detail in section 5.3. A temperature of 400 K for NPD is chosen to exclude magnetic scattering, since it lies above the Curie temperature of $\approx 350\ K$. The x-ray and neutron diffraction data for both samples are displayed in Figure 5.5. These two samples are in the focus, since it is known from magnetization data, shown in Figure 5.6, that the phase transition is largely influenced by annealing in the above mentioned temperature range. The measurements clearly exclude chemical ordering between Ni and Co, since the (111) reflection is completely absent after subtraction of a 0.3 % $\frac{\lambda}{2}$

Table 5.1: Normalized intensities of all reflections at 400 K for $Ni_{37}Co_{13}Mn_{33}Ti_{17}$ after annealing at temperatures of 1173 K and 973 K followed by water quenching. The fundamental reflection (220) is set to 1. (s) indicates a B2 superstructure reflection and (f) a fundamental reflection. For better consistency, the Miller indices are used according to the $L2_1$ structure. In the present B2 structure the indices would be halved.

Reflection	I(1173 K)	I(973 K)	I(973 K)/I(1173 K)
(200) (s)	5.15714	6.3358	1.22855
(220) (f)	1	1	1
(222) (s)	3.01989	3.56145	1.17933
(400) (f)	0.36356	0.32416	0.89161
(420) (s)	10.382	11.78465	1.1351

contamination, which is present in the neutron beam. Instead, the intensities of superstructure reflections and fundamental reflections, shown in table 5.1, reveal that there must be a change in the degree of B2 order, since all superstructure reflections are more pronounced for the sample annealed at 973 K than for 1173 K.

From the x-ray measurements it is known that Ti and Mn are not ordered, so only a B2 order is present with Mn/Ti at one site and Ni/Co at the other. In order to determine the B2 order parameter from the NPD data, an artificial Mn/Ti atom is introduced. Its scattering length is -3.631 fm, which is the concentration weighted average of the Mn and Ti scattering lengths. This procedure takes into account the prior knowledge from the x-ray measurements, but at the same time concedes that the two elements could not be distinguished by NPD. The refinements yield a perfectly ordered B2 structure for the sample annealed at 973 K, but some disorder for annealing at 1173 K. The exact amount of disorder depends on the elements involved. Since ordering can be estimated from electronegativity arguments [150], it is unlikely that Ni changes its position and for Mn and Ti it would not lead to a large difference due to quite similar scattering length. Since the electronegativity of Co is closer to Mn than to Ti it is expected that the disorder arises from an exchange of Co and Mn Atoms. Another hint at the role of a Co/Mn atom exchange is the fact that in samples without Co, the shift of the phase transition does not appear. If vacancies would be assumed to be the culprit of the disorder, a reasonable vacancy concentration would not lead to such a large difference in intensity. Therefore, it is assumed that the origin of disorder lies between Co and the averaged Mn/Ti atom; The calculation shows, that 2.5 at.% of Co on the Mn/Ti site and 10.5 at.% at the Ni site would explain the superstructure NPD intensities.

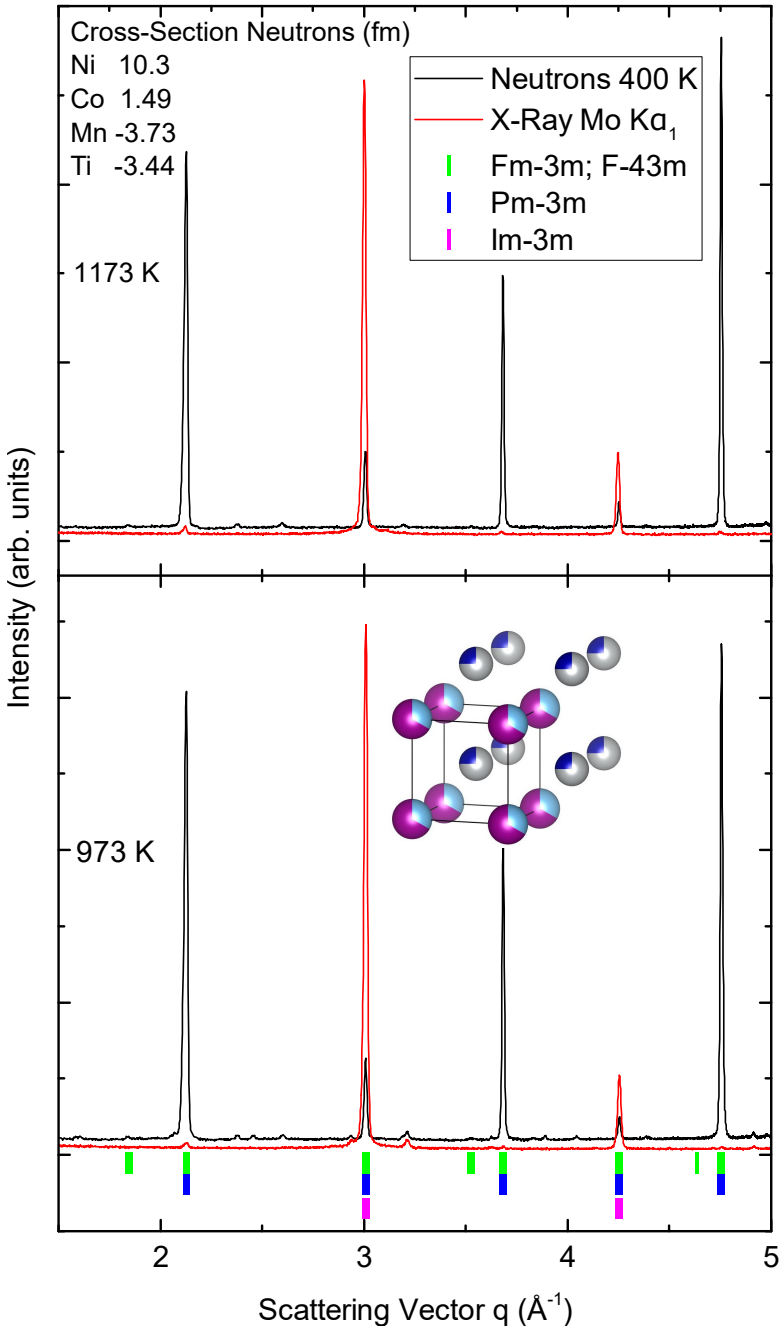

Figure 5.5: NPD and X-ray diffraction (XRD) data of $Ni_{37}Co_{13}Mn_{33}Ti_{17}$ for different annealing temperatures. The neutron scattering length for the corresponding elements is given, for x-rays it is proportional to the number of electrons. A (Ni,Mn)Ti_3 $P6_3/mmc$ side phase is present(1 %), which is common for these alloys. [31] $0,3\ \%\ \frac{\lambda}{2}$ is present in the neutron data which is corrected for in the data evaluation.

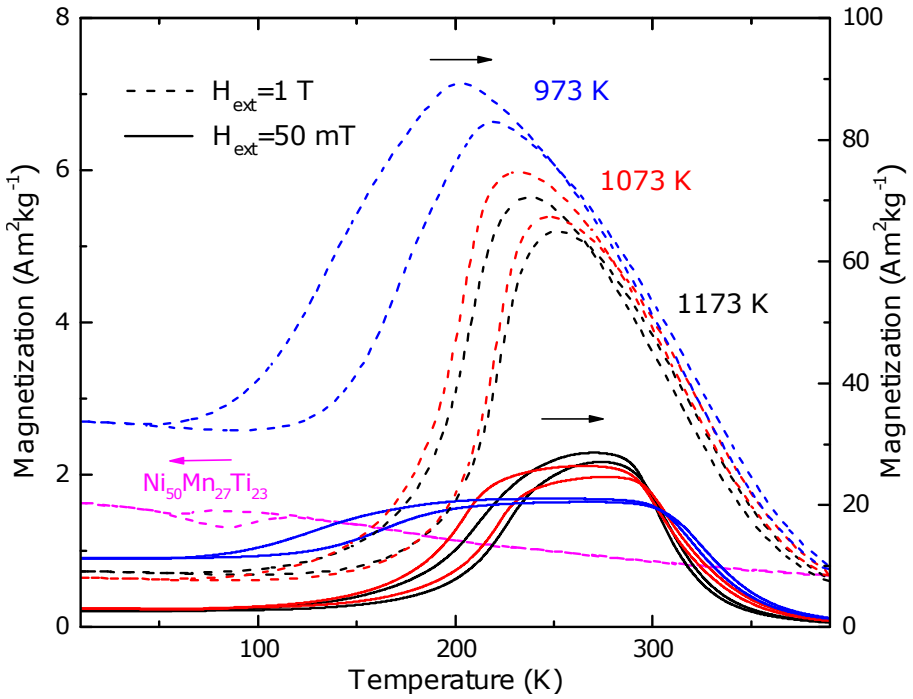

Figure 5.6: M-T curves of $Ni_{37}Co_{13}Mn_{33}Ti_{17}$ powder for different annealing temperatures at 1 T(dashed lines) and 50 mT(solid lines) and M-T curve of $Ni_{50}Mn_{27}Ti_{23}$ at 1 T.

Influence of Order on the phase transitions

This disorder seems to be quite small, but since Co is responsible for enhancing the magnetic coupling [24] and stabilization of the cubic structure in Heusler compounds [151], it can significantly influence the phase transition, which is shown in the magnetization in Figure 5.6 and in the diffraction in Figure 5.7. While increasing the annealing temperature from 973 K and 1073 K to 1173 K, the martensitic phase transition shifts to higher temperature and the Curie temperature T_c to lower temperatures. In the sample annealed at 973 K, kinetic arrest appears due to the low phase transition temperature, verified by temperature dependent x-ray diffraction.

In order to gain insight into the shift of T_c and the martensitic phase transition temperature and to verify our disorder model, calculated the phase stability and magnetic properties for different degrees of Co/Mn disorder, seen in Figure 5.8. The calculations show that T_c is sensitive to chemical disorder: mirroring our experimental work, T_c decreases with disorder, mainly due to the increasing competition between ferromagnetic Mn-(Ni,Co) interactions and antiferromagnetic Mn-Mn interactions arising from the redistribution of the elements between the sites (see supplementary). The latter is also responsible for the concomitant decrease

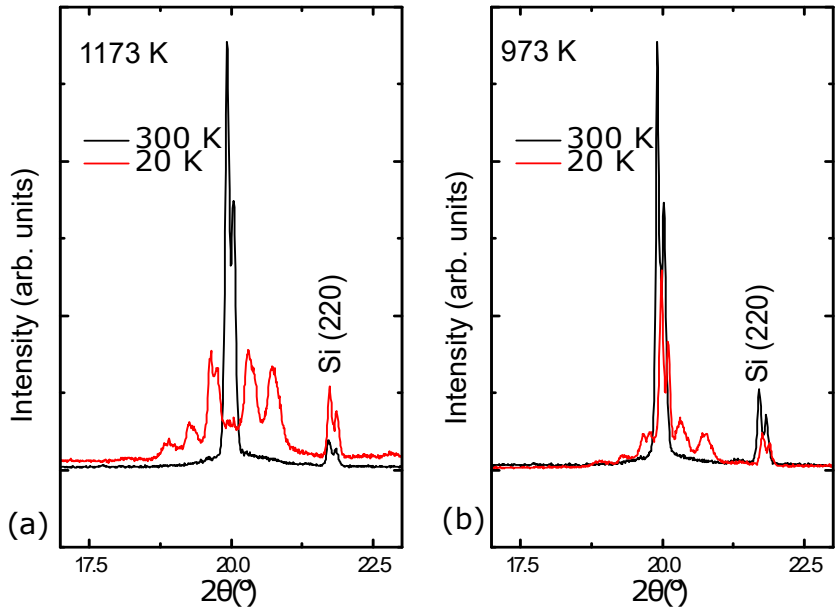

Figure 5.7: (a),(b) Temperature dependent x-ray diffraction data for $Ni_{37}Co_{13}Mn_{33}Ti_{17}$ annealed at 1173 K and 973 K at 300 K (black) and 20 K (red). The martensite crystal structure can be indexed as an 6M(IC) monoclinic crystal structure(see Figure 5.10).

in the total magnetization. Furthermore, the energy surface as a function of tetragonality along the Bain path changes: the calculated energy difference (ΔE) between the austenite ($\frac{c}{a} = 1$) and martensite ($\frac{c}{a} \neq 1$) leads to an expected shift of the martensitic phase transition temperature.[152] Disorder destabilizes the cubic structure and therefore may increases the phase transition temperature. Furthermore, the energy difference between the B2 ordered structure and those with Co-Mn disorder increases with the amount of disorder as shown in Figure 5.9. The energy difference between the fully ordered B2 structures and the calculated disorder is rather small (24 meV/atom), which shows that such a disorder can easily be thermally induced. Our calculations verify the trend seen experimentally and it can infer that chemical disorder with respect to the position of the Co atoms can be used to tune both the magnetism and the structure of the alloy system Ni(Co)MnTi. This widens the possibilities for alloy design beyond the conventional discussion based on the ratio $\frac{e}{a}$.

If these results should be transferred to bulk materials or melt spun ribbons, the different cooling behavior has to be taken into consideration, which is in general different from that of the powders investigated here. Since ordering kinetics tend to be very fast in this temperature range, not only the annealing temperature but also the cooling rate becomes crucial. [22] For melt spun ribbons, a large shift of the phase transition with annealing temperature is recognized by two groups and Liu et al. also suggests that this effect could be attributed to ordering. [153,

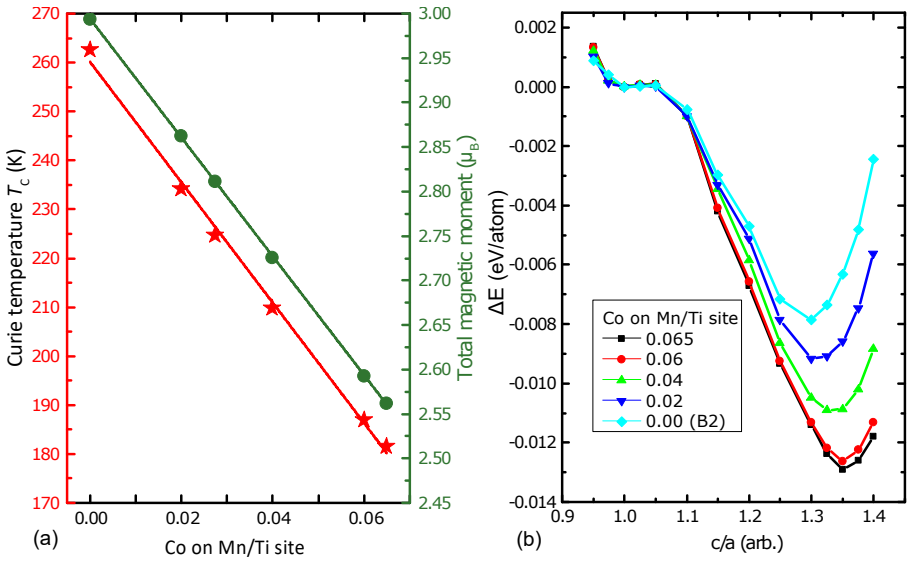

Figure 5.8: (a)Calculated Curie Temperature T_c and total magnetization for $Ni_{37}Co_{13}Mn_{33}Ti_{17}$ for different amounts of Co on Mn/Ti site. (b) Bain path for $Ni_{37}Co_{13}Mn_{33}Ti_{17}$ for different amounts of Co on Mn/Ti site. The total number of atoms is set to 1.

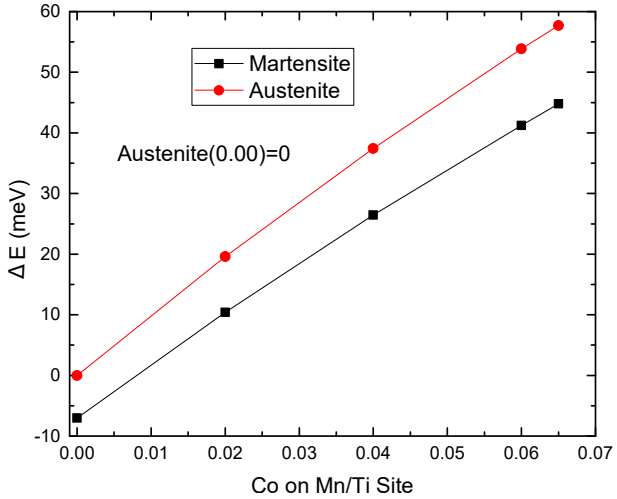

Figure 5.9: Energy difference per atom between austenite and tetragonal distorted martensite of $Ni_{37}Co_{13}Mn_{33}Ti_{17}$ for different amounts of Co on Mn/Ti site. The perfectly B2 ordered austenite is set to 0.

154] Their suggestion can be verified within the experimental results presented in here.

5.2 Martensite Structure

The structure of the martensite phase in Ni-Mn-Z Heusler alloys can adopt either a tetragonal $L1_0$ structure or a modulated martensite structure, which may exhibit tetragonal, orthorhombic, or monoclinic symmetry. The specific structure depends on various factors, including phase transition temperatures, composition, and the choice of the Z-element. Higher transition temperatures typically favor the formation of the tetragonal $L1_0$ structure, while lower transition temperatures lead to the appearance of modulated phases. Additionally, intermartensitic phase transitions can contribute to the formation of the $L1_0$ structure. [16, 155]

In the transition temperature range investigated within this work, a modulated martensite structure is formed. These martensite structures in Ni(Co)MnTi-based all-d-Heusler alloys can be effectively described using the superspace approach introduced in Section 2.2.3. As an example, this is shown for the sample $Ni_{37}Co_{13}Mn_{33}Ti_{17}$ in Figure 5.10, which is analyzed in terms of LRO in the section before. The Rietveld refinement was carried out using JANA2006.[90] The super space group used is $I2/m(\alpha 0\gamma)00$, which is consistent with the main group element Heusler alloys.[91, 92] Atomic positions and occupancies, as presented in Table 5.3, are oriented based on the long range B2 ordering observed in the austenite phase. It's worth noting that LRO can be more accurately determined in the austenite state and remains unchanged during the phase transition due to its diffusionless nature. The lattice parameters are summarized in Table 5.2. To describe the modulation, a periodic displacement along the c-axis of the average unit cell is employed, represented as a series of sinusoidal waves as shown in Equation 5.2. In the case of this sample, two sinusoidal waves were used, with their amplitudes detailed in Table 5.4.

Table 5.2: Lattice parameters of $Ni_{37}Co_{13}Mn_{33}Ti_{17}$ at 20 K. Since the structure is monoclinic, only the angle $\beta \neq 90°$ is given. q_{mod} is the modulation wavevector.

Temperature	a	b	c	β	q_{mod}
20 K	4.332(6) Å	5.487(9) Å	4.248(8) Å	92.574(4) °	$0.381c^*$

Table 5.3: Atomic positions of the average martensite unit cell.

Atom	x	y	z
Ni/Co	0.5	0.25	0
Mn/Ti	0	0.5	0
Mn/Ti	0	0	0

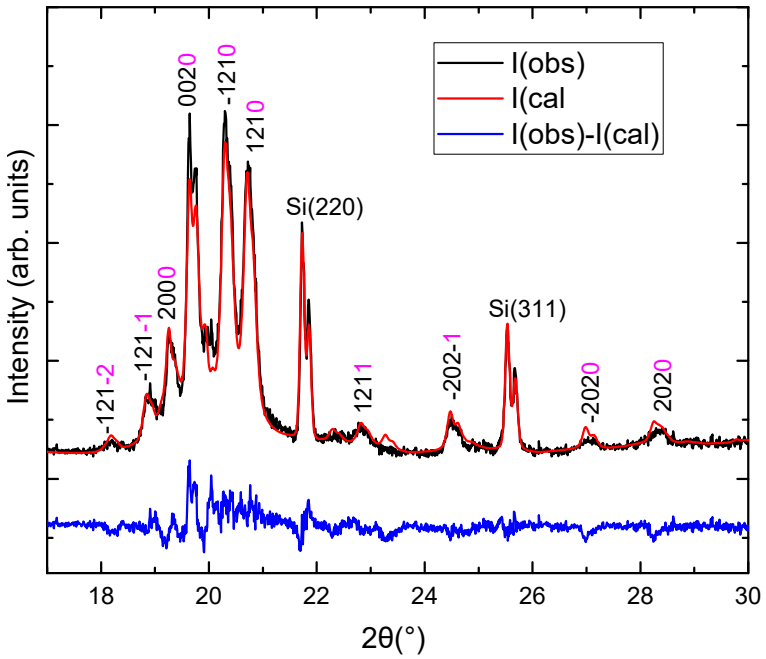

Figure 5.10: Fit of martensite for $Ni_{37}Co_{13}Mn_{33}Ti_{17}$ heat treated at 1173 K, at 20 K. The modulation index of the reflection is written in purple.

$$u = \sum_{n=1}^{2} A_i^n sin(2\pi n q_{mod}) \tag{5.2}$$

Table 5.4: Modulation parameters for $Ni_{37}Co_{13}Mn_{33}Ti_{17}$ at 20 K.

	x	y	z
A1	0.098903 Å	0 Å	-0.000541 Å
A2	0.04536 Å	0 Å	-0.005685 Å

5.3 Composition dependencies in $Ni_{50-x}Co_xMn_{33}Ti_{17}$

The impact of compositional changes on the magnetic properties and martensitic phase transition temperature in all-d-Heusler alloys has been extensively studied in the literature.[24, 27] However, investigations into changes in the crystalline lattice of both the high-temperature austenite and low-temperature martensite phases are still lacking. While alterations in composition can result in different ordering temperatures, the high-temperature phase remains cubic but may exhibit volume variations. In contrast, the low-temperature martensite can undergo changes in symmetry. Existing literature indicates that the precise relationship between these two structures can significantly impact their compatibility, which, in turn, influences hysteresis behavior.[23, 69, 95, 96, 98]

Hence, the structures of a series of samples with the composition $Ni_{50-x}Co_xMn_{33}Ti_{17}$ were investigated through temperature-dependent x-ray diffraction on powder samples. These powders were post-annealed at 1023 K to facilitate recrystallization. It's important to note that a significant sensitivity of the phase transition temperature to the specific annealing temperature, as discussed in Section 5.1, is only observed for Co content of $\geq$12 at.%. While the austenite phase undergoes a reduction in the lattice parameter with increasing Co content, following Vegard's law [156], the changes in the martensite structure are more complex. Figure 5.11 displays x-ray diffraction data at 20 K for three different Co contents. One prominent change is the splitting of the (121) reflection into two distinct reflections, (-121) and (121), which indicates a transition from quasi-orthorhombic to monoclinic crystal structure. Since the exact peak shape strongly correlates with monoclinic angles for angles close to 90°, which is anisotropic, it is challenging to definitively classify x=0 as monoclinic or orthorhombic. For consistency, all martensite data is refined using a monoclinic unit cell.

Fitting the data, as described earlier, quantifies this transition from a quasi-orthorhombic 4O(IC) structure to a monoclinic 6M(IC) structure. As the monoclinic angle β increases continuously, there is a corresponding continuous shift in the modulation wavevector q_{mod}. This observation highlights two important points. Firstly, it emphasizes the strong incommensurate character of the martensite structure, necessitating the use of superspace crystallography for its analysis since the wavevector shifts gradually rather than step-wise, as needed for commensurate structures. Secondly, because the modulation of the martensite can be linked to phonon softening and Fermi surface nesting in the austenite phase[7, 10, 157], it underscores the significant influence of Co on the vibrational properties of the alloy, which stabilizes ferromagnetism and the cubic high-temperature structure[24, 149].

For investigating the effect of this change in the martensite crystal structure on the phase transition, crystallographic calculations are performed to determine the transformation stretch

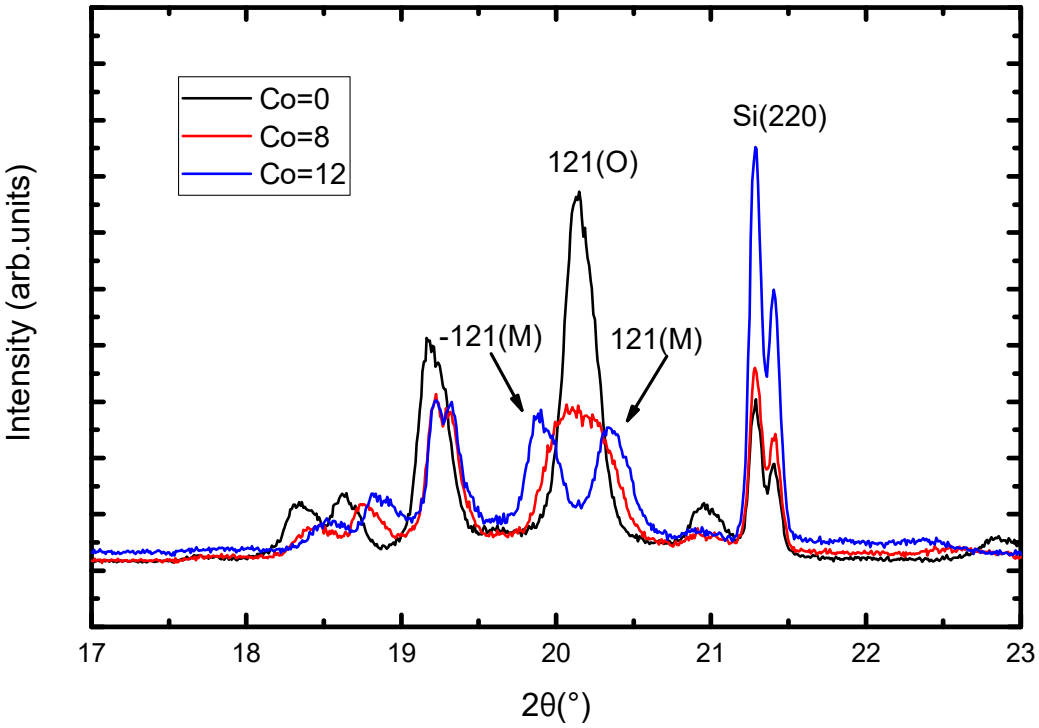

Figure 5.11: X-ray diffraction data at 20 K for the alloys $Ni_{50-x}Co_xMn_{33}Ti_{17}$. Standard NIST SRM640d silicon powder((220) reflection visible) is added for correcting geometrical errors.(O) is indicating an orthorhombic symmetry while (M) denotes a monoclinic symmetry.

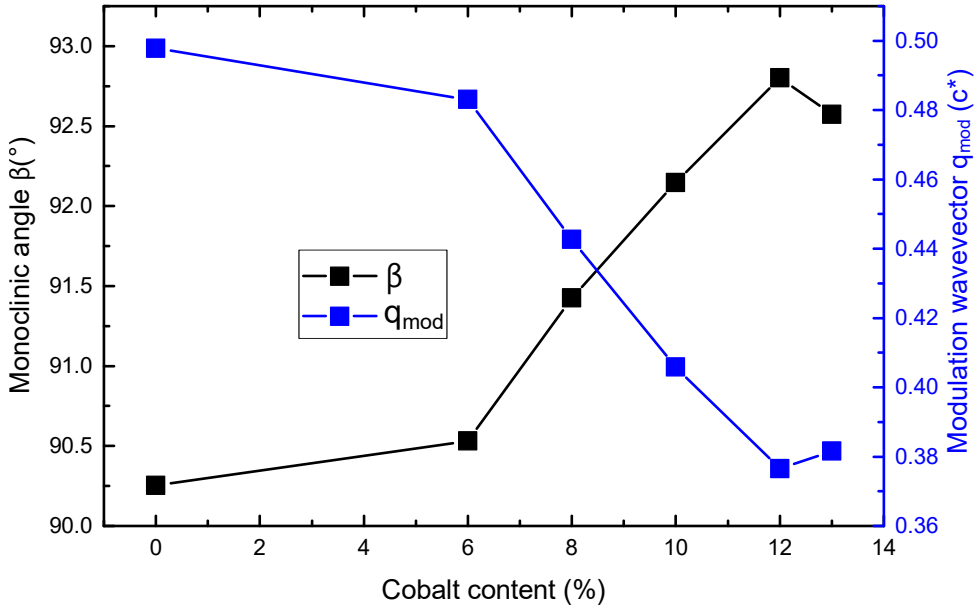

Figure 5.12: Monoclinic angle and modulation wavevector q_{mod}(0,0,c*) for the alloys $Ni_{50-x}Co_xMn_{33}Ti_{17}$ at 20 K.

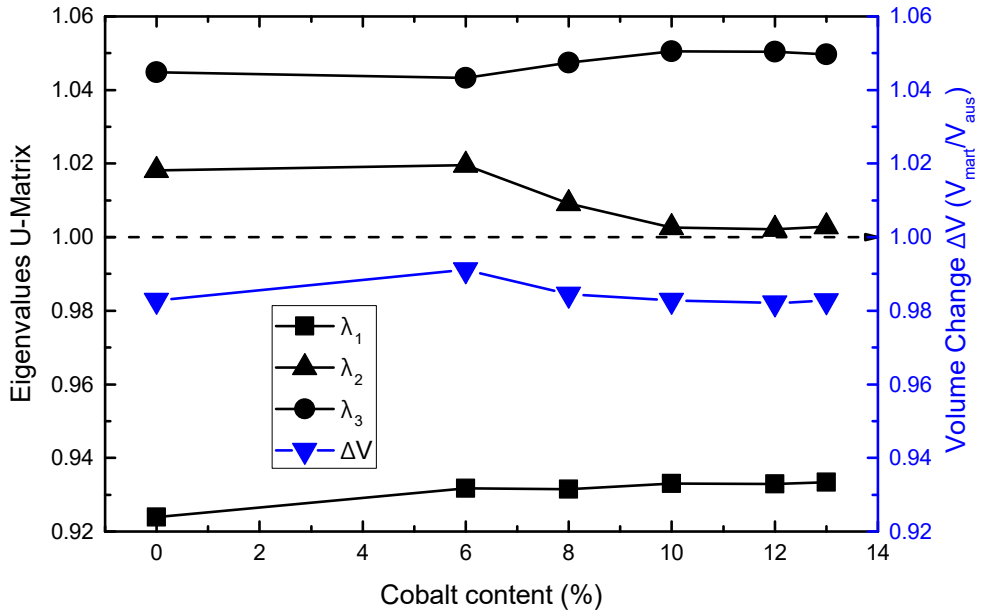

Figure 5.13: Transformation stretch matrix eigenvalues and volume change of the alloys $Ni_{50-x}Co_xMn_{33}Ti_{17}$.

matrix U, as shown in equation 2.7, and the corresponding eigenvalues λ_1, λ_2, and λ_3. The λ_2 value is directly related to the thermal hysteresis and is commonly investigated to analyze hysteresis in NiTi-based shape memory alloys[96], as well as in NiMn-Heusler-based magnetic shape memory alloys[97–99, 158]. For each Co content, the lattice parameters used are determined at temperatures within the phase transition, where both phase fractions are high enough to enable a reliable fit of the unit cells.

While λ_2 is the important eigenvalue for compatibility, λ_1 represents the maximum obtainable transformation compressive strain, and λ_3 represents the maximum obtainable transformation tensile strain during the phase transition. As the Co content increases, λ_2 decreases and approaches unity, indicating enhanced crystallographic compatibility. The most significant change occurs between 6 at.% and 10 at.% Co, which corresponds to the transition from quasi-orthorhombic to monoclinic. Conversely, λ_3 increases in the same range. λ_1 shows a slight increase, reducing the maximum compressive strain. To verify the improved compatibility, magnetization curves of the two samples with 6 at.% and 10 at.% Co of the bulk alloy are shown in Figure 5.14. Both samples exhibit paramagnetism in the austenite phase. Ferromagnetism in the austenite phase at this Ti content becomes apparent around 12 at.% Co. However, the paramagnetic moment for the 10 at.% Co sample is significantly larger. The hysteresis, on the other hand, decreases from 20.5 °C to 15.5 °C, indicating a significant improvement in compatibility at similar transition temperatures. It is expected that further improvements in

compatibility can be achieved through optimized processing and microstructure design, which is also crucial for reducing hysteresis.[159] The compatibility remains close to unity up to 13 at.% Co, but a higher Co content leads to an increase in hysteresis.[24, 27, 28]

Due to the improved compatibility and absence of ferromagnetism, the composition around 10 at.% Co is potentially promising for elastocaloric cooling. In this composition range, the hysteresis is reduced compared to the Co-free alloys, while the change in magnetic entropy remains very small, which is beneficial for maintaining a high adiabatic temperature change, a desirable characteristic in elastocaloric materials [26, 29, 31, 32]. However, since strong ferromagnetism is not a requirement for this purpose and Co is relatively expensive and resource-critical, substituting Co with Fe is promising for further investigation. Fe has a weaker ferromagnetic activation compared to Co but still induces a phase transition to a monoclinic martensite [160].

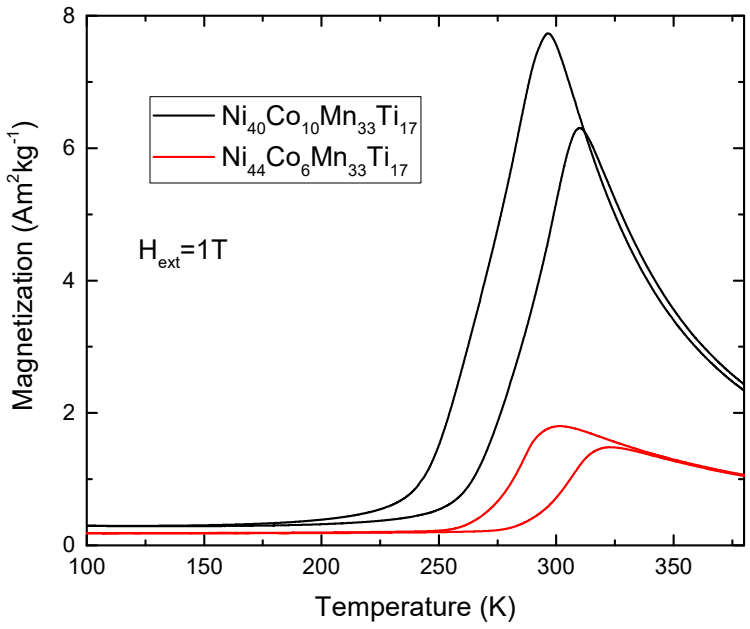

Figure 5.14: Temperature dependent magnetization of $Ni_{44}Co_6Mn_{33}Ti_{17}$ and $Ni_{44}Co_{10}Mn_{33}Ti_{17}$ in an external field of 1 T.

5.4 Diffuse scattering in single crystals

The use of single crystals offers two major advantages in diffraction experiments. Firstly, it allows for discrimination between different directions in reciprocal space, not limited to lattice plane distances. This capability enables a more detailed analysis of diffuse scattering signals, such as the direction of thermal diffuse scattering (TDS). The investigation of anisotropic properties in single crystals is also valuable for applications like ultrasonic measurements of elastic constants or the study of dispersion relations via neutron diffraction. Although these techniques often require relatively large single crystals, diffuse scattering experiments generally works with single crystals larger than 10 μm. Secondly, single crystals provide a larger dynamic range in the signal compared to polycrystalline samples, where signals are diffused into Debye-Scherrer rings instead of sharp diffraction peaks. This expanded dynamic range allows the detection of very weak signals, making single crystals essential for the study of all types of diffuse scattering experiments, since diffuse signals are typically much weaker than Bragg scattering. The choice of the single crystal's composition was driven by the need for a magnetostructural phase transition occurring below room temperature. This choice allows to work in the austenite phase during sample preparation and benefit from a substantial magnetization change at the phase transition. Therefore, the composition $Ni_{37}Co_{13}Mn_{33}Ti_{17}$ was selected for this purpose. It's worth noting that the crystals were extracted from two different initial samples with the same nominal compositions, but slightly different real compositions, resulting in a shift in the phase transition temperature. However, for investigations related to ordering phenomena, these small compositional differences are considered negligible. A secondary heat treatment of 1 h was performed to tune the degree of chemical long range and short range order in the sample. For temperature dependent studies a crystal of sample 1 with a secondary heat treatment of 973 K was chosen. The investigation of SRO was additionally done at room temperature at a crystal of sample 2 with a secondary heat treatment at 773 K. The application of diffuse x-ray scattering addresses two main challenges: First, if a $L2_1$ LRO cannot be established, is there a significant amount of $L2_1$ SRO, which would fulfill the typical Heusler order on a local length scale, while LRO is suppressed by anti-phase boundaries, proving the $L2_1$ ground state in all-d-Heusler alloys. Second, does the elastic instability in these all-d-Heusler alloys differ from the elastic instabilities known in Ni-Mn-Z Heusler alloys with a main group element. The first questions can be answered with an investigation of the SRO diffuse signal and the latter one with an investigation of the temperature dependent TDS. Both diffuse signatures are pre-characterized with laboratory equipment. The main characterization is based on a synchrotron radiation experiment performed at the beamline p21.1 at the Petra3 synchrotron at DESY as described in section 4.2.2.

5.4.1 Motivation for a synchrotron experiment

Using large grains of several millimeters in size, as shown in Figure 4.1(a), laboratory experiments in a four-circle diffractometer in reflection mode can be conducted, while small etched crystals ($<$150 μm) can be measured in transmission with a precession camera. Due to the large grain size in the reflection, only one grain is in focus of the x-ray beam.

For the investigation of short range order (SRO), q scans between fundamental, B2, and $L2_1$-like reflections were performed, as shown in Figure 5.15. Even with the improved signal from a single crystal, no $L2_1$-like ordering is visible. In this laboratory setup, a dynamic range of four orders of magnitude is achieved. To detect possible SRO at the $L2_1$ position, the background must be reduced, and the statistics improved. Background sources in this measurement include device background, electronic noise, air scattering, and surface effects, as only a few micrometers can be probed using Cu K_α radiation.

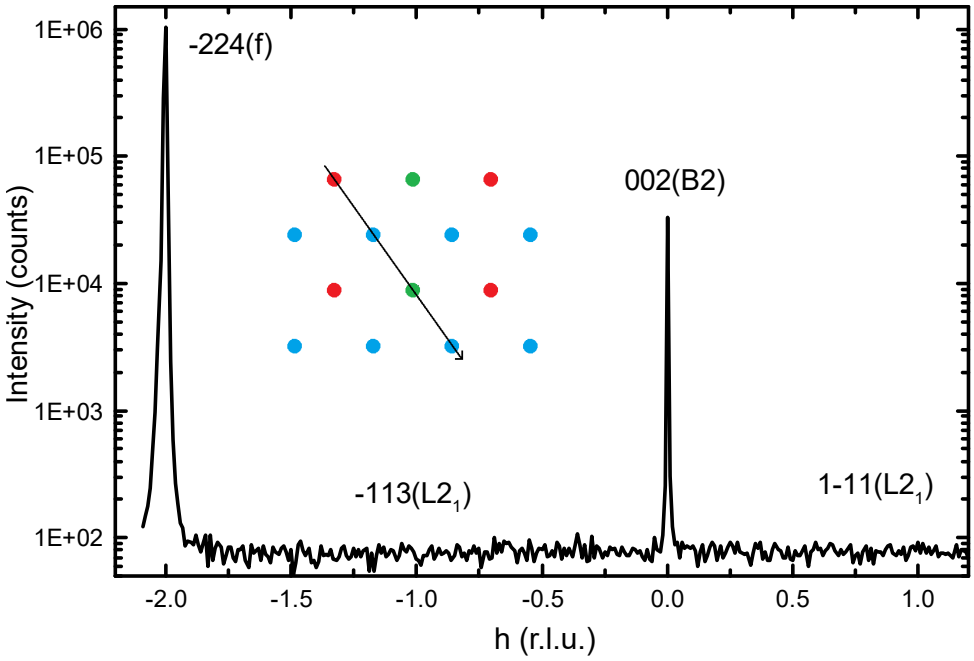

Figure 5.15: Reciprocal space scan of a $Ni_{37}Co_{13}Mn_{33}Ti_{17}$ single crystal using a four circle diffractometer with Cu- Kα radiation along [1 -1 -1] direction, evolving fundamental, $L2_1$ and B2 superstructure reflections. The direction of the scan is illustrated in the insert, where fundamental reflection are red, B2-like reflections green and $L2_1$-like reflections blue.

Using the Buerger precession camera, undistorted reciprocal space measurements of oriented single crystals can be performed[134], as shown in Figure 5.16. Since Ag K_α radiation was used, fewer surface effects are present, and the entire reciprocal lattice plane is captured in

one shot. By measuring the (110) orientation, fundamental, B2, and $L2_1$ typical reflections are all within one plane. As visible in Figure 5.16(a), the image plate detector is susceptible to artifacts at the positions of fundamental Bragg peaks. A long exposure leads to the saturation of Bragg reflections, which then produces streaking in the detector. Since the B2 superstructure reflections are significantly weaker, this does not occur at the B2 positions. At possible $L2_1$ positions, again, no sharp or diffuse signal is present. To overcome the saturation issue, the precession camera can be adjusted to measure not the 0th layer but the 0.1 layer, effectively reducing sharp signals while minimally affecting broad signals like TDS and SRO. The 0.1 layer exhibits a qualitative TDS pattern, which is expected for a B2-like single crystal with high elastic anisotropy, typical for shape memory materials. Quantifying this data, however, is challenging and prone to errors due to significant effects of sample alignment and geometrical corrections of the precession camera geometry. Additionally, this method does not allow for longer measurements due to the decay of the image plate signal over time.

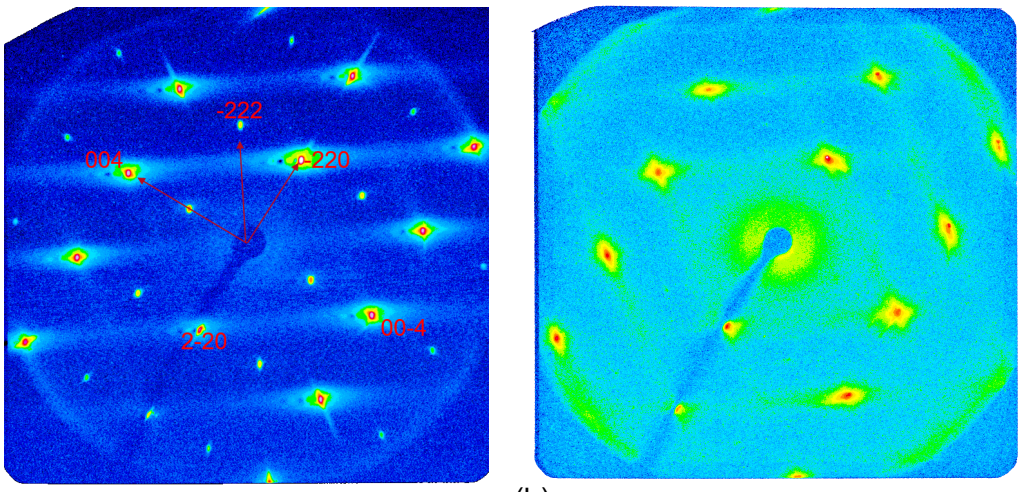

(a) (b)

Figure 5.16: Precession camera images from a ≈150 μm $Ni_{37}Co_{13}Mn_{33}Ti_{17}$ single crystal in 110 orientation (a) of the 0th layer (b) of the 0.1th layer.

High energy -synchrotron experiments resolve the laboratory issues in multiple ways. First, due to the high flux and hybrid photon-counting detectors, the data acquisition rate is exceptionally high, with measurement times of a few minutes for a three-dimensional dataset of the entire reciprocal space - ideally suited for in-situ experiments. The intrinsically noise-free detector also provides an exceptionally high dynamic range, making it ideal for measuring weak diffuse scattering signals. The high energy itself allows for probing larger samples, reducing surface effects and increasing the coherent signal from the sample. [161] Air scattering is therefore reduced compared to the sample signal. The large crystal also permits mounting the crystal without

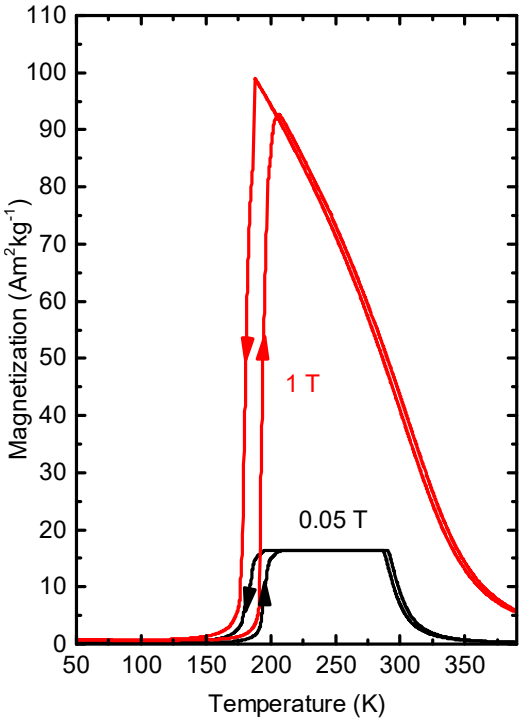

Figure 5.17: Temperature dependent magnetization of the $Ni_{37}Co_{13}Mn_{33}Ti_{17}$ single crystal in a field of 1 T and 0.05 T.

introducing any glue or sample mount into the x-ray beam, which would generate an amorphous signal. Fluorescence is effectively blocked by the detector, leaving Compton scattering as the main incoherent contribution in the diffraction pattern, resulting in a continuously increasing background at higher angles.

5.4.2 Reciprocal space maps

The single crystal used for temperature-dependent measurements and the analysis of elastic constants was heat treated at 973 K. This ensures the maximum obtainable LRO according to the NPD analysis in section 5.1. Lower annealing temperatures for Co-containing samples can lead to decomposition. Therefore, the annealing time was generally chosen to be one hour, which is long enough for short range diffusion processes in the used temperature ranges between 773 K and 973 K but minimizes the potential decomposition at low temperatures. Additionally, precipitates tend to form at defects, such as grain boundaries, which are effectively reduced in a single crystal. The scattering data were recorded during the first cooling of the sample to minimize possible scattering from defects induced by cycling through the phase transition. However, no change in the diffuse scattering can be found after cooling through the phase transition and heating back to the austenite state. The magnetization of the sample is shown in

Figure 5.17, with the phase transition occurring around 190 K during cooling and the T_c around 290 K. The data is reconstructed into reciprocal space coordinates for data interpretation. These 3-dimensional datasets are used for further data analysis. The reconstruction of the raw data in the h-k plane is shown in Figure 5.18 (a). Blank spaces between the signals are due to detector gaps and are filled by applying the Laue symmetry m-3m later. The reconstruction is done with a step size of 0.02 r.l.u. or 0.021 $Å^{-1}$. Increasing the step size to 0.04 r.l.u. improves the statistics of the data, but sharp signals like Bragg reflections will be diluted by the low-intensity regions around them.

There is also a pronounced detector artifact produced by frames with Bragg reflections, which leads to lines in the reconstruction toward the origin. This artifact is commonly found at high x-ray energies and is related to Compton scattering within the sensor layer. [115, 128, 162]

Due to the high symmetry, fewer than 10% of the frames are affected, and the region around the Bragg reflection can be masked for the reconstruction. After implementing a count dependent masking around Bragg reflections and applying the 48 symmetry operations of the point group m-3m, the reconstruction in 5.18 (b) at L=0 and (c) at L=2 is obtained. Around the B2-superstructure reflections, remnants of the Compton streaking remain. The data is dominated by the TDS around the fundamental Bragg reflections in [110]-like directions, which is typical for bcc-like structures with a high elastic anisotropy. This is further discussed in section 5.4.3 . The intensity of the TDS is reduced with temperature as expected, which is visible in Figure 5.18 (d) at 195 K, directly above the phase transition. This also shows that these diffuse features are clearly related to TDS,as other diffuse scattering signatures do not exhibit this strong temperature dependence. By further reduction of the temperature, the martensite phase forms, which is highly twinned and therefore not analyzed here. Heating back to the austenite state recovers the single crystalline state. The B2-ordering reflections also exhibit TDS around them. However, since the TDS intensities are related to the structure factor of the reflections, the TDS is much weaker at superstructure reflections than around fundamental Bragg reflections. The intensity of Bragg reflections can be improved by merging datasets with different attenuators. A limitation arises from the count rate correction of the Pilatus detectors, which only considers the average count rate during one frame, making it unable to correct for local changes in the rate during a constant rotation in single crystal experiments. [163] This leads to an underestimation of Bragg intensities whenever the intensity during the constant rotation temporarily exceeds approximately $1.5 \cdot 10^6$ cps/pixel. Since the actual count rate is unknown in these single crystal experiments and depends not only on the $\Delta\phi$ of the measurement but also on the exact mosaicity of the crystal. The strategy to overcome this problem is to measure with reduced intensity for Bragg reflections and to keep the $\Delta\phi$ of each detector frame small. The used $\Delta\phi$ of 0.1°

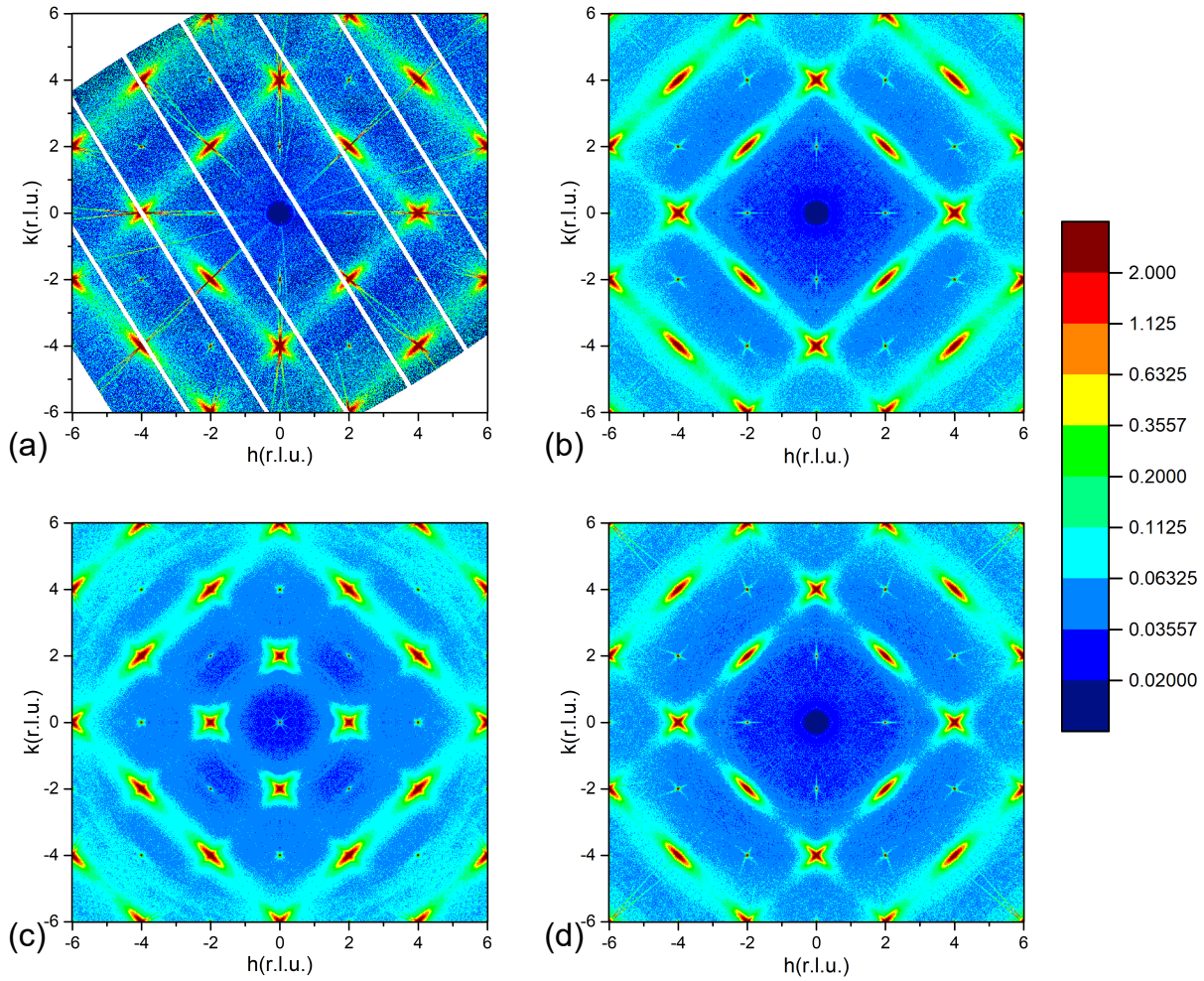

Figure 5.18: (a) Reciprocal space map without symmetry operations and masking at L=0 and 290 K. (b) Reciprocal space map with symmetry operations and masking at L=0 and 290 K. (c) Reciprocal space map with symmetry operations and masking at L=1. (d) Reciprocal space map with symmetry operations and masking at L=0 and 195 K.

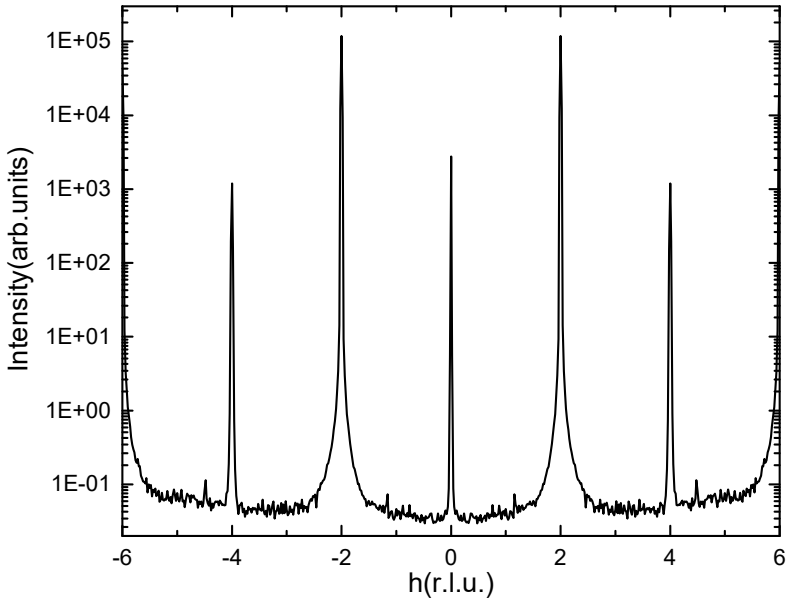

Figure 5.19: Scan along h-direction of the merged dataset at 290 K at l=0 and k=2.

represents a compromise between having a small $\Delta\phi$ and still being able to process the amount of raw data. The crystals themselves have a mosaicity of below 0.1°. Merging these datasets with the high flux dataset to achieve good statistics in the diffuse scattering allows for the analysis of both signals simultaneously. A line scan of such a merged dataset is presented in Figure 5.19. The strongest Bragg reflection, the (220) reflection, is more than 6 orders of magnitude above the background. The B2 ordering reflections, such as the (020) or (420), are still more than 4 orders of magnitude above the background.

5.4.3 Elastic and vibrational properties

The mechanism of the martensitic phase transition in Ni-Mn-Z shape memory alloys is driven by electronic instabilities, leading to an instability in the crystalline lattice.[10, 164, 165] This is explained in more details in section 2.2.1 This lattice instability can be probed by the investigation of phonon modes. These phonon modes can be split into two regimes: a long wavelength limit and a short wavelength regime. The long wavelength limit (close to the Γ point) is characterized by the elastic constants of the material and how sound waves propagate through the material. These tend to show anomalies while approaching the phase transition, such as a reduction of C' and an increase of the Zener anisotropy ratio A. If a pre-martensitic phase

transition is present, they are often associated with an abrupt change in the elastic constants, making them very useful to detect a pre-martensitic phase, as in Ni-Mn-Ga. [80] In the short wavelength regime, the instability is visible by an anomaly in the TA_2 branch, which becomes soft. A soft mode is characterized by a decrease in the phonon frequency in a certain range. This is usually the case around $\frac{1}{3}$[110] in the transverse TA_2 phonon mode for Heusler compounds. [13, 73–75] Since both phonon modes are characterized by a relatively low-frequency region, they lead to high intensity in the thermal diffuse scattering (TDS), making diffuse scattering in single crystals an ideal tool to investigate both regimes at the same time. The TDS of Ni-Mn-Ga alloys has been investigated several times in the literature to study the vibrational instability of the soft TA_2 mode. [3, 4, 76, 77] Since this mode is very pronounced in Ni-Mn-Ga, it can be observed in satellites in the diffuse scattering. To calculate the complete TDS, a phonon dispersion is necessary, or it could otherwise be calculated from the TDS data [123]. However, due to the significant amount of disorder in the system, accurately modeling phonon modes is highly complicated. Despite the need for complete modeling, some information about the TA_2 branch can be obtained by applying certain approximations.

An investigation of elastic constants in a shape memory material via TDS has never been published so far. However, the investigation of elastic constants by TDS is a well-established technique [120], which has become more popular nowadays due to advances in synchrotron sources and noise-free x-ray detectors. [125–128, 166] This makes these measurements fast and allows for in-situ studies. A detailed view of the three-dimensional structure of the TDS is shown in Figure 5.20. The isosurface representations of the diffuse scattering around the (400) and (220) reflections are displayed. The most pronounced feature in both cases consists of rods in the [110]-like direction, indicating that the lattice is particularly sensitive to deformation in the [110] direction. In contrast to the (400) reflection, the (220) reflection exhibits a broad streaking along the [-110] direction. Both phenomena correspond to the TA_2 phonon mode but differ in the phonon structure factor. [77, 167, 168]

Since the signal is most pronounced in the (220) reflection, it will be used for further analysis of the TA_2 phonon branch in Section 5.4.3. A quantitative analysis of the elastic constants as the martensitic phase transition is approached will be presented in the following section. For this analysis, all fundamental reflections will be utilized. Subsequently, the analysis of the TA_2 phonon branch will be presented.

Elastic constants

The investigation of elastic constants is of paramount importance in shape memory materials as they often serve as precursor phenomena to phase transitions. However, to date, there are no

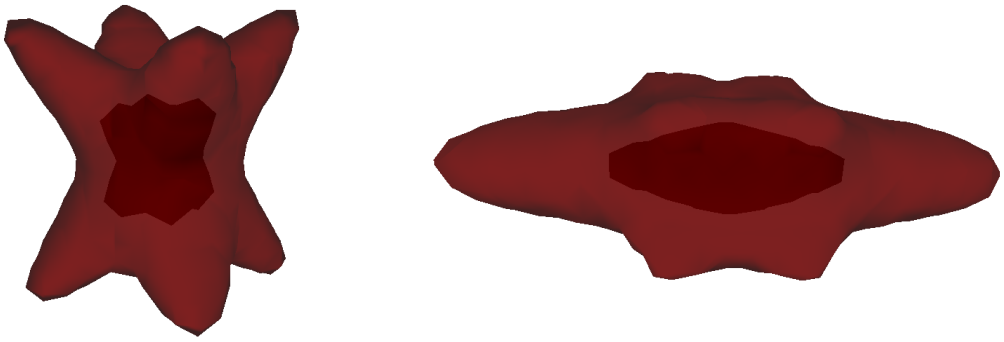

(a) (b)

Figure 5.20: Isosurface representation of the TDS of (a) (400) Bragg reflection at 290 K. The diffuse rods are in [110], [-110], [101], [-101] directions (b) (220) Bragg reflection at 290 K. Small diffuse rods along [011], [101], [-101], [0-11] direction and big diffuse rod along [-110] direction.

reported experimental elastic constants for Ni(Co)MnTi. Determining elastic constants from the TDS data is a multi-step process. At temperatures where the austenite phase is stable, only the ratios of elastic constants can be obtained since the measurements are not in absolute units. In principle, at lower temperatures, absolute values could be obtained through a two-temperature fit. However, this approach requires that different phonon branches exhibit significantly different behavior when the temperature changes. Such a condition can be met if one phonon branch has an energy of $2k_bT > \hbar\omega$, while another branch has an energy of $2k_bT < \hbar\omega$ within the corresponding ROI. In the case of Ni(Co)MnTi, achieving temperatures significantly below 100 K would be necessary, which is not feasible if the experiment aims to measure the elastic instability close to the martensitic phase transition around 190 K. Consequently, the relative values of the elastic constants must be re-scaled to an isotropic elastic modulus measured on a polycrystalline material. In this case, nanoindentation was conducted on a polycrystalline sample with the same nominal composition as the single crystal investigated in the diffuse scattering experiment. Nanoindentation provides the average elastic response within the probed volume and should therefore be less affected by different crystalline orientations.

Nevertheless, to completely eliminate any orientation-dependent effects, the measured indentation modulus is averaged over 25 different spots representing various crystalline orientations. The region of the sample that was measured is depicted in the EBSD map in Figure 5.21(a). The positions of the 25 indents are visible in the image quality map in Figure 5.21(b), and the corresponding load-displacement curves are shown in Figure 5.21(c). The indentation modulus is determined from the slope of the deloading curve and yields an average value of 115.7 GPa

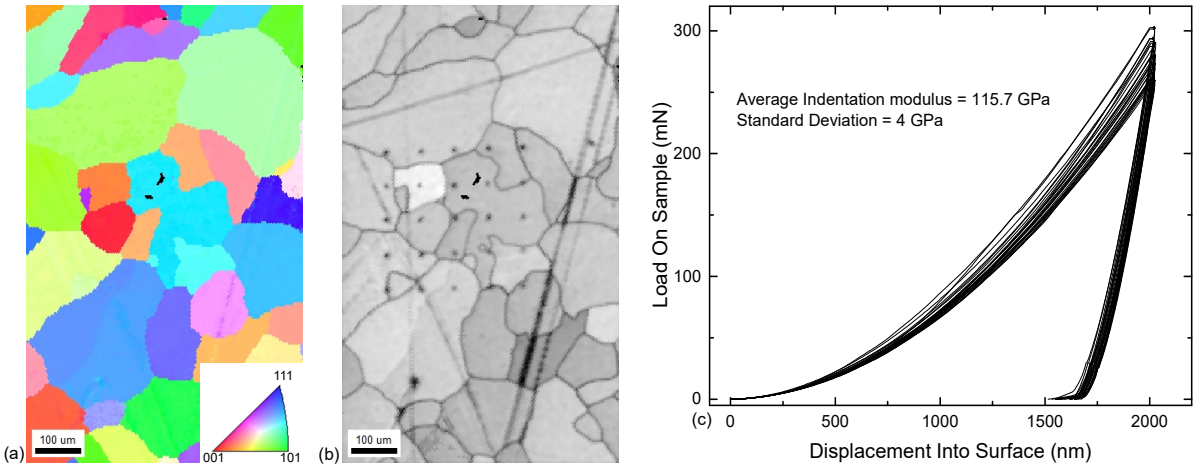

Figure 5.21: (a) Electron backscattering diffraction (EBSD) map with of the area used for nanoindentation. The inverse polefigure for the colorcode of crystallite orientations is shown in the insert. (b) Image quality map of the same area for showing defects in the sample surface. Showing grain boundaries, scratches from polishing and the position of the 25 indents visible. (c) Load-Displacement curves of all 25 indents.

with a standard deviation of only 4 GPa, indicating that the effect of crystalline orientation is negligible.

This indentation modulus should be equivalent to the isotropic Young's modulus, allowing us to utilize equations 4.3, 4.4, and 4.5 to rescale the ratios of the elastic constants to absolute values. Notably, the Young's modulus is significantly lower when compared to Heusler alloys containing main group elements. For instance, Ni_2MnGa and $Ni_{49.3}Mn_{34.2}In_{16.5}$ have Young's moduli of 165 GPa and 151 GPa, respectively.[75, 169] This discrepancy can be attributed to differences in bonding types, with Ni-Mn-Z alloys exhibiting a stronger covalent character due to p-d hybridization, whereas all-d-Heusler alloys feature weaker d-d bonding, which enhances ductility.[35, 170] The data fitting process was carried out using the TDS2EL2 software package, where the data is fitted on the raw data within the specified ROI for all fundamental Bragg reflections. An exemplary fit is illustrated in Figure 5.22, where the upper part displays the raw data, and the lower part shows the corresponding fit. Even though the data seems to be noisy within one detector frame, over 10^6 pixels are used in the fit to obtain only two elastic constants, making the fit highly stable and reliable. To mitigate any potential influence of scattering unrelated to TDS, such as the weak Debye-Scherrer rings, a two-temperature fit is performed using the temperatures 290 K and 250 K. This approach assumes that the elastic constants remain unchanged in this temperature range and effectively subtracts all signals unaffected by

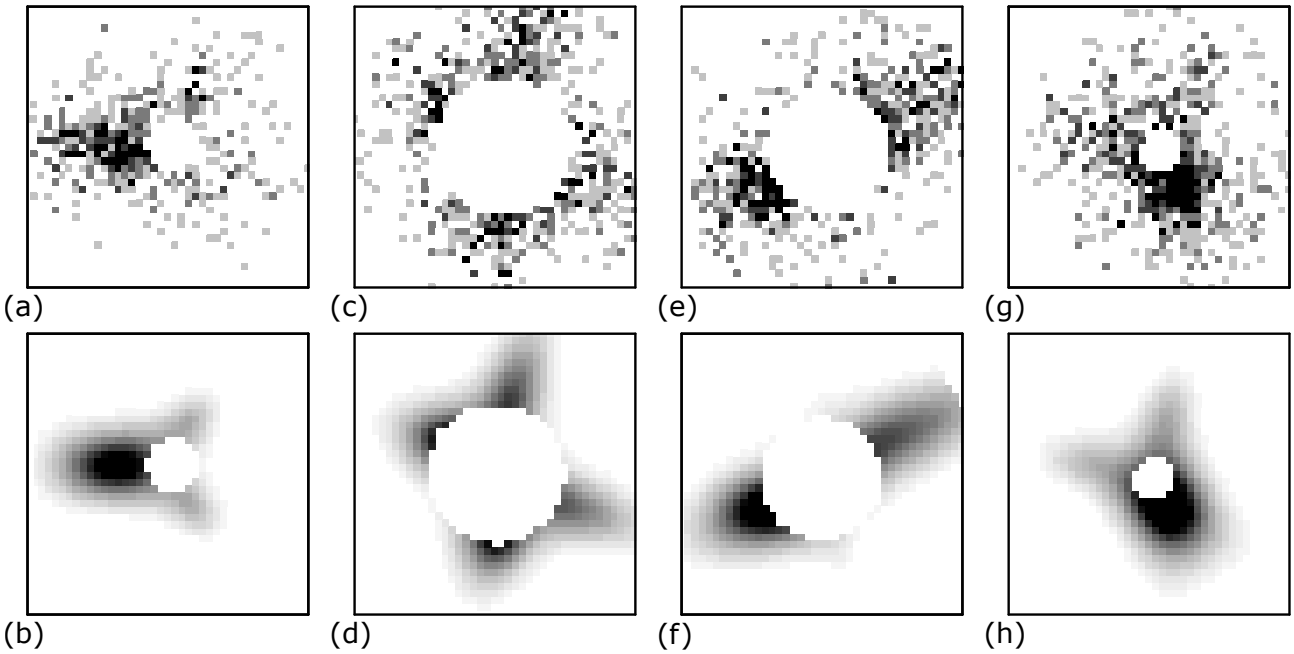

Figure 5.22: Raw data(upper part) and fit(lower part) of the thermal diffuse scattering for different, representative reflections. (a,b) (220); (c,d) (400); (e,f) (422) and (440) (g,h) reflections.

temperature variations.

To analyze the temperature dependence, the change in elastic constants relative to their values at 270 K (set to 1) is determined using single-temperature fits. This approach is chosen because two-temperature fits require a substantial change in TDS intensities, which is not observed for small temperature steps. It should be noted that the change in the C_{11} constant and the isotropic Young's modulus is neglected in this case, even though they typically exhibit slight increases upon cooling. In Figure 5.23 (top), the variations in the shear elastic moduli C' and C_{44} between 290 K and 195 K in the austenite phase are shown. Both moduli exhibit a consistent increase during cooling, indicating the absence of a pre-martensitic phase transition.

Table 5.5: Values of elastic constants out of fitting of thermal diffuse scattering data; rescaled by the indentation modulus determined in Figure 5.21.

Elastic Constant	TDS (270 K)
C_{11}	103.4 GPa
C_{12}	90.8 GPa
C_{44}	70.6 GPa
C'	6.3 GPa
Young's modulus Y	115.7 GPa
Anisotropy Factor	11.3

It's worth noting that this increase is typically observed for C_{44}, but not for C', in shape memory materials as they approach the martensitic phase transition. Besides the change of a single elastic constant, the ratio between the shear elastic constants is from importance to describe the stability of the cubic structure. This is quantified using the Zener anisotropy ratio, denoted as A and shown in Figure 5.23 (bottom). It exhibits a minor decrease from 290 K to 235 K, followed by a significant increase up to a value of 11.6. A higher elastic anisotropy implies an elastic instability of the cubic crystal structure [78]. It's important to note that materials typically have fixed values of the elastic anisotropy at the phase transition, but these values can differ among different material classes. The observed increase in C' may be related to magnetic interactions within the structure, which serve to stabilize the austenite phase. With a T_c around 290 K, the magnetic interactions become significantly more pronounced during the cooling process, resulting in lattice hardening. This effect is also reflected in the phase diagram of $Ni_{50-x}Co_xMn_{35}Ti_{15}$ as reported by Wei et al. [24]. As soon as the austenite phase becomes ferromagnetic, the high-temperature phase experiences increasing stabilization. In cases with lower Co content and a paramagnetic austenite, the influence of Co content on the phase transition temperature is relatively weak. This interplay between the shear elastic modulus C_{44} and C' ultimately governs the phase transition, underscoring the complex nature of martensitic phase transitions in ferromagnetic all-d-Heusler alloys.

Phonon softening

The intensity of the previously described diffuse feature associated with the (220) reflection in the [-110] direction is shown in Figure 5.24 (top) for temperatures of 290 K, 240 K, and 195 K. In contrast to Ni-Mn-Ga, there is no well-defined maximum[130] indicative of a soft mode, and there is no anomalous change in intensity upon cooling; the diffuse scattering (TDS) decreases continuously. In the high-temperature limit with $2k_bT >> \hbar\omega$, the diffuse intensity in equation 3.15 from TDS can be approximated using equation 3.17 with the proportionality $I_{TDS} \sim \frac{T}{\omega^2_{k,\nu}}$. Since typical soft mode phonon frequencies for Ni-Mn-Heusler alloys are below 5 meV [75, 171], this approximation is valid for the TA_2 mode at the temperatures used. In the high-temperature limit, the intensity increases linearly with temperature, which can also be observed here. Using this high-temperature approximation, the phonon dispersion of the TA_2 mode can be constructed in Figure 5.24 (bottom). Since the initial slope of the phonon dispersion is related to the C' value over the speed of sound, the dispersion can be converted to absolute values of the phonon energy using equation 2.5 and the calculated absolute value of C'. In both intensity and dispersion, it can be seen that the slope changes around $\xi = 0.15$, which marks the beginning of a small soft mode anomaly. This behavior corresponds to the

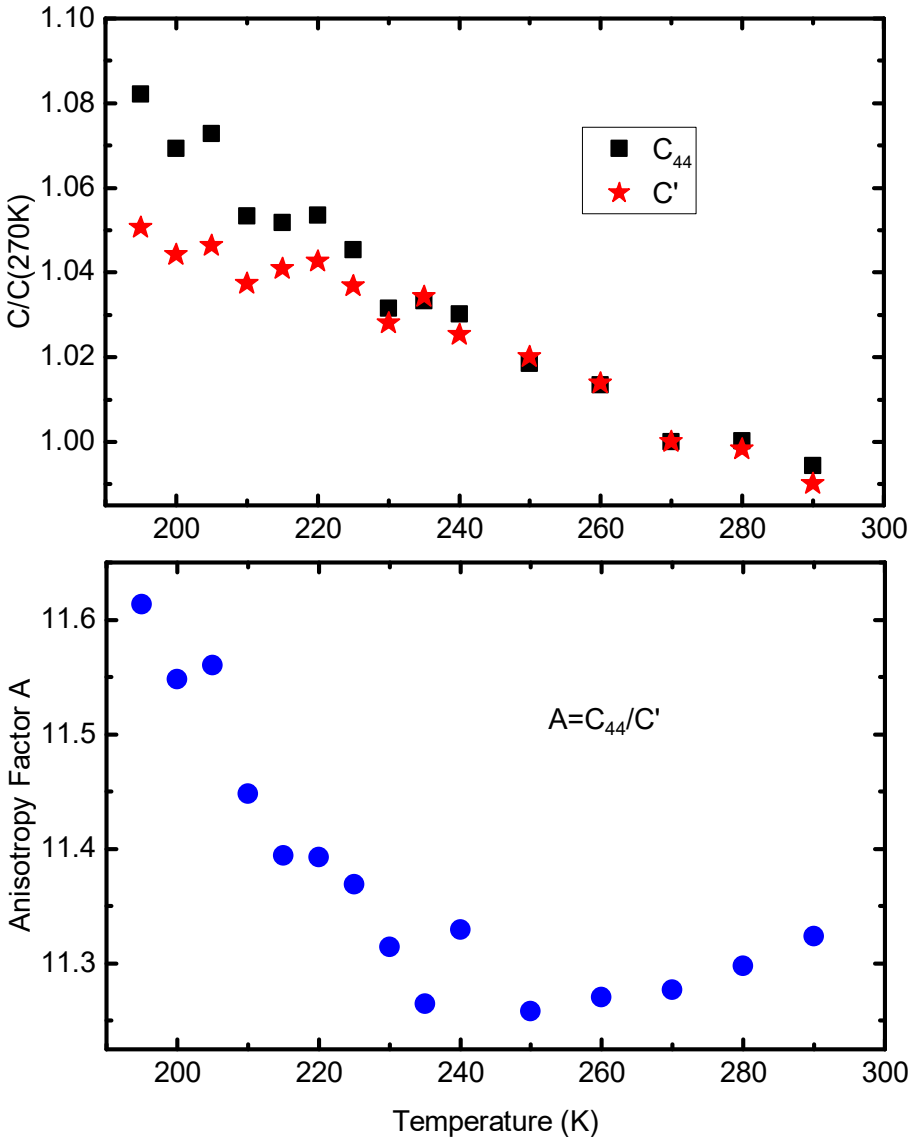

Figure 5.23: Temperature dependence of the shear elastic constants C_{44} and C' and the anisotropy factor A.

typical anomaly seen in Ni-Mn-Z Heusler alloys with main group element Z. Here, the soft mode centers around $\xi = 0.28$, but it does not exhibit significant changes with temperature.

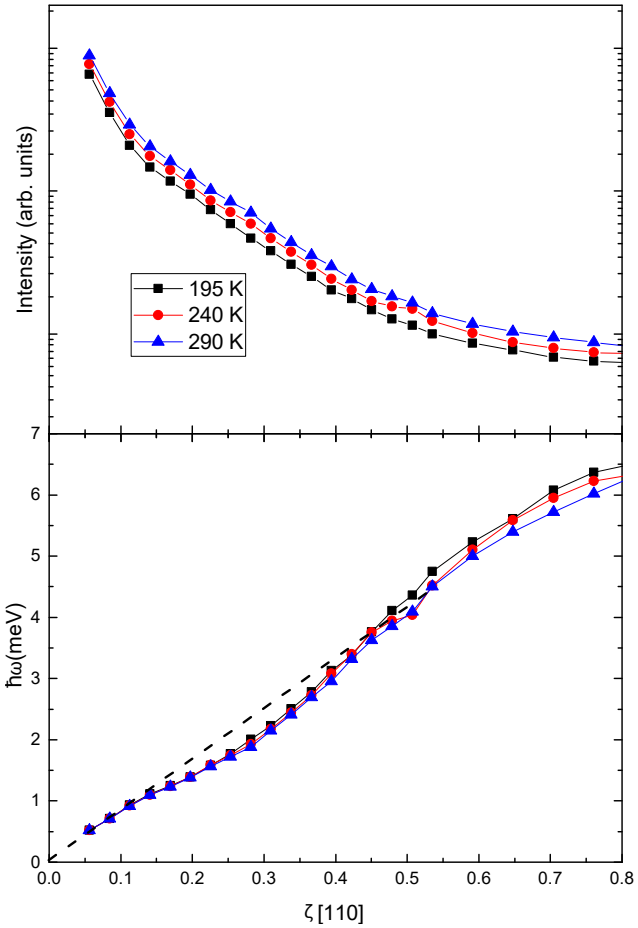

Figure 5.24: Qualitative phonon dispersion and corresponding TDS intensities for the TA_2 mode for different temperatures the dashed line is a guide to the eye.

In main group element Heusler alloys, the degree of softening varies depending on the main group element and the exact composition. Stoichiometric Ni_2MnGa exhibits the most significant softening, but this effect generally becomes less pronounced as the alloy becomes off-stoichiometric [172]. In other Heusler compounds such as Ni-Mn-In and Ni-Mn-Al, the phonon mode is still well pronounced but to a lesser extent than in Ni_2MnGa [75, 171]. It's worth noting that Ni_2MnGa is the only Ni-Mn-Z-Heusler compound that undergoes a martensitic phase transition while being stoichiometric.In In- Sn- or Al- Heusler alloys, excess Mn is added to shift the martensitic phase transition to higher temperatures, which reduces the degree of order since Mn atoms occupy Z element sites.

Several factors may contribute to the low degree of softening observed in the $Ni_{37}Co_{13}Mn_{33}Ti_{17}$ system. First, the strong softening observed in Ni_2MnGa can be related to a strong spin-phonon

coupling, which might be reduced in the $Ni_{37}Co_{13}Mn_{33}Ti_{17}$ system. Additionally, in the Ti-based system, no $L2_1$ LRO can be established, which could further reduce the degree of softening. The higher Co content in $Ni_{37}Co_{13}Mn_{33}Ti_{17}$ compared to Ni-Mn-Heusler alloys with main group elements also increases the amount of disorder compared to a perfectly ordered system, which can affect Fermi surface nesting and consequently the softening behavior. The observation that the soft mode does not become more pronounced during cooling could be related to magnetism. The T_c in this alloy is close to room temperature and therefore the magnetic moment is increasing significantly upon cooling. The magnetism is known to stabilize the austenite structure for all-d-Heusler alloys.[24] Furthermore, Co is used in Ni-Mn-Z alloys to enhance the Curie temperature, but in all-d-Heusler alloys, Co is needed to establish ferromagnetism at all by ferromagnetic activation of the Mn moments via local Mn-Co-Mn configurations.[25] In contrast to Ni-Mn-Ga, which exhibits ferromagnetism even without Co addition, and where phonon softening is enhanced by the T_c [73, 173], the $Ni_{37}Co_{13}Mn_{33}Ti_{17}$ system displays a relatively low degree of softening. Additional phonon measurements conducted above room temperature and the phonon dispersion of a Co-free sample could provide valuable insights into the extent of softening in this system. However, despite the lower degree of softening, a similar phonon anomaly as observed in Ni-Mn-Z Heusler alloys is still present. This behavior, however, does not hold true for all shape memory materials. An exception can be found in Co-rich Co-Ni-Ga alloys, which undergo a martensitic phase transition. Interestingly, no soft mode has been observed either experimentally or theoretically. [174] This suggests that Fermi surface nesting plays a role in the electronic instability leading to the martensitic phase transition in all-d-Heusler alloys, analogous to the Ni-Mn-Z Heusler compounds. Further theoretical work is needed to determine which electronic states are responsible for the Fermi surface nesting and, consequently, the electronic instability. As for Ni_2MnGa, a low-lying optical phonon is suspected to induce the softening in the TA_2 branch[9, 10], but a complete modeling of the phonon dispersion would enhance the understanding. This can be, in principle, also modeled with TDS[123]. However, since the TDS data is dominated by low-energy phonons, the accuracy in the optical phonons will be limited. There, an inelastic neutron scattering experiment on a large single crystal will provide valuable insights into the complete phonon dispersion of all-d-Heusler alloys.

5.4.4 Short range order

Various theoretical studies suggest that the $L2_1$ structure is energetically more favorable than the B2 structure for Ni(Co)MnTi alloys [31, 34]. However, experimental evidence has consistently shown that the long range ordering (LRO) of Ni(Co)MnTi remains in the B2 structure, with random distribution of Ni/Co at one site and Mn/Ti at the other site. It's important to note that complete randomness at all temperatures within these lattice sites is unlikely, and some level of correlations can persist above a critical long range ordering temperature, diminishing as temperature increases [110]. Locally ordered clusters can form, as observed in Fe-Ga alloys, where the size of these clusters depends on the thermal history and composition [103–105].

This issue of SRO in all-d-Heusler alloys is closely related to the investigation of SRO in high-entropy alloys HEA, where theoretical predictions also suggest the presence of SRO between dissimilar d-metal elements while LRO is suppressed [117–119]. In both HEA and all-d-metal Heusler alloys, the weak contrast for diffuse x-ray scattering due to the close atomic numbers of the d-metals makes the experimental determination of SRO challenging. As contrast to the HEA, for the all-d-metal Heusler alloys also LRO is present and known. Therefore, no correlations between all elements have to be taken into account but only correlations between Ni/Co and between Mn/Ti, reducing the problem to two binary cases. For x-rays the signal from SRO will be dominated by the Mn/Ti sublattice. The difference in form factor is approximately 3 times larger(f ≈Z) for $(f_{Mn} - f_{Ti})$ than $(f_{Ni} - f_{Co})$. Since any SRO signal is proportional to $(f_i - f_j)^2$ this leads to a ≈9 times higher signal from the Mn/Ti sublattice for the same degree of SRO. In case of a tendency to form $L2_1$ order, SRO would manifest itself in diffuse maxima around the position of superstructure reflections which are related to the $L2_1$ ordering, namely all with only odd indices like (111), (311) or (331). Size effect diffuse scattering could additionally shift the position slightly from the nominal position.

Especially suitable for this investigation is a Reciprocal space map (RSM) in the (110) orientation(as for the precession images in figure 5.16), since it encompasses all characteristic crystallographic directions ([100], [110], [111]) and includes fundamental, B2, and $L2_1$ superstructure reflections. Distinguishing between different sources of diffuse scattering can be challenging. To identify regions around the potential superstructure reflections that are not related to TDS, which is the dominant source of diffuse scattering, diffuse scattering at the temperatures 290 K and 195 K in the 110-like orientation is presented in Figure 5.25. Given the broad nature of diffuse scattering, the array resolution can be reduced to 0.08 r.l.u. without any loss of information regarding the diffuse features, resulting in improved data statistics. Please note that the color coding in this figure differs from that in Figure 5.18 to highlight smaller signals and changes in the data.

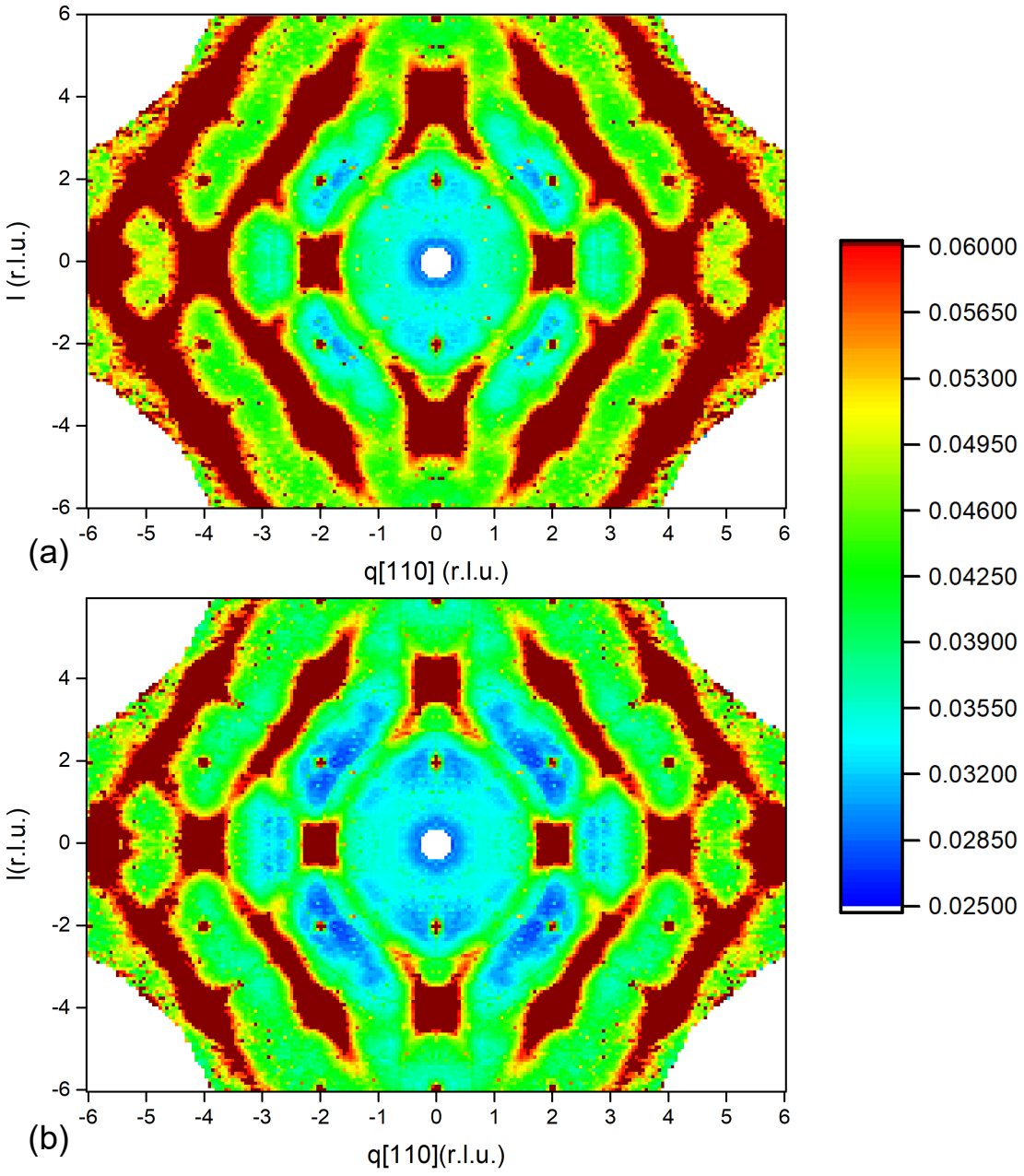

Figure 5.25: Reciprocal space map of the diffuse scattering in $Ni_{37}Co_{13}Mn_{33}Ti_{17}$ after heat treatment at 973 K in the (110) orientation at (a)290 K and (b) 195 K .

The reduction in temperature and the higher binning of the data have unveiled a diffuse ring close to the center but have not revealed any visible diffuse SRO features at the corresponding positions. Due to the decrease in the form factor and the increase in TDS and Compton scattering with higher values of q, the most promising signal is observed close to the origin, at the (111)-like positions. To investigate if there is any difference in the diffuse scattering that is unrelated to the diffuse ring and TDS, q-scans were performed from the origin for both 195 K and 290 K along [111] and [001] directions, as shown in Figure 5.26. The [110] direction, which is strongly affected by TDS, has been omitted for clarity. It is evident from the scans that there is no significant difference in the diffuse scattering along both directions at the position corresponding to the (111) reflection, both at 290 K and 195 K, respectively. Therefore, no signal from short range $L2_1$ order can be observed. Additionally, attempts to enhance the measurement statistics by summing up 16 single measurements at 195 K or by increasing the measurement time while blocking Bragg spots with tungsten discs have not revealed any features related to $L2_1$ SRO as well.

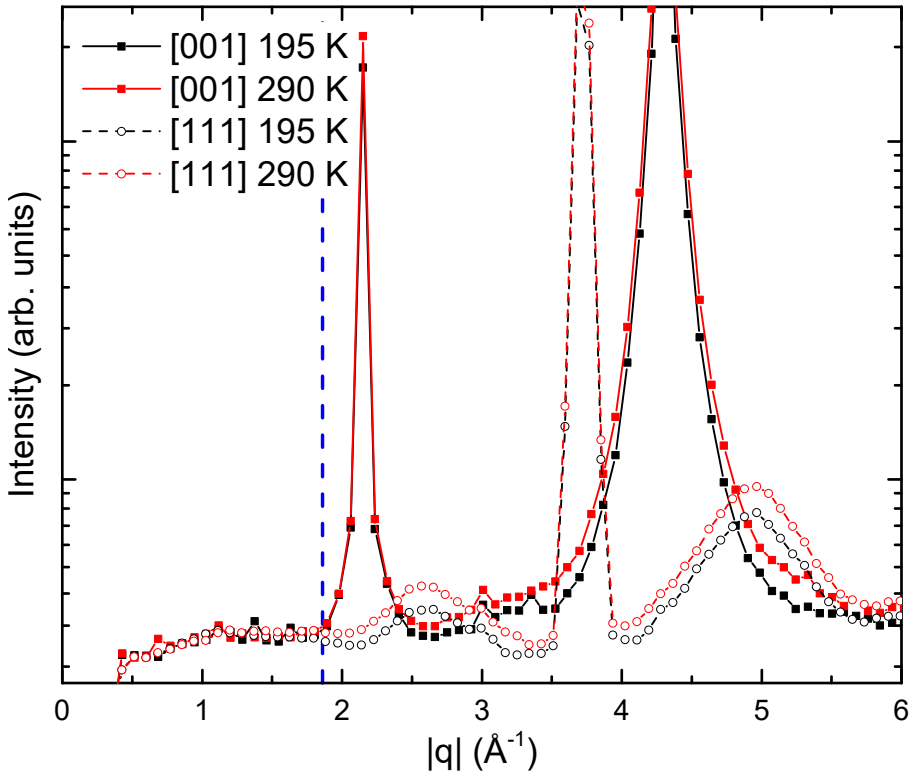

Figure 5.26: q-scans of diffuse scattering along [001] and [111] directions for 195 K and 290 K. The position of the (111) superstructure reflection is marked with the blue dashed line. Note that Bragg intensities are completely omitted in this reconstruction.

In the case of no SRO , one would expect Laue monotonic scattering, which is described

by equation 3.14. The intensity of the Laue monotonic scattering for a disordered system is often referred to as one Laue unit and can be used to describe diffuse scattering in absolute terms. To express the intensity of the background in terms of Laue units, a calibration of the beam intensity using a well-defined scatterer (e.g., C_8H_8) with the exact same probed volume is typically required.[175, 176] However, this calibration was not feasible in the transmission experiment with a not perfectly shaped single crystal. The monotonic background is defined by the corresponding phase fractions and the difference in atomic form factors. Figure 5.27 shows the simulated Laue monotonic scattering for random Mn/Ti positions and random Ni/Co positions. The phenomenological shape of the Compton scattering background is displayed in the insert, which is responsible for the overall increase in the background observed in the experimental data. Due to the larger difference in form factor, the Mn/Ti Laue monotonic signal would be much larger and would be very close to the total Laue monotonic scattering for the completely disordered case. For simplicity, the contribution of Ni/Co is excluded in the following discussion, since the contribution would be overshadowed by the Mn/Ti site anyway. Due to the difference in the angular dependence of the scattering factors of Mn and Ti, as described in equation 3.6, the Laue monotonic scattering exhibits a peak around 1.27Å^{-1} and decreases as q increases. Additionally, the signal from air scattering, approximated by nitrogen, is shown, and it has a steeper decline with increasing q but still decreases overall. The position and shape of the diffuse ring observed in Figure 5.25 roughly corresponds to the peak of the theoretical Laue monotonic scattering from randomly distributed Mn/Ti sites or the sum of both sites. Other types of scattering, such as air scattering, have different angular dependencies and lack this characteristic peak. Moreover, no glue or glass rod was in the x-ray beam during the experiment, which could contribute to a diffuse ring from an amorphous structure. However, it's worth considering the possibility of Ti-O-N impurities (commonly present in arc-molten samples in the literature, e.g., [27, 31, 177]) or traces of epoxy glue as alternative sources for this diffuse ring. However, due to the large sample size effects from the sample mounting should not be present, although traces of glue cannot be entirely ruled out.

If this diffuse ring is indeed caused by Laue monotonic scattering, it would indicate that there is no enhanced probability for a Mn atom to have either a Ti or a Mn atom at the next position of the Mn/Ti sublattice different from what is given by the average composition of the sample.

Lowering the annealing temperature would potentially enhance SRO and therefore reduce Laue monotonic scattering. Unfortunately, lowering the annealing temperature below 973 K can lead to the formation of $(Ni,Co)Ti_3$ precipitates. For the formation of precipitates in comparison to the formation of SRO, long range diffusion is necessary, and the process is therefore rather slow. Additionally, precipitates tend to form at grain boundaries and defects, which are strongly

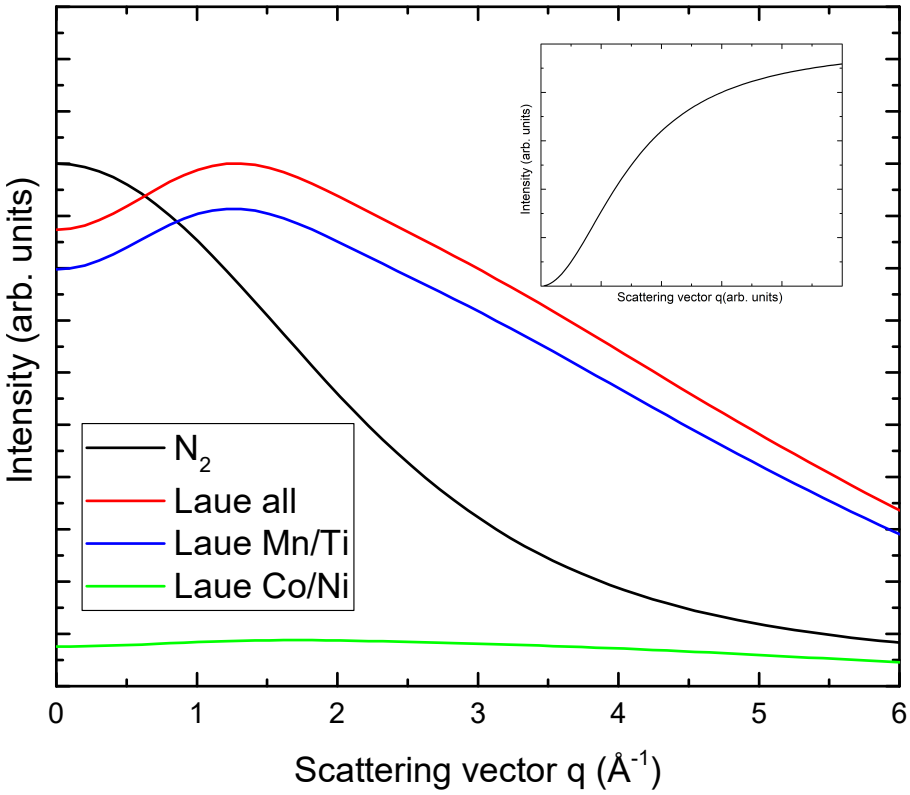

Figure 5.27: Angular dependency of possible coherent scattering contributions of the background in the reciprocal space maps. The Compton scattering form in the insert is modelled after [178].

reduced in the single crystalline sample, minimizing the formation of precipitates.

To test the hypothesis of Laue monotonic scattering in the 973 K annealed sample and if SRO can be established at lower temperatures, the data is compared to samples aged at lower temperature. While after annealing at 873 K, no $L2_1$ SRO was found, annealing at 773 K changes the diffuse scattering. The RSM of the (110) layer of the sample aged at 773 K is shown in Figure 5.28(a).

Unlike the sample annealed at 973 K in Figure 5.25, the diffuse ring is gone, and the background is only continuously increasing. Instead, diffuse features appear around the (111) position, as expected for $L2_1$ SRO. This can be directly seen in the scan in Figure 5.25 (b), where there is a significant difference in intensity along the [111] direction compared to the [100] direction, which was absent in Figure 5.26. Since the background is continuously increasing by scanning through the origin, the profile of the signal at the (111) position is not clearly visible. This can be improved by scanning in different directions, as shown by the q-scans in Figure 5.29(a) in [11-1] direction and (b) [100] direction. These diffuse features are highlighted by the scans through the (111) position in different directions. In Figure 5.28 (b), the sample is scanned in the [11-1]

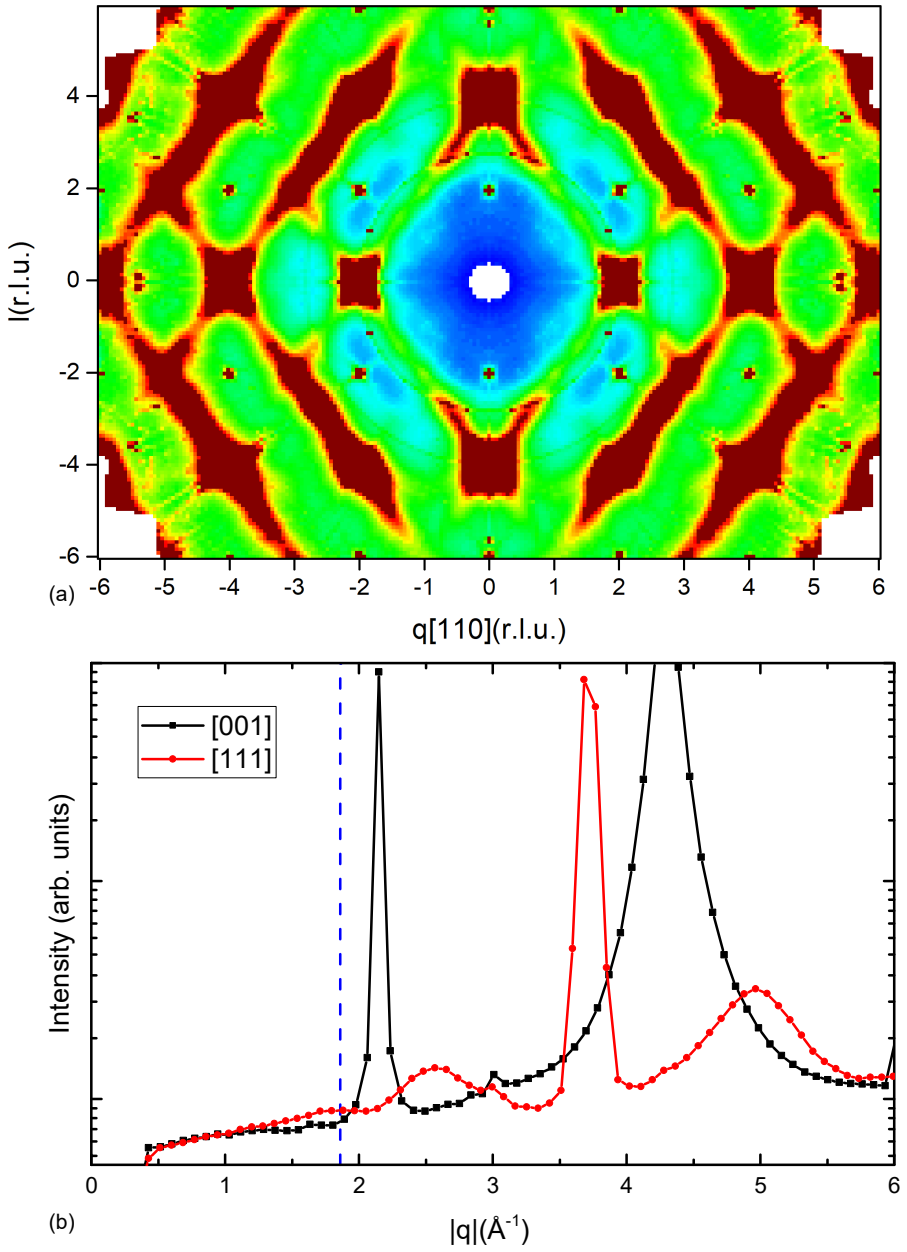

Figure 5.28: (a) Reciprocal space map of the diffuse scattering in $Ni_{37}Co_{13}Mn_{33}Ti_{17}$ after heat treatment at 773 K in the (110) orientation.(b) q-scans of diffuse scattering along [001] and [111] directions.

direction, showing the TDS of fundamental and B2-like reflections and TDS in between. The scan along the [100] direction in Figure 5.28 (c) shows the maximum at the (111) position as well. Since no other Bragg reflection is within this line scan, the increasing background due to Compton scattering and TDS is highlighted, making the possible further $L2_1$-like reflections invisible in the background, since the intensity of those reflections would be further reduced due to the reduction of the x-ray form factor, as seen in the Laue monotonic scattering in Figure 5.27. The SRO signal is not notably shifted from the nominal position, indicating a negligible size effect in diffuse scattering.

The weakness of this SRO signal does not allow for a reliable evaluation of the SRO in terms of Warren-Cowley SRO parameters. The occurrence of the SRO signal at one site and the vanishing of the diffuse ring at the other site support the idea that the diffuse ring at higher annealing temperatures is due to Laue monotonic scattering from a random distribution of Mn/Ti atoms. However, epoxy glue does have to be identical in different samples and could be an additional factor for the intensity of the diffuse intensity at the position of the Laue monotonic scattering. Therefore, the presence of SRO signals after annealing at 773 K and the absence of SRO signals after annealing at 973 K is a more reliable argument than the presence of the ring itself.

Since all samples produced in the literature have annealing temperatures of 973 K and higher, it is highly likely that all of these samples have a pure random distribution of Mn and Ti atoms. The shape of the SRO region can be used to calculate the correlation length of ordered clusters by the inverse FWHM.[103] This gives a correlation length of the $L2_1$ SRO clusters of 2.5 $L2_1$ unit cells or 1.5 nm.

This can be compared with the literature on Fe-Ga, which also has a bcc-like structure, and SRO is heavily investigated. [103–105] There, DO_3 and B2 SRO is investigated, which form ordered clusters as well. The DO_3 structure has the same symmetry as the $L2_1$ structure, but with only two different atoms, therefore, the structures are very similar. In the case of FeGa, SRO is also found after annealing at 1273 K, followed by water quenching, but it increases if the sample is cooled to room temperature with a rate of 10 K/min. Strong SRO signals, comparable to the TDS signals, can be observed there, indicating a much higher tendency for ordering. This can be explained by a significantly higher tendency for the formation of an $L2_1$ ordered structure driven by p electrons from the main group element. However, the tendency for the formation of an $L2_1$ structure also exists for Ti without any p electrons but is hindered by sample decomposition and kinetics. Additionally, it has to be noted that a longer annealing temperature does not necessarily result in LRO, since these SRO correlations can exist far above a potential ordering temperature. [110] Furthermore, the intensity of the SRO signal is close to

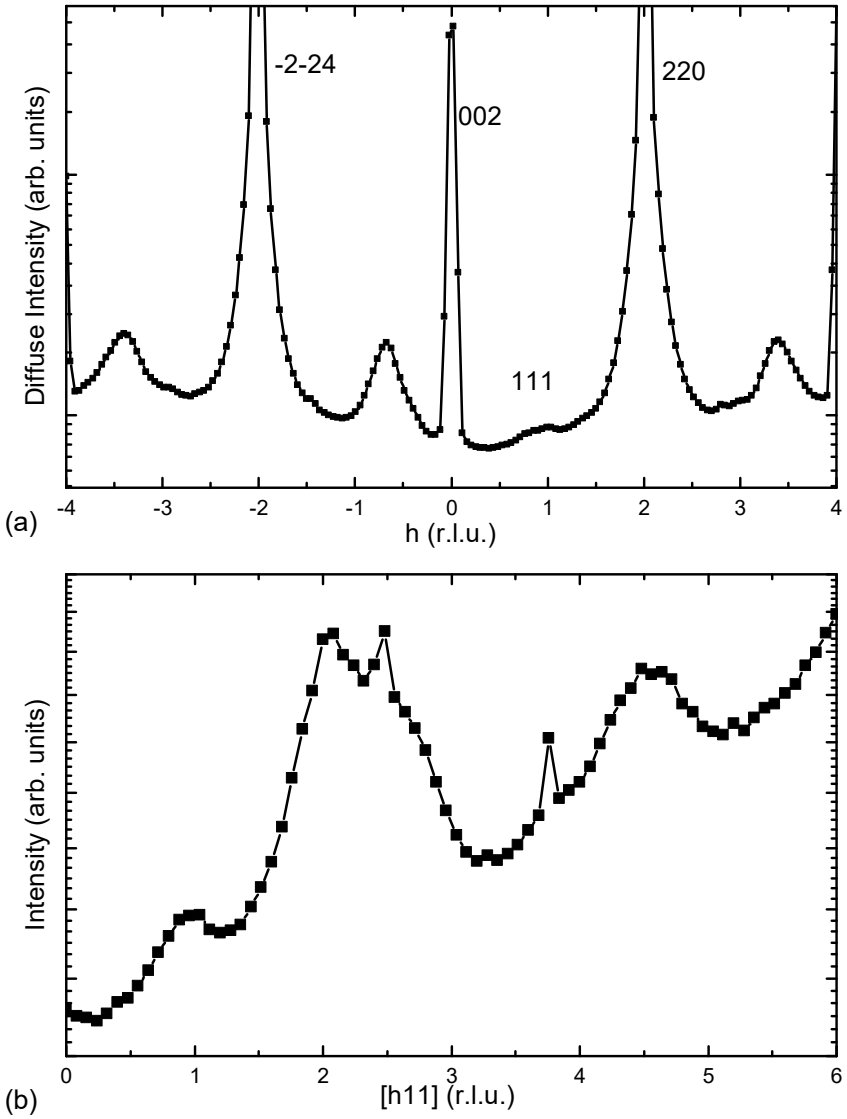

Figure 5.29: (a)q-scan in [11-1] direction through fundamental, B2 superstructure and $L2_1$ superstructure reflections. Note that Bragg intensities are completely omitted here. (b) q-scan in [100] direction at the position k,l=1. Sharp peaks h=2.5 and h=3.7 are due to the weak Debye-Scherrer rings in the data.

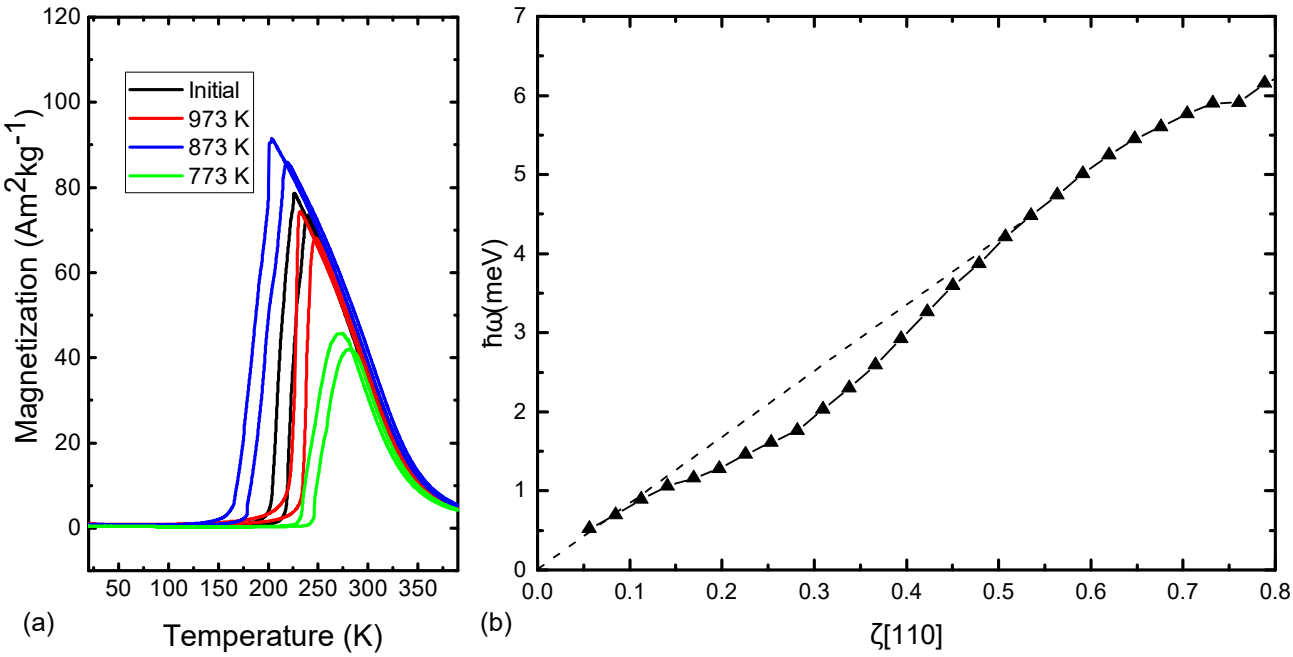

Figure 5.30: (a) Magnetization of $Ni_{37}Co_{13}Mn_{33}Ti_{17}$ without secondary heat treatment and secondary heat treatment between 773 K and 973 K of the same initial grain. (b) Qualitative phonon dispersion constructed out of TDS of the crystal with heat treatment at 773 K.

the background intensities and weaker than the TDS intensities. This means that the signal is more than 6 orders of magnitude weaker than the signal from Bragg reflections, as seen in Figure 5.19. This prevents us from being able to detect this weak SRO signal in polycrystalline data, even if one were able to enhance the SRO signal by one order of magnitude. In powder diffraction, seldom more than 3 orders of magnitude dynamic range can be achieved.

A significant drawback of the low temperature required for the formation of $L2_1$ SRO is that in this temperature region, decomposition can also occur. This makes it difficult to clearly distinguish the effects of $L2_1$ SRO from those related to decomposition. The annealing time was chosen as a compromise in order to minimize decomposition while enabling short range diffuse processes to enhance the degree of SRO. However, it cannot be entirely ruled out that the start of decomposition may occur, even though no signs of decomposition were visible in the diffuse scattering data, which probes the entire volume of the crystal at a length of 300 *mum*. The magnetization of the sample with $L2_1$ SRO is shown in Figure 5.30 (a), with crystals subjected to different secondary heat treatments using the same bulk sample/grain for comparison. While the sample subjected to a heat treatment at 973 K exhibits a phase transition similar to the initial sample without any secondary heat treatment, lowering the annealing temperature to 873 K further reduces the phase transition temperature. This reduction can be

attributed to a slight change in the degree of B2-ordering, as discussed in section 5.1. Due to the substantial differences in thermal mass, with a single crystal weighing around 1 mg, a bulk sample weighing several grams, and a powder sample also weighing several grams, the effect of a given annealing temperature varies during the cooling process. Given the rapid ordering kinetics of Heusler alloys in this temperature range[22], this significantly influences the final degree of order. The higher mass of the initial sample results in a slower cooling rate compared to the single crystals. Consequently, both the initial sample and the crystal subjected to a heat treatment at 973 K exhibit similar phase transition temperatures and B2 LRO parameters. This degree of LRO slightly increases after the heat treatment at 873 K, leading to a lower phase transition temperature, as expected.

In contrast, the heat treatment at 773 K shifts the phase transition temperature back to higher values, possibly indicating the onset of $L2_1$ cluster formation. However, the magnetism only undergoes a slight change, resulting in a lower T_c. This increase in the phase transition temperature with the development of $L2_1$ order aligns with findings in NiCoMnIn single crystals[21]. Additionally, the phase transition becomes broader, potentially linked to the formation of local clusters and thus enhanced chemical variations within the sample. However, it's important to note that decomposition may also contribute to the broadening of the transition, and further investigation is needed to clarify this aspect and to disentangle these possible contributions. Analyzing the TDS data, as shown in Figure 5.24, allows us to approximate a phonon dispersion for the TA_2 branch, as presented in Figure 5.30 (b). To scale the y-axis, the elastic constants determined in section 5.4.3 are utilized as an approximation. It's noteworthy that the anomaly in the phonon dispersion is present even without $L2_1$ SRO, but it becomes more pronounced with the development of $L2_1$ SRO. This observation highlights that the typical Heusler structure plays a crucial role in promoting lattice instability. However, the B2 structure, even without any $L2_1$ SRO, is sufficient to provide the electronic instability that leads to the martensitic phase transition. Furthermore, this finding aligns with the higher phase transition temperature observed in the sample with $L2_1$ SRO.

The effect of the Ni/Co sublattice remains unclear in our study. Since the contrast is substantially weaker for Ni/Co, the data is predominantly dominated by Mn/Ti. This dominance prevents us from clearly observing SRO in the case of a similarly weak ordering tendency as observed for Mn/Ti, as the signals are at the same positions in reciprocal space. Altering the scattering contrast through anomalous diffraction can potentially be employed to analyze short range order between d-metals, such as in high-entropy alloys (HEA) [179]. However, increasing the scattering contrast between Mn and Ti in our case would require measurements at the Ti absorption edge, which is challenging due to the extremely low energy for x-ray diffraction in

this region. Similarly, measurements around the Mn absorption edge could be beneficial since the form factor of Mn varies significantly and may even fall below that of Ti. This variation allows us to adjust the contrast between Mn and Ti slightly, affecting the intensity of Laue scattering originating from random Mn/Ti sites, even allowing tuning the contrast between Mn and Ti to zero.

Changing the scattering contrast through the Co and Ni absorption edges is another possibility. However, experiments for anomalous scattering in general in this energy regime require a completely different setup compared to diffuse scattering performed here. Since transmission in this energy window is not possible, reflection measurements are necessary, with a need to minimize potential background sources, such as by working in a vacuum. Additionally, diffuse neutron scattering could be highly complementary to diffuse x-ray scattering if a larger single crystal becomes available, which was already discussed prior for more detailed analysis of the phonon dispersion. Neutrons provide enhanced contrast between Ni and Co, and the reduced contrast between Mn and Ti compared to x-rays makes it ideal for observing SRO effects between Ni and Co. However, additional care is required when dealing with neutron scattering since it introduces an additional diffuse background related to Laue monotonic scattering between isotopes, known as incoherent scattering. To mitigate this, the use of an isotope-enriched large single crystal would be an ideal choice for studying SRO between all elements.

6 Conclusion

Within this thesis, the interplay between chemical order (on short and long length scales) and the structural instability of the compositionally complex all-d-Heusler alloy Ni(Co)MnTi was investigated. This was done using Bragg scattering on polycrystalline samples to investigate long range chemical order. Diffuse x-ray scattering on self-grown single crystals was used for examining short range order and the elastic precursors of the instability. The structural instability leading to the magneto-structural phase transition, is the driving force for the caloric effects in these compounds. Therefore, the understanding of this instability and their underlying chemical ordering schemes are from fundamental interest for bringing the Ni(Co)MnTi system to its physical limits and also for stimulating further research for compounds which also possess a similar structural instability.

The investigation of the long range structure has revealed that only B2 order, with Ti/Mn on one site and Ni(/Co) on the other site, is present in the Ni(Co)MnTi system. It is demonstrated that long range $L2_1$ order, which is typical for the long-known Ni-Mn-Z Heusler compounds, cannot be stabilized by annealing at temperatures between 573 K and 1173 K in this system. In Ni-Mn-Z Heusler alloys, the formation of a p-d hybrid state between Ni and the main group element is assumed to play a central role in the structural instability leading to the martensitic phase transition [7, 9, 10]. In all-d-metal systems like Ni(Co)MnTi, where Ti-atoms do not provide additional p-electrons, this role must be taken over by d-d hybridization [24, 25]. Given that long range $L2_1$ structures can be stabilized in all other Ni-Mn-Z alloys, the different hybridization in all-d-metal Heusler alloys may additionally affect the ordering scheme, reducing the tendency to form a long range ordered $L2_1$ structure. Nonetheless, the overall electronic behavior of $Ni_{50}Mn_{50-x}Ti_x$ conforms to the expected behavior for Heusler systems. The phase transition temperatures are governed by the ratio of the number of valence electrons per atom. As $\frac{e}{a}$ decreases with increasing Ti content, there is a linear decrease in the phase transition temperature, up to a concentration of 23 at.% Ti.

In Co-containing alloys, it has been demonstrated that they are sensitive to chemical dis-

order, which can lead to a significant shift in the magnetic and martensitic phase transition due to alterations in magnetic interactions and in the energy landscape across the Bain path. This effect has been confirmed through theoretical calculations [149]. The degree of chemical disorder involving Co atoms can serve as an additional method for tuning the phase transition. This phenomenon is observed not only in powder or polycrystalline samples but also in bulk single crystals. However, due to variations in effective cooling rates and thermal masses, the behavior may not be identical and strongly depends on the actual cooling rate.

Furthermore, alloying with Co offers the flexibility to modify not only the magnetism of the austenite phase but also the crystal structure of the martensite phase without significantly altering the phase transition temperature. This can have a substantial impact on the compatibility between the austenite and martensite phases, leading to a significant improvement in thermal hysteresis. In cases where large magnetization is required, this effect has already been utilized, as ferromagnetism necessitates a certain Co content. This induces a phase transition from a less compatible orthorhombic martensite to a monoclinic martensite with enhanced compatibility. However, for the elastocaloric effect, no change in magnetization is required to induce the phase transition. Instead, a magnetization change reduces the total caloric effect. This makes the composition around 10 at.% Co promising for these applications, where no large magnetization change is present, but the crystal structures are already more compatible. Until now, either ferromagnetic alloys or alloys without Co have been investigated for the elastocaloric effect in all-d-Heusler alloys.

The investigation of diffuse scattering in single crystals of $Ni_{37}Co_{13}Mn_{33}Ti_{17}$ using high-energy x-ray diffraction at a synchrotron source can provide detailed insights into the local structures and elastic instabilities present in these complex alloys. Modern detector technology has significantly improved the quality and efficiency of such experiments, allowing for rapid data acquisition and making diffuse scattering a powerful tool for studying phase transitions in compositionally complex materials.

Thermal diffuse scattering has been employed to probe elastic instability in both the long-wave limit (associated with elastic constants) and the short-wave region (related to the TA_2 softening). While a soft mode in the TA_2 phonon branch is observed, a notable difference is observed when compared to literature data on Ni-Mn-Z Heusler alloys, such as Ni-Mn-Ga [73, 74, 173], Ni-Mn-Al [171], or Ni-Mn-In [75]. In this case, the TA_2 soft mode is less pronounced, and it does not significantly change as the phase transition is approached. Furthermore, the investigation of elastic constants reveals an increase in both shear elastic moduli, C_{44} and C', which is contrary to the common observation of a decrease in C' in shape memory alloys. Instead, the phase transition in this system is driven by the interplay between these two moduli. This behavior

is evident in the Zener anisotropy constant, which exhibits a strong increase near the phase transition. This effect can be attributed to the complex interplay between lattice and magnetism interactions, which counteract each other in this material.

An annealing treatment at 973 K does not result in a preferred local ordering between Mn/Ti atoms. However, lowering the annealing temperature to 773 K promotes the formation of locally ordered $L2_1$ clusters with a size of approximately 1.5 nm, which are observable in x-ray diffuse scattering experiments. This observation highlights that the ground state of the all-d-metal Heusler alloy is indeed the $L2_1$ ordered state. Further investigation of enhanced ordering through quenching in vacancies may offer a potential way to improve kinetics and facilitate the formation of larger ordered clusters, as already shown for the Ni-Mn-Al system.[180] The significant difference in intensity between SRO signals and Bragg signals, with the SRO signals being more than 6 orders of magnitude weaker, underscores the importance of using single crystals and synchrotron sources for studying and investigating SRO in all-d-Heusler alloys.

What remains uncertain is the local configuration of atoms on the Ni/Co site, where the potential SRO signal is roughly one order of magnitude weaker than on the Mn/Ti site. Therefore, it is inconclusive whether there is an additional ordering tendency on this site. To explore this further, it would be necessary to conduct either an anomalous scattering experiment or, ideally, employ a larger single crystal for an in-depth investigation of the diffuse neutron scattering pattern. This would notably enhance the contrast on the Ni/Co site while diminishing the contrast on the Mn/Ti site, which was already used for the investigation of LRO in this work.

The presence of $L2_1$ short range order leads to an increase in the phase transition temperature. This effect is distinct from the influence of long range $B2$ ordering, where an increase in the order parameter typically results in a reduction of the phase transition temperature. The enhanced phase transition temperature associated with $L2_1$ order also corresponds to a more pronounced soft mode in the TA_2 phonon branch.

Overall, this work demonstrates that ordering can occur on both long and short length scales in all-d-Heusler alloys, where both order parameters can be influenced by the corresponding heat treatment. These small changes in ordering have a significant impact on the martensitic phase transition and can therefore be utilized for additional alloy tuning of the phase transition. Despite the absence of main group elements in all-d-Heusler alloys, the physics is quite similar to classical Ni-Mn-Z alloys. Both tend to adopt an $L2_1$ ground state, and both exhibit the anomalous softening of the TA_2 phonon branch, confirming that p-electrons are not required for this elastic instability and the $L2_1$ structure. This paves the way for further exploration of materials composed of abundant 3d-metals and for optimizing the Ni(Co)MnTi alloys by adjustment of the chemical order.

Acknowledgements

First and foremost, I would like to express my gratitude to Prof. Wolfgang Donner for his exceptional guidance and mentorship throughout my PhD journey. I am thankful for his unwavering support during synchrotron beam times at ESRF and DESY, as well as for his invaluable advice and the independence he granted me during my research.

I am also deeply grateful to PD Dr. Markus Gruner for his collaboration and for agreeing to be a co-referee for my work. His insights have been instrumental in advancing my research.

I extend my appreciation to Prof. Lambert Alff and Prof. Karsten Durst for kindly agreeing to be part of my examination committee.

During my time at the university, I had the privilege of collaborating with numerous individuals, mostly by providing my expertise in structural characterization. Many of these individuals also significantly aided my research, and I would like to express my thanks to them. I am grateful to Benedikt Beckmann, Dr. Narendirakumar Narayanan, Dr. Olga Miroshkina, Nuno Fortunato, and Franziska Staab for their valuable input and ongoing collaborations. Additionally, I want to thank Dr. Martin von Zimmermann, Dr. Oleh Ivasko, and Dr. Gavin Vaughan for their support during synchrotron beamtimes.

The scientific environment fostered by the CRC/TRR270 has led to exciting collaborations and scientific endeavors. I extend my gratitude to Dr. Lukas Schäfer, Kilian Schäfer, Dr. Franziska Scheibel, Niels Kubitza, Nicholas Josten, Dr. Benedikt Eggert, Johanna Lill, Dr. Ruksan Nadarajan, Shabbir Tahir, and Prof. i.R. Mehmet Acet for their contributions to stimulating scientific work in an excellent work environment.

Furthermore, I appreciate the fruitful collaborations with the members of the Functional Materials group. Special thanks go to Dr. Fernando Maccari, Dr. Semih Ener, Dr. Lukas Pfeuffer, Yevhen Ablets, and Prof. Oliver Gutfleisch as head of the group.

My gratitude extends to the international groups I had the privilege to collaborate with, including Dr. Leopold Diop from the Universite de Lorraine, Dr. Greta Cavazzini from Parma University, and Dr. Joshua Levinsky from Groningen University. These interactions have enriched my scientific journey.

I wish to acknowledge the valuable contributions of Cornelia Hoppe, Yannic Stahl, and Jonas Philippi during their Bachelor Theses and as a HiWi, respectively. The smooth operation of the laboratory owes much to the continuous support from the workshop personal, for which I am thankful.

I would also like to express my appreciation to the Structure Research group and its members for their support and the wonderful times we shared. Special thanks go to Jean-Christophe Jaud, Leif Carstensen, Claudia Fasel, Heinz Mohren, Dr. Joachim Brötz, Dr. Constantin Wansorra, Dr. Tom Faske, Marcel Urban, Sabine Foro, and Maria Bense.

Lastly, my thanks go to my family and to Amelie for their unwavering support throughout my academic journey.

Publications

[1] R. Nadarajah, S. Tahir, J. Landers, D. Koch, A. S. Semisalova, J. Wiemeler, A. El-Zoka, S.-H. Kim, D. Utzat, R. Möller, B. Gault, H. Wende, M. Farle, and B. Gökce. "Controlling the oxidation of magnetic and electrically conductive solid-solution iron-rhodium nanoparticles synthesized by laser ablation in liquids." In: Nanomaterials 10.12 (2020), p. 2362.

[2] G. Cavazzini, F. Cugini, D. Delmonte, G. Trevisi, L. Nasi, S. Ener, D. Koch, L. Righi, M. Solzi, O. Gutfleisch, and F. Albertini. "Multifunctional Ni-Mn-Ga and Ni-Mn-Cu-Ga Heusler particles towards the nanoscale by ball-milling technique." In: Journal of Alloys and Compounds 872 (2021), p. 159747.

[3] L. Diop, T. Faske, M. Amara, D. Koch, O. Isnard, and W. Donner. "Evidence for a coupled magnetic-crystallographic transition in La 0.9 Ce 0.1 Fe 12 B 6." In: Physical Review B 104.13 (2021), p. 134412.

[4] F. Maccari, S. Ener, D. Koch, I. Dirba, K. Skokov, E. Bruder, L. Schäfer, and O. Gutfleisch. "Correlating changes of the unit cell parameters and microstructure with magnetic properties in the CeFe11Ti compound." In: Journal of Alloys and Compounds 867 (2021), p. 158805.

[5] L. Pfeuffer, J. Lemke, N. Shayanfar, S. Riegg, D. Koch, A. Taubel, F. Scheibel, N. A. Kani, E. Adabifiroozjaei, L. Molina-Luna, K. P. Skokov, and O. Gutfleisch. "Microstructure engineering of metamagnetic Ni-Mn-based Heusler compounds by Fe-doping: A roadmap towards excellent cyclic stability combined with large elastocaloric and magnetocaloric effects." In: Acta Materialia 221 (2021), p. 117390.

[6] L. Pfeuffer, A. Gràcia-Condal, T. Gottschall, D. Koch, T. Faske, E. Bruder, J. Lemke, A. Taubel, S. Ener, F. Scheibel, K. Durst, K. P. Skokov, L. Mañosa, A. Planes, and O. Gutfleisch. "Influence of microstructure on the application of Ni-Mn-In Heusler compounds for multicaloric cooling using magnetic field and uniaxial stress." In: Acta Materialia 217 (2021), p. 117157.

[7] R. Nadarajah, J. Landers, S. Salamon, D. Koch, S. Tahir, C. Doñate-Buendía, B. Zingsem, R. E. Dunin-Borkowski, W. Donner, M. Farle, H. Wende, and B. Gökce. "Towards laser printing of magnetocaloric structures by inducing a magnetic phase transition in iron-rhodium nanoparticles." In: Scientific Reports 11.1 (2021), p. 13719.

[8] D. Koch, B. Beckmann, N. M. Fortunato, O. N. Miroshkina, M. E. Gruner, H. Zhang, O. Gutfleisch, and W. Donner. "Chemical long range ordering in all-d-metal Heusler alloys." In: Journal of Applied Physics 131.7 (2022).

[9] Ö. Özgün, D. Koch, A. Çakr, T. Tavanolu, W. Donner, M. Farle, and M. Acet. "Magnetic properties of fcc and σ phases in equiatomic and off-equiatomic high-entropy Cantor alloys." In: Physical Review B 106.21 (2022), p. 214422.

[10] G. Cavazzini, F. Cugini, F. Puglielli, S. Fabbrici, D. Delmonte, G. Trevisi, L. Nasi, L. Righi, S. Ener, L. Pfeuffer, D. Koch, O. Gutfleisch, F. Albertini, and M. Solzi. "Effect of size and disorder on martensitic phase transition and thermal hysteresis in milled Ni-Mn-In-Co microparticles." In: Journal of Alloys and Compounds 906 (2022), p. 164377.

[11] O. N. Miroshkina, B. Eggert, J. Lill, B. Beckmann, D. Koch, M. Y. Hu, T. Lojewski, S. Rauls, F. Scheibel, A. Taubel, M. ob, K. Ollefs, O. Gutfleisch, H. Wende, M. E. Gruner, and M. Friák. "Impact of magnetic and antisite disorder on the vibrational densities of states in Ni 2 MnSn Heusler alloys." In: Physical Review B 106.21 (2022), p. 214302.

[12] F. Staab, E. Bruder, L. Schäfer, K. Skokov, D. Koch, B. Zingsem, E. Adabifiroozjaei, L. Molina-Luna, O. Gutfleisch, and K. Durst. "Hard magnetic SmCo5-Cu nanocomposites produced by severe plastic deformation." In: Acta Materialia 246 (2023), p. 118709.

[13] B. Beckmann, D. Koch, L. Pfeuffer, T. Gottschall, A. Taubel, E. Adabifiroozjaei, O. N. Miroshkina, S. Riegg, T. Niehoff, N. A. Kani, M. E. Gruner, L. Molina-Luna, K. P. Skokov, and O. Gutfleisch. "Dissipation losses limiting first-order phase transition materials in cryogenic caloric cooling: A case study on all-d-metal Ni (-Co)-Mn-Ti Heusler alloys." In: Acta Materialia 246 (2023), p. 118695.

[14] L. Schäfer, K. Skokov, F. Maccari, I. Radulov, D. Koch, A. Mazilkin, E. Adabifiroozjaei, L. Molina-Luna, and O. Gutfleisch. "A Novel Magnetic Hardening Mechanism for Nd-Fe-B Permanent Magnets Based on Solid-State Phase Transformation." In: Advanced Functional Materials 33.4 (2023), p. 2208821.

[15] B. Beckmann, T. A. El-Melegy, D. Koch, U. Wiedwald, M. Farle, F. Maccari, J. Snyder, K. P. Skokov, M. W. Barsoum, and O. Gutfleisch. "Reactive single-step hot-pressing and magnetocaloric performance of polycrystalline Fe2Al1. 15- xB2GexGax (x= 0, 0.05) MAB phases." In: Journal of applied physics 133.17 (2023).

[16] F. Scheibel, C. Lauhoff, P. Krooss, S. Riegg, N. Sommer, D. Koch, K. Opelt, H. Gutte, O. Volkova, S. Böhm, T. Niendorf, and O. Gutfleisch. “Additive manufacturing of Ni-Mn-Sn shape memory Heusler alloy–Microstructure and magnetic properties from powder to printed parts.” In: Materialia 29 (2023), p. 101783.

[17] S. Tahir, J. Landers, S. Salamon, D. Koch, C. Doñate-Buendía, A. R. Ziefuss, H. Wende, and B. Gökce. “Development of Magnetocaloric Microstructures from Equiatomic IronRhodium Nanoparticles through Laser Sintering.” In: Advanced Engineering Materials n/a.n/a (), p. 2300245.

[18] K. Schäfer, R. Fim, F. Maccari, T. Braun, S. Riegg, K. Skokov, D. Koch, E. Bruder, I. Radulov, C. Ahrens, P. Wendhausen, and O. Gutfleisch. “Laser powder bed fusion of anisotropic Nd-Fe-B bonded magnets utilizing an in-situ mechanical alignment approach.” In: Journal of Magnetism and Magnetic Materials 583 (2023), p. 171064. ISSN: 0304-8853.

[19] F. Staab, Y. Yang, E. Foya, E. Bruder, B. Zingsem, E. Adabifiroozjaei, D. Nasiou, K. Skokov, D. Koch, M. Farle, R. E. Dunin-Borkowski, L. Molina-Luna, O. Gutfleisch, B.-X. Xu, and K. Durst. “Influence of amorphous phase on coercivity in SmCo5-Cu nanocomposites.” In: Scripta Materialia (2023). (in press).

Conference Contributions

[1] D. Koch, B. Beckmann, O. N. Mirsohkina, N. M. Fortunato, M. E. Gruner, H. Zhang, O. Gutfleisch, and W. Donner. “Poster: Chemical long range ordering in all-d-metal Heusler alloys.” In: DPG SKM Frühjahrstagung. 2022.

[2] D. Koch, B. Beckmann, G. V. B. Vaughan, O. Gutfleisch, and W. Donner. “Poster: Growth and characterization of Ni37Co13Mn33Ti17 single crystals.” In: DPG SKM Frühjahrstagung. 2023.

[3] D. Koch, G. V. B. Vaughan, and W. Donner. “Talk: Diffuse Scattering in NiCoMnTi all-d-Heusler single crystals.” In: Seventh International Conference on Ferromagnetic Shape Memory Alloys. 2023.

List of Figures

List of Tables

References

[1] V. Franco, J. Blázquez, J. Ipus, J. Law, L. Moreno-Ramírez, and A. Conde. "Magnetocaloric effect: From materials research to refrigeration devices." In: Progress in Materials Science 93 (2018), pp. 112–232. ISSN: 0079-6425.

[2] IEA. "The Future of Cooling." In: https://www.iea.org/reports/the-future-of-cooling (2018).

[3] A. Zheludev, S. Shapiro, P. Wochner, A. Schwartz, M. Wall, and L. Tanner. "Phonon anomaly, central peak, and microstructures in Ni 2 MnGa." In: Physical Review B 51.17 (1995), p. 11310.

[4] A. Zheludev, S. Shapiro, P. Wochner, and L. Tanner. "Precursor effects and premartensitic transformation in Ni 2 MnGa." In: Physical Review B 54.21 (1996), p. 15045.

[5] R. Kainuma, F. Gejima, Y. Sutou, I. Ohnuma, and K. Ishida. "Ordering, martensitic and ferromagnetic transformations in Ni-Al-Mn Heusler shape memory alloys." In: Materials transactions, JIM 41.8 (2000), pp. 943–949.

[6] M. Acet, E. Duman, E. F. Wassermann, L. Mañosa, and A. Planes. "Coexisting ferro- and antiferromagnetism in Ni2MnAl Heusler alloys." In: Journal of Applied Physics 92.7 (2002), pp. 3867–3871. ISSN: 0021-8979.

[7] A. Zayak and P. Entel. "Role of shuffles and atomic disorder in NiMnGa." In: Materials Science and Engineering: A 378.1 (2004). European Symposium on Martensitic Transformation and Shape-Memory, pp. 419–423. ISSN: 0921-5093.

[8] T. Krenke, E. Duman, M. Acet, E. F. Wassermann, X. Moya, L. Mañosa, and A. Planes. "Inverse magnetocaloric effect in ferromagnetic Ni–Mn–Sn alloys." In: Nature Materials 4.6 (2005), pp. 450–454.

[9] A. T. Zayak, P. Entel, K. M. Rabe, W. A. Adeagbo, and M. Acet. "Anomalous vibrational effects in nonmagnetic and magnetic Heusler alloys." In: Phys. Rev. B 72 (5 2005), p. 054113.

[10] P. Entel, V. Buchelnikov, V. Khovailo, A. Zayak, W. Adeagbo, M. Gruner, H. Herper, and E. Wassermann. "Modelling the phase diagram of magnetic shape memory Heusler alloys." In: Journal of Physics D: Applied Physics 39.5 (2006), p. 865.

[11] T. Krenke, X. Moya, S. Aksoy, M. Acet, P. Entel, L. Mañosa, A. Planes, Y. Elerman, A. Yücel, and E. Wassermann. "Electronic aspects of the martensitic transition in NiMn based Heusler alloys." In: Journal of Magnetism and Magnetic Materials 310.2, Part 3 (2007). Proceedings of the 17th International Conference on Magnetism, pp. 2788–2789. ISSN: 0304-8853.

[12] M. Khan, A. K. Pathak, M. R. Paudel, I. Dubenko, S. Stadler, and N. Ali. "Magnetoresistance and field-induced structural transitions in Ni50Mn50- xSnx Heusler alloys." In: Journal of magnetism and magnetic materials 320.3-4 (2008), pp. L21–L25.

[13] T. Mehaddene, J. Neuhaus, W. Petry, K. Hradil, P. Bourges, and A. Hiess. "Interplay of structural instability and lattice dynamics in Ni 2 MnAl." In: Physical Review B 78.10 (2008), p. 104110.

[14] A. Planes, L. Mañosa, and M. Acet. "Magnetocaloric effect and its relation to shape-memory properties in ferromagnetic Heusler alloys." In: Journal of Physics: Condensed Matter 21.23 (2009), p. 233201.

[15] V. Buchelnikov and V. Sokolovskiy. "Magnetocaloric effect in Ni-Mn-X (X= Ga, In, Sn, Sb) Heusler alloys." In: The Physics of Metals and Metallography 112.7 (2011), pp. 633–665.

[16] A. Çakır, L. Righi, F. Albertini, M. Acet, M. Farle, and S. Aktürk. "Extended investigation of intermartensitic transitions in Ni-Mn-Ga magnetic shape memory alloys: A detailed phase diagram determination." In: Journal of Applied Physics 114.18 (2013).

[17] T. Kihara, X. Xu, W. Ito, R. Kainuma, and M. Tokunaga. "Direct measurements of inverse magnetocaloric effects in metamagnetic shape-memory alloy NiCoMnIn." In: Phys. Rev. B 90 (21 2014), p. 214409.

[18] F. Xiao, M. Jin, J. Liu, and X. Jin. "Elastocaloric effect in Ni50Fe19Ga27Co4 single crystals." In: Acta Materialia 96 (2015), pp. 292–300.

[19] T. Gottschall, K. P. Skokov, D. Benke, M. E. Gruner, and O. Gutfleisch. "Contradictory role of the magnetic contribution in inverse magnetocaloric Heusler materials." In: Physical Review B 93.18 (2016), p. 184431.

[20] P. Neibecker, M. E. Gruner, X. Xu, R. Kainuma, W. Petry, R. Pentcheva, and M. Leitner. "Ordering tendencies and electronic properties in quaternary Heusler derivatives." In: Physical Review B 96.16 (2017), p. 165131.

[21] N. Bruno, D. Salas, S. Wang, I. V. Roshchin, R. Santamarta, R. Arroyave, T. Duong, Y. Chumlyakov, and I. Karaman. "On the microstructural origins of martensitic transformation arrest in a NiCoMnIn magnetic shape memory alloy." In: Acta Materialia 142 (2018), pp. 95–106. ISSN: 1359-6454.

[22] Y. Wang, D. Salas, T. C. Duong, B. Medasani, A. Talapatra, Y. Ren, Y. I. Chumlyakov, I. Karaman, and R. Arróyave. "On the fast kinetics of B2L21 ordering in Ni-Co-Mn-In metamagnetic shape memory alloys." In: Journal of Alloys and Compounds 781 (2019), pp. 479–489. ISSN: 0925-8388.

[23] L. Pfeuffer, J. Lemke, N. Shayanfar, S. Riegg, D. Koch, A. Taubel, F. Scheibel, N. A. Kani, E. Adabifiroozjaei, L. Molina-Luna, K. P. Skokov, and O. Gutfleisch. "Microstructure engineering of metamagnetic Ni-Mn-based Heusler compounds by Fe-doping: A roadmap towards excellent cyclic stability combined with large elastocaloric and magnetocaloric effects." In: Acta Materialia 221 (2021), p. 117390. ISSN: 1359-6454.

[24] Z. Y. Wei, E. K. Liu, J. H. Chen, Y. Li, G. D. Liu, H. Z. Luo, X. K. Xi, H. W. Zhang, W. H. Wang, and G. H. Wu. "Realization of multifunctional shape-memory ferromagnets in all-d-metal Heusler phases." In: Applied Physics Letters 107.2 (2015), p. 022406.

[25] Z. Y. Wei, E. K. Liu, Y. Li, X. L. Han, Z. W. Du, H. Z. Luo, G. D. Liu, X. K. Xi, H. W. Zhang, W. H. Wang, and G. H. Wu. "Magnetostructural martensitic transformations with large volume changes and magneto-strains in all-d-metal Heusler alloys." In: Applied Physics Letters 109.7 (2016), p. 071904.

[26] Z. Y. Wei, W. Sun, Q. Shen, Y. Shen, Y. F. Zhang, E. K. Liu, and J. Liu. "Elastocaloric effect of all-d-metal Heusler NiMnTi(Co) magnetic shape memory alloys by digital image correlation and infrared thermography." In: Applied Physics Letters 114.10 (2019), p. 101903.

[27] A. Taubel, B. Beckmann, L. Pfeuffer, N. Fortunato, F. Scheibel, S. Ener, T. Gottschall, K. P. Skokov, H. Zhang, and O. Gutfleisch. "Tailoring magnetocaloric effect in all-d-metal Ni-Co-Mn-Ti Heusler alloys: a combined experimental and theoretical study." In: Acta Materialia 201 (2020), pp. 425–434. ISSN: 1359-6454.

[28] H. Neves Bez, A. K. Pathak, A. Biswas, N. Zarkevich, V. Balema, Y. Mudryk, D. D. Johnson, and V. K. Pecharsky. "Giant enhancement of the magnetocaloric response in NiCoMnTi by rapid solidification." In: Acta Materialia 173 (2019), pp. 225–230. ISSN: 1359-6454.

[29] D. Cong, W. Xiong, A. Planes, Y. Ren, L. Mañosa, P. Cao, Z. Nie, X. Sun, Z. Yang, X. Hong, and Y. Wang. "Colossal Elastocaloric Effect in Ferroelastic Ni-Mn-Ti Alloys." In: Phys. Rev. Lett. 122 (25 2019), p. 255703.

[30] A. Aznar, A. Gràcia-Condal, A. Planes, P. Lloveras, M. Barrio, J.-L. Tamarit, W. Xiong, D. Cong, C. Popescu, and L. Mañosa. "Giant barocaloric effect in all-*d*-metal Heusler shape memory alloys." In: Phys. Rev. Materials 3 (4 2019), p. 044406.

[31] H.-L. Yan, L.-D. Wang, H.-X. Liu, X.-M. Huang, N. Jia, Z.-B. Li, B. Yang, Y.-D. Zhang, C. Esling, X. Zhao, and L. Zuo. "Giant elastocaloric effect and exceptional mechanical properties in an all-d-metal NiMnTi alloy: Experimental and ab-initio studies." In: Materials & Design 184 (2019), p. 108180. ISSN: 0264-1275.

[32] Y. Shen, Z. Wei, W. Sun, Y. Zhang, E. Liu, and J. Liu. "Large elastocaloric effect in directionally solidified all-d-metal Heusler metamagnetic shape memory alloys." In: Acta Materialia 188 (2020), pp. 677–685. ISSN: 1359-6454.

[33] Z. Guan, J. Bai, S. Sun, J. Gu, X. Liang, Y. Zhang, C. Esling, X. Zhao, and L. Zuo. "Extraordinary mechanical properties and successive caloric effects with ultrahigh cyclic stability in directionally solidified Ni36.6Co12.8Mn34.7Ti15.9 alloy." In: Applied Materials Today 29 (2022), p. 101634. ISSN: 2352-9407.

[34] Z. Guan, J. Bai, J. Gu, X. Liang, D. Liu, X. Jiang, R. Huang, Y. Zhang, C. Esling, X. Zhao, et al. "First-principles investigation of B2 partial disordered structure, martensitic transformation, elastic and magnetic properties of all-d-metal Ni-Mn-Ti Heusler alloys." In: Journal of Materials Science & Technology 68 (2021), pp. 103–111.

[35] V. G. de Paula and M. S. Reis. "All-d-metal full Heusler alloys: A novel class of functional materials." In: Chemistry of Materials 33.14 (2021), pp. 5483–5495.

[36] F. Zhang, K. Westra, Q. Shen, I. Batashev, A. Kiecana, N. van Dijk, and E. Brück. "The second-order magnetic phase transition and magnetocaloric effect in all-d-metal NiCoMnTi-based Heusler alloys." In: Journal of Alloys and Compounds 906 (2022), p. 164337.

[37] Z. Wei, Y. Shen, Z. Zhang, J. Guo, B. Li, E. Liu, Z. Zhang, and J. Liu. "Low-pressure-induced giant barocaloric effect in an all-d-metal Heusler Ni35.5Co14.5Mn35Ti15 magnetic shape memory alloy." In: APL Materials 8.5 (2020), p. 051101.

[38] F. Zhang, I. Batashev, N. Van Dijk, and E. Brück. "Reduced hysteresis and enhanced giant magnetocaloric effect in B-Doped all-d-metal Ni-Co-Mn-Ti-based Heusler materials." In: Physical Review Applied 17.5 (2022), p. 054032.

[39] B. Cantor, I. Chang, P. Knight, and A. Vincent. "Microstructural development in equiatomic multicomponent alloys." In: Materials Science and Engineering: A 375-377 (2004), pp. 213–218. ISSN: 0921-5093.

[40] J.-W. Yeh, S.-K. Chen, S.-J. Lin, J.-Y. Gan, T.-S. Chin, T.-T. Shun, C.-H. Tsau, and S.-Y. Chang. "Nanostructured high-entropy alloys with multiple principal elements: novel alloy design concepts and outcomes." In: Advanced engineering materials 6.5 (2004), pp. 299–303.

[41] M.-H. Tsai and J.-W. Yeh. "High-entropy alloys: a critical review." In: Materials Research Letters 2.3 (2014), pp. 107–123.

[42] Y. Wu, F. Zhang, X. Yuan, H. Huang, X. Wen, Y. Wang, M. Zhang, H. Wu, X. Liu, H. Wang, et al. "Short-range ordering and its effects on mechanical properties of high-entropy alloys." In: Journal of Materials Science & Technology 62 (2021), pp. 214–220.

[43] J. Y. Law, L. M. Moreno-Ramírez, Á. Díaz-García, A. Martín-Cid, S. Kobayashi, S. Kawaguchi, T. Nakamura, and V. Franco. "MnFeNiGeSi high-entropy alloy with large magnetocaloric effect." In: Journal of Alloys and Compounds 855 (2021), p. 157424.

[44] J. Y. Law, Á. Díaz-García, L. M. Moreno-Ramírez, and V. Franco. "Increased magnetocaloric response of FeMnNiGeSi high-entropy alloys." In: Acta Materialia 212 (2021), p. 116931.

[45] Y. Guo, T. Zhang, Z. Zhang, B. Chen, W. Guo, S. Pan, Y. Gong, Y. Bai, Y. Gong, J. Liu, X. Miao, and F. Xu. "Large reversible magnetocaloric effect in high-entropy MnFeCoNiGeSi system with low-hysteresis magnetostructural transformation." In: APL Materials 10.9 (2022), p. 091107. ISSN: 2166-532X.

[46] W. Giauque and D. MacDougall. "The production of temperatures below one degree absolute by adiabatic demagnetization of gadolinium sulfate." In: Journal of the American Chemical Society 57.7 (1935), pp. 1175–1185.

[47] G. V. Brown. "Magnetic heat pumping near room temperature." In: Journal of Applied Physics 47.8 (1976), pp. 3673–3680. ISSN: 0021-8979.

[48] V. K. Pecharsky and K. A. Gschneidner Jr. “Giant Magnetocaloric Effect in $Gd_5(Si_2Ge_2)$.” In: Phys. Rev. Lett. 78 (23 1997), pp. 4494–4497.

[49] V. Pecharsky and K. Gschneidner. “Effect of alloying on the giant magnetocaloric effect of Gd5(Si2Ge2).” In: Journal of Magnetism and Magnetic Materials 167.3 (1997), pp. L179–L184. ISSN: 0304-8853.

[50] A. O. Pecharsky, J. Gschneidner K. A., and V. K. Pecharsky. “The giant magnetocaloric effect of optimally prepared Gd5Si2Ge2.” In: Journal of Applied Physics 93.8 (2003), pp. 4722–4728. ISSN: 0021-8979.

[51] K. A. Gschneidner, V. K. Pecharsky, and A. O. Tsokol. “Recent developments in magnetocaloric materials.” In: Reports on Progress in Physics 68.6 (2005), p. 1479.

[52] S. Fähler and V. K. Pecharsky. “Caloric effects in ferroic materials.” In: MRS Bulletin 43.4 (2018), pp. 264–268.

[53] T. Gottschall, K. P. Skokov, M. Fries, A. Taubel, I. Radulov, F. Scheibel, D. Benke, S. Riegg, and O. Gutfleisch. “Making a Cool Choice: The Materials Library of Magnetic Refrigeration.” In: Advanced Energy Materials 9.34 (2019), p. 1901322.

[54] O. Gutfleisch, T. Gottschall, M. Fries, D. Benke, I. Radulov, K. P. Skokov, H. Wende, M. Gruner, M. Acet, P. Entel, and M. Farle. “Mastering hysteresis in magnetocaloric materials.” In: Philosophical Transactions of the Royal Society A: Mathematical, Physical and Engineering Sciences 374.2074 (2016), p. 20150308.

[55] S. Fujieda, A. Fujita, and K. Fukamichi. “Large magnetocaloric effect in La(FexSi1x)13 itinerant-electron metamagnetic compounds.” In: Applied Physics Letters 81.7 (2002), pp. 1276–1278. ISSN: 0003-6951.

[56] A. Fujita, S. Fujieda, Y. Hasegawa, and K. Fukamichi. “Itinerant-electron metamagnetic transition and large magnetocaloric effects in $La(Fe_xSi_{1-x})_{13}$ compounds and their hydrides.” In: Phys. Rev. B 67 (10 2003), p. 104416.

[57] J. Liu, J. Moore, K. Skokov, M. Krautz, K. Löwe, A. Barcza, M. Katter, and O. Gutfleisch. “Exploring La(Fe,Si)13-based magnetic refrigerants towards application.” In: Scripta Materialia 67.6 (2012). Viewpoint Set No. 51: Magnetic Materials for Energy, pp. 584–589. ISSN: 1359-6462.

[58] K. Engelbrecht, C. Bahl, and K. Nielsen. “Experimental results for a magnetic refrigerator using three different types of magnetocaloric material regenerators.” In: International Journal of Refrigeration 34.4 (2011), pp. 1132–1140. ISSN: 0140-7007.

[59] O. Tegus, E. Brück, K. Buschow, and F. De Boer. “Transition-metal-based magnetic refrigerants for room-temperature applications.” In: Nature 415.6868 (2002), pp. 150–152.

[60] D. T. Cam Thanh, E. Brück, N. T. Trung, J. C. P. Klaasse, K. H. J. Buschow, Z. Q. Ou, O. Tegus, and L. Caron. “Structure, magnetism, and magnetocaloric properties of MnFeP1xSix compounds.” In: Journal of Applied Physics 103.7 (2008). 07B318. ISSN: 0021-8979.

[61] F. Guillou, G. Porcari, H. Yibole, N. van Dijk, and E. Brück. “Taming the First-Order Transition in Giant Magnetocaloric Materials.” In: Advanced Materials 26.17 (2014), pp. 2671–2675.

[62] F. Guillou, H. Yibole, N. van Dijk, L. Zhang, V. Hardy, and E. Brück. “About the mechanical stability of MnFe(P,Si,B) giant-magnetocaloric materials.” In: Journal of Alloys and Compounds 617 (2014), pp. 569–574. ISSN: 0925-8388.

[63] F. Heusler. “Ueber magnetische Manganlegierungen.” In: Verh DPG, 5 (1903).

[64] O. Heusler. “Kristallstruktur und Ferromagnetismus der Mangan-Aluminium-Kupferlegierungen.” In: Annalen der Physik 411.2 (1934), pp. 155–201.

[65] T. Graf, C. Felser, and S. S. Parkin. “Simple rules for the understanding of Heusler compounds.” In: Progress in solid state chemistry 39.1 (2011), pp. 1–50.

[66] J. Liu, T. Gottschall, K. P. Skokov, J. D. Moore, and O. Gutfleisch. “Giant magnetocaloric effect driven by structural transitions.” In: Nature Materials 11.7 (2012), pp. 620–626.

[67] L. Mañosa, D. González-Alonso, A. Planes, E. Bonnot, M. Barrio, J.-L. Tamarit, S. Aksoy, and M. Acet. “Giant solid-state barocaloric effect in the Ni–Mn–In magnetic shape-memory alloy.” In: Nature Materials 9.6 (2010), pp. 478–481.

[68] T. Gottschall, A. Gracia-Condal, M. Fries, A. Taubel, L. Pfeuffer, L. Manosa, A. Planes, K. P. Skokov, and O. Gutfleisch. “A multicaloric cooling cycle that exploits thermal hysteresis.” In: Nature Materials 17.10 (2018), pp. 929–934.

[69] L. Pfeuffer, A. Gràcia-Condal, T. Gottschall, D. Koch, T. Faske, E. Bruder, J. Lemke, A. Taubel, S. Ener, F. Scheibel, K. Durst, K. P. Skokov, L. Mañosa, A. Planes, and O. Gutfleisch. “Influence of microstructure on the application of Ni-Mn-In Heusler compounds for multicaloric cooling using magnetic field and uniaxial stress.” In: Acta Materialia 217 (2021), p. 117157. ISSN: 1359-6454.

[70] R. Kainuma, Y. Imano, W. Ito, Y. Sutou, H. Morito, S. Okamoto, O. Kitakami, K. Oikawa, A. Fujita, T. Kanomata, et al. “Magnetic-field-induced shape recovery by reverse phase transformation.” In: Nature 439.7079 (2006), pp. 957–960.

[71] W. Hume-Rothery. “Research on the Nature, Properties and Conditions of Formation of Intermetallic Compounds, with Special Reference to Certain Compounds of Tin.” In: Journal Institute of Metals, Vol. 35, pp.295-299 (1926).

[72] M. C. Gao, J.-W. Yeh, P. K. Liaw, and Y. Zhang. High-entropy alloys: fundamentals and applications. Springer, 2016.

[73] U. Stuhr, P. Vorderwisch, V. V. Kokorin, and P.-A. Lindgård. “Premartensitic phenomena in the ferro- and paramagnetic phases of Ni_2MnGa.” In: Phys. Rev. B 56 (22 1997), pp. 14360–14365.

[74] L. Mañosa, A. Gonz‘alez-Comas, E. Obradó, A. Planes, V. A. Chernenko, V. V. Kokorin, and E. Cesari. “Anomalies related to the TA_2-phonon-mode condensation in the Heusler Ni_2MnGa alloy.” In: Phys. Rev. B 55 (17 1997), pp. 11068–11071.

[75] X. Moya, D. González-Alonso, L. Mañosa, A. Planes, V. O. Garlea, T. A. Lograsso, D. L. Schlagel, J. L. Zarestky, S. Aksoy, and M. Acet. “Lattice dynamics in magnetic superelastic Ni-Mn-In alloys: Neutron scattering and ultrasonic experiments.” In: Phys. Rev. B 79 (21 2009), p. 214118.

[76] G. Wang, Y.-D. Wang, Y. Ren, Y. Liu, and P. K. Liaw. “In-Situ High-Energy X-Ray Diffuse-Scattering Study of the Phase Transition in a Ni 2 MnGa Ferromagnetic Shape-Memory Crystal.” In: Metallurgical and Materials Transactions A 39 (2008), pp. 3184–3190.

[77] T.-L. Cheng, F. D. Ma, J. E. Zhou, G. Jennings, Y. Ren, Y. M. Jin, and Y. U. Wang. “In Situ Three-Dimensional Reciprocal-Space Mapping of Diffuse Scattering Intensity Distribution and Data Analysis for Precursor Phenomenon in Shape-Memory Alloy.” In: JOM 64.1 (2012), pp. 167–173.

[78] A. Planes and L. Mañosa. “Vibrational properties of shape-memory alloys.” In: ed. by H. Ehrenreich and F. Spaepen. Vol. 55. Solid State Physics. Academic Press, 2001, pp. 159–267.

[79] C. Zener. “Contributions to the theory of beta-phase alloys.” In: Physical Review 71.12 (1947), p. 846.

[80] M. Stipcich, L. Mañosa, A. Planes, M. Morin, J. Zarestky, T. Lograsso, and C. Stassis. “Elastic constants of $Ni-Mn-Ga$ magnetic shape memory alloys.” In: Phys. Rev. B 70 (5 2004), p. 054115.

[81] S. Hunklinger. Festkörperphysik. 4. aktual. Aufl. 2014.

[82] S. M. Shapiro, G. Xu, G. Gu, J. Gardner, and R. W. Fonda. “Lattice dynamics of the high-temperature shape-memory alloy Nb−Ru.” In: Phys. Rev. B 73 (21 2006), p. 214114.

[83] E. Simon, J. G. Vida, S. Khmelevskyi, and L. Szunyogh. “Magnetism of ordered and disordered Ni_2MnAl full Heusler compounds.” In: Phys. Rev. B 92 (5 2015), p. 054438.

[84] S. V. Faleev, Y. Ferrante, J. Jeong, M. G. Samant, B. Jones, and S. S. Parkin. “Origin of the tetragonal ground state of Heusler compounds.” In: Physical Review Applied 7.3 (2017), p. 034022.

[85] R. Niemann, U. K. RöSSler, M. E. Gruner, O. Heczko, L. Schultz, and S. Fähler. “The Role of Adaptive Martensite in Magnetic Shape Memory Alloys.” In: Advanced Engineering Materials 14.8 (2012), pp. 562–581.

[86] M. E. Gruner, R. Niemann, P. Entel, R. Pentcheva, U. K. Rössler, K. Nielsch, and S. Fähler. “Modulations in martensitic Heusler alloys originate from nanotwin ordering.” In: Scientific reports 8.1 (2018), p. 8489.

[87] S. Schwabe, R. Niemann, A. Backen, D. Wolf, C. Damm, T. Walter, H. Seiner, O. Heczko, K. Nielsch, and S. Fähler. “Building Hierarchical Martensite.” In: Advanced Functional Materials 31.7 (2021), p. 2005715.

[88] S. van Smaalen. “An elementary introduction to superspace crystallography.” In: Zeitschrift für Kristallographie-Crystalline Materials 219.11 (2004), pp. 681–691.

[89] S. van Smaalen. Incommensurate Crystallography. Oxford University Press, 2007. ISBN: 9780198570820.

[90] V. Petíek, M. Duek, and L. Palatinus. “Crystallographic Computing System JANA2006: General features.” In: Zeitschrift für Kristallographie - Crystalline Materials 229.5 (2014), pp. 345–352.

[91] L. Righi, F. Albertini, L. Pareti, A. Paoluzi, and G. Calestani. “Commensurate and incommensurate 5M modulated crystal structures in NiMnGa martensitic phases.” In: Acta Materialia 55.15 (2007), pp. 5237–5245. ISSN: 1359-6454.

[92] L. Righi, F. Albertini, E. Villa, A. Paoluzi, G. Calestani, V. Chernenko, S. Besseghini, C. Ritter, and F. Passaretti. “Crystal structure of 7M modulated NiMnGa martensitic phase.” In: Acta Materialia 56.16 (2008), pp. 4529–4535. ISSN: 1359-6454.

[93] H. Yan, Y. Zhang, N. Xu, A. Senyshyn, H.-G. Brokmeier, C. Esling, X. Zhao, and L. Zuo. “Crystal structure determination of incommensurate modulated martensite in NiMnIn Heusler alloys.” In: Acta Materialia 88 (2015), pp. 375–388. ISSN: 1359-6454.

[94] K. Momma and F. Izumi. “VESTA3 for three-dimensional visualization of crystal, volumetric and morphology data.” In: Journal of Applied Crystallography 44.6 (2011), pp. 1272–1276.

[95] H. Gu, L. Bumke, C. Chluba, E. Quandt, and R. D. James. “Phase engineering and supercompatibility of shape memory alloys.” In: Materials Today 21.3 (2018), pp. 265–277. ISSN: 1369-7021.

[96] Z. Zhang, R. D. James, and S. Müller. “Energy barriers and hysteresis in martensitic phase transformations.” In: Acta Materialia 57.15 (2009), pp. 4332–4352. ISSN: 1359-6454.

[97] P. Devi, M. G. Zavareh, C. S. Mejía, K. Hofmann, B. Albert, C. Felser, M. Nicklas, and S. Singh. “Reversible adiabatic temperature change in the shape memory Heusler alloy Ni 2.2 Mn 0.8 Ga: An effect of structural compatibility.” In: Physical Review Materials 2.12 (2018), p. 122401.

[98] P. Devi, C. S. Mejía, M. G. Zavareh, K. K. Dubey, P. Kushwaha, Y. Skourski, C. Felser, M. Nicklas, and S. Singh. “Improved magnetostructural and magnetocaloric reversibility in magnetic Ni-Mn-In shape-memory Heusler alloy by optimizing the geometric compatibility condition.” In: Phys. Rev. Mater. 3 (6 2019), p. 062401.

[99] A. A. Mendonca, L. Ghivelder, P. L. Bernardo, H. Gu, R. D. James, L. F. Cohen, and A. M. Gomes. “Experimentally correlating thermal hysteresis and phase compatibility in multifunctional Heusler alloys.” In: Phys. Rev. Mater. 4 (11 2020), p. 114403.

[100] K. Dubey, P. Devi, A. K. Singh, and S. Singh. “Improved crystallographic compatibility and magnetocaloric reversibility in Pt substituted Ni2Mn1. 4In0. 6 magnetic shape memory Heusler alloy.” In: Journal of Magnetism and Magnetic Materials 507 (2020), p. 166818.

[101] T. Gottschall, E. Bykov, A. Gràcia-Condal, B. Beckmann, A. Taubel, L. Pfeuffer, O. Gutfleisch, L. Mañosa, A. Planes, Y. Skourski, and J. Wosnitza. “Advanced characterization of multicaloric materials in pulsed magnetic fields.” In: Journal of Applied Physics 127.18 (2020), p. 185107.

[102] B. Li, S. Li, B. Yang, H. Zhong, Z. Liu, and D. Li. “Enhancing the elastocaloric effect and thermal cycling stability in dendritic-like Ni50Mn31.6Ti18.4 single crystal.” In: Journal of Alloys and Compounds 936 (2023), p. 168310. ISSN: 0925-8388.

[103] Y. Du, M. Huang, S. Chang, D. L. Schlagel, T. A. Lograsso, and R. J. McQueeney. “Relation between Ga ordering and magnetostriction of Fe-Ga alloys studied by x-ray diffuse scattering.” In: Phys. Rev. B 81 (5 2010), p. 054432.

[104] Y. Du, M. Huang, T. A. Lograsso, and R. J. McQueeney. "X-ray diffuse scattering measurements of chemical short-range order and lattice strains in a highly magnetostrictive Fe0.813Ga0.187 alloy in an applied magnetic field." In: Phys. Rev. B 85 (21 2012), p. 214437.

[105] R. A. Laroche and S. Guruswamy. "Influence of Ga content and high temperature annealing on the short range order and magnetostriction of FeGa single crystals." In: Journal of Applied Physics 128.19 (2020), p. 195102. ISSN: 0021-8979.

[106] B. E. Warren. X-ray Diffraction. Courier Corporation, 1990.

[107] J. Als-Nielsen and D. McMorrow. Elements of modern X-ray physics. John Wiley & Sons, 2011.

[108] H. M. Rietveld. "A profile refinement method for nuclear and magnetic structures." In: Journal of Applied Crystallography 2.2 (1969), pp. 65–71.

[109] J. Rodríguez-Carvajal. "Recent advances in magnetic structure determination by neutron powder diffraction." In: Physica B: Condensed Matter 192.1 (1993), pp. 55–69. ISSN: 0921-4526.

[110] B. Fultz. Phase Transitions in Materials. Cambridge University Press, 2014.

[111] P. J. Webster. "Heusler alloys." In: Contemporary Physics 10.6 (1969), pp. 559–577.

[112] B. Henke, E. Gullikson, and J. Davis. "X-Ray Interactions: Photoabsorption, Scattering, Transmission, and Reflection at E = 50-30,000 eV, Z = 1-92." In: Atomic Data and Nuclear Data Tables 54.2 (1993), pp. 181–342. ISSN: 0092-640X.

[113] F. S. Varley. "Neutron scattering lengths and cross sectioirn." In: Neutron news 3.3 (1992), pp. 29–37.

[114] P. J. Brown, A. G. Fox, E. N. Maslen, M. A. OKeefe, and B. T. M. Willis. "Intensity of diffracted intensities." In: International Tables for Crystallography, Set, Volumes A - G, OnlineMRW. John Wiley & Sons, Ltd, 2006. Chap. 6.1, pp. 554–595. ISBN: 9780470685754.

[115] T. Welberry and T. Weber. "One hundred years of diffuse scattering." In: Crystallography Reviews 22.1 (2016), pp. 2–78.

[116] J. M. Cowley. "An Approximate Theory of Order in Alloys." In: Phys. Rev. 77 (5 1950), pp. 669–675.

[117] P. Singh, A. V. Smirnov, and D. D. Johnson. "Atomic short-range order and incipient long-range order in high-entropy alloys." In: Phys. Rev. B 91 (22 2015), p. 224204.

[118] P. Singh, A. Smirnov, A. Alam, and D. D. Johnson. "First-principles prediction of incipient order in arbitrary high-entropy alloys: exemplified in Ti0.25CrFeNiAlx." In: Acta Materialia 189 (2020), pp. 248–254. ISSN: 1359-6454.

[119] C. D. Woodgate and J. B. Staunton. "Short-range order and compositional phase stability in refractory high-entropy alloys via first-principles theory and atomistic modeling: NbMoTa, NbMoTaW, and VNbMoTaW." In: Phys. Rev. Mater. 7 (1 2023), p. 013801.

[120] W. A. Wooster. Diffuse X-ray reflections from crystals. Oxford University Press, 1962.

[121] K. Lonsdale. "Experimental study of x-ray scattering in relation to crystal dynamics." In: Reports on Progress in Physics 9.1 (1942), p. 256.

[122] M. Holt, Z. Wu, H. Hong, P. Zschack, P. Jemian, J. Tischler, H. Chen, and T.-C. Chiang. "Determination of Phonon Dispersions from X-Ray Transmission Scattering: The Example of Silicon." In: Phys. Rev. Lett. 83 (16 1999), pp. 3317–3319.

[123] R. Xu and T. C. Chiang. "Determination of phonon dispersion relations by x-ray thermal diffuse scattering." In: Zeitschrift für Kristallographie-Crystalline Materials 220.12 (2005), pp. 1009–1016.

[124] G. Wang, Y.-D. Wang, Y. Ren, D. Li, Y. Liu, and P. K. Liaw. "In-Situ High-Energy X-Ray Diffuse-Scattering Study of the Phase Transition of Ni 2 MnGa Single Crystal under High Magnetic Field." In: Metallurgical and Materials Transactions A 41 (2010), pp. 1269–1275.

[125] B. Wehinger, A. Bosak, K. Refson, A. Mirone, A. Chumakov, and M. Krisch. "Lattice dynamics of α-cristobalite and the Boson peak in silica glass." In: Journal of Physics: Condensed Matter 27.30 (2015), p. 305401.

[126] A. Bosak, D. Chernyshov, B. Wehinger, B. Winkler, M. L. Tacon, and M. Krisch. "In-between Bragg reflections: thermal diffuse scattering and vibrational spectroscopy with x-rays." In: Journal of Physics D: Applied Physics 48.50 (2015), p. 504003.

[127] B. Wehinger, A. Mirone, M. Krisch, and A. Bosak. "Full elasticity tensor from thermal diffuse scattering." In: Physical Review Letters 118.3 (2017), p. 035502.

[128] J. Büscher, A. Mirone, M. Stekiel, D. Spahr, W. Morgenroth, E. Haussühl, V. Milman, A. Bosak, O. Ivashko, M. von Zimmermann, A.-C. Dippel, and B. Winkler. "Elastic stiffness coefficients of thiourea from thermal diffuse scattering." In: Journal of Applied Crystallography 54.1 (2021), pp. 287–294.

[129] E. M. Schmidt, S. Thomas, J. M. Bulled, A. Minelli, and A. L. Goodwin. “Interplay of thermal diffuse scattering and correlated compositional disorder in KCl_1--xBr_x.” In: Acta Crystallographica Section B 78.3 Part 1 (2022), pp. 385–391.

[130] G. Fritsch, V. Kokorin, V. Chernenko, A. Kempf, and I. Zasimchuk. “Martensitic transformation in Ni-Mn-Ga alloys.” In: Phase Transitions: A Multinational Journal 57.4 (1996), pp. 233–240.

[131] M. Avdeev and J. R. Hester. “ECHIDNA: a decade of high-resolution neutron powder diffraction at OPAL.” In: Journal of Applied Crystallography 51.6 (2018), pp. 1597–1604.

[132] T. Faske and W. Donner. “X-ray diffractometer for the investigation of temperature- and magnetic field-induced structural phase transitions.” In: Journal of Applied Crystallography 51.3 (2018), pp. 761–767.

[133] A. Bergamaschi, A. Cervellino, R. Dinapoli, F. Gozzo, B. Henrich, I. Johnson, P. Kraft, A. Mozzanica, B. Schmitt, and X. Shi. “The MYTHEN detector for X-ray powder diffraction experiments at the Swiss Light Source.” In: Journal of synchrotron radiation 17.5 (2010), pp. 653–668.

[134] M. J. Buerger. “The Photography of the Reciprocal Lattice.” In: American Society of X-Ray and Electron Diffraction ASXRED Monograph No. 1 (1944).

[135] W. Kabsch. “xds.” In: Acta Crystallographica Section D: Biological Crystallography 66.2 (2010), pp. 125–132.

[136] A. Simonov. “Meerkat.” In: ETH Zurich, Switzerland 0.3.7. (2020).

[137] M. Jamal, S. Jalali Asadabadi, I. Ahmad, and H. Rahnamaye Aliabad. “Elastic constants of cubic crystals.” In: Computational Materials Science 95 (2014), pp. 592–599. ISSN: 0927-0256.

[138] P. Soven. “Coherent-potential model of substitutional disordered alloys.” In: Physical Review 156.3 (1967), p. 809.

[139] B. Gyorffy. “Coherent-potential approximation for a nonoverlapping-muffin-tin-potential model of random substitutional alloys.” In: Physical Review B 5.6 (1972), p. 2382.

[140] H. Ebert and et al. In: A spin polarized relativistic Korringa-Kohn-Rostoker (SPR-KKR) code for Calculating Solid State Properties, version 7.7 (), https://www.ebert.cup.uni–muenchen.de/kkr/.

[141] H. Ebert, D. Koedderitzsch, and J. Minar. “Calculating condensed matter properties using the KKR-Green’s function methodrecent developments and applications.” In: Reports on Progress in Physics 74.9 (2011), p. 096501.

[142] J. P. Perdew, K. Burke, and M. Ernzerhof. “Generalized gradient approximation made simple.” In: Physical Review Letters 77.18 (1996), p. 3865.

[143] A. I. Liechtenstein, M. Katsnelson, V. Antropov, and V. Gubanov. “Local spin density functional approach to the theory of exchange interactions in ferromagnetic metals and alloys.” In: Journal of Magnetism and Magnetic Materials 67.1 (1987), pp. 65–74.

[144] L. Vitos, H. L. Skriver, B. Johansson, and J. Kollár. “Application of the exact muffin-tin orbitals theory: the spherical cell approximation.” In: Computational materials science 18.1 (2000), pp. 24–38.

[145] L. Vitos, I. Abrikosov, and B. Johansson. “Anisotropic lattice distortions in random alloys from first-principles theory.” In: Physical Review Letters 87.15 (2001), p. 156401.

[146] L. Vitos. Computational quantum mechanics for materials engineers: the EMTO method and applications. Springer Science & Business Media, 2007.

[147] L. Vitos. “Total-energy method based on the exact muffin-tin orbitals theory.” In: Physical Review B 64.1 (2001), p. 014107.

[148] B. L. Gyorffy, A. J. Pindor, J. Staunton, G. M. Stocks, and H. Winter. “A first-principles theory of ferromagnetic phase transitions in metals.” In: Journal of Physics F: Metal Physics 15.6 (1985), pp. 1337–1386.

[149] D. Koch, B. Beckmann, N. M. Fortunato, O. N. Miroshkina, M. E. Gruner, H. Zhang, O. Gutfleisch, and W. Donner. “Chemical long range ordering in all-d-metal Heusler alloys.” In: Journal of Applied Physics 131.7 (2022), p. 073903.

[150] S. Wurmehl and M. Wójcik. “Structural Order in Heusler Compounds.” In: Heusler Alloys: Properties, Growth, Applications. Ed. by C. Felser and A. Hirohata. Cham: Springer International Publishing, 2016, pp. 87–109. ISBN: 978-3-319-21449-8.

[151] M. Zelený, A. Sozinov, L. Straka, T. Björkman, and R. M. Nieminen. “First-principles study of Co- and Cu-doped Ni_2MnGa along the tetragonal deformation path.” In: Phys. Rev. B 89 (18 2014), p. 184103.

[152] S. Barman, A. Chakrabarti, S. Singh, S. Banik, S. Bhardwaj, P. Paulose, B. Chalke, A. Panda, A. Mitra, and A. Awasthi. “Theoretical prediction and experimental study of a ferromagnetic shape memory alloy: Ga 2 MnNi.” In: Physical Review B 78.13 (2008), p. 134406.

[153] K. Liu, S. Ma, C. Ma, X. Han, K. Yu, S. Yang, Z. Zhang, Y. Song, X. Luo, C. Chen, S. U. Rehman, and Z. Zhong. "Martensitic transformation and giant magneto-functional properties in all-d-metal Ni-Co-Mn-Ti alloy ribbons." In: Journal of Alloys and Compounds 790 (2019), pp. 78–92. ISSN: 0925-8388.

[154] M. López-Cruz, J. Zamora, C. F. Sánchez-Valdés, and J. L. Sánchez Llamazares. "On the synthesis, structural transformation and magnetocaloric behavior of Ni37.5Co12.5 Mn35Ti15 melt-spun ribbons." In: AIP Advances 11.1 (2021), p. 015010.

[155] A. Cakir, L. Righi, F. Albertini, M. Acet, and M. Farle. "Intermartensitic transitions and phase stability in Ni50Mn50xSnx Heusler alloys." In: Acta Materialia 99 (2015), pp. 140–149. ISSN: 1359-6454.

[156] L. Vegard. "Die konstitution der mischkristalle und die raumfüllung der atome." In: Zeitschrift für Physik 5.1 (1921), pp. 17–26.

[157] V. V. Kokorin, V. A. Chernenko, E. Cesari, J. Pons, and C. Segui. "Pre-martensitic state in Ni - Mn - Ga alloys." In: Journal of Physics: Condensed Matter 8.35 (1996), p. 6457.

[158] S. Samanta, S. Chatterjee, S. Ghosh, and K. Mandal. "Large reversible magnetocaloric effect and magnetoresistance by improving crystallographic compatibility condition in Ni(Co)-Mn-Ti all-*d*-metal Heusler alloys." In: Phys. Rev. Mater. 6 (9 2022), p. 094411.

[159] H. Sepehri-Amin, A. Taubel, T. Ohkubo, K. Skokov, O. Gutfleisch, and K. Hono. "Microstructural origin of hysteresis in Ni-Mn-In based magnetocaloric compounds." In: Acta Materialia 147 (2018), pp. 342–349. ISSN: 1359-6454.

[160] Q. Zeng, J. Shen, H. Zhang, J. Chen, B. Ding, X. Xi, E. Liu, W. Wang, and G. Wu. "Electronic behaviors during martensitic transformations in all-d-metal Heusler alloys." In: Journal of Physics: Condensed Matter 31.42 (2019), p. 425401.

[161] I. B. Ramsteiner, A. Schöps, H. Reichert, H. Dosch, V. Honkimäki, Z. Zhong, and J. B. Hastings. "High-energy X-ray diffuse scattering." In: Journal of Applied Crystallography 42.3 (2009), pp. 392–400.

[162] M. J. Krogstad, P. M. Gehring, S. Rosenkranz, R. Osborn, F. Ye, Y. Liu, J. P. Ruff, W. Chen, J. M. Wozniak, H. Luo, et al. "The relation of local order to material properties in relaxor ferroelectrics." In: Nature Materials 17.8 (2018), pp. 718–724.

[163] L. Krause, K. Tolborg, T. B. E. Grønbech, K. Sugimoto, B. B. Iversen, and J. Overgaard. "Accurate high-resolution single-crystal diffraction data from a Pilatus3X CdTe detector." In: Journal of Applied Crystallography 53.3 (2020), pp. 635–649.

[164] O. Velikokhatnyi and I. Naumov. “Electronic structure and instability of Ni 2 MnGa.” In: Physics of the Solid State 41 (1999), pp. 617–623.

[165] C. Bungaro, K. M. Rabe, and A. D. Corso. “First-principles study of lattice instabilities in ferromagnetic Ni_2MnGa.” In: Phys. Rev. B 68 (13 2003), p. 134104.

[166] B. Wehinger, D. Chernyshov, M. Krisch, S. Bulat, V. Ezhov, and A. Bosak. “Diffuse scattering in Ih ice.” In: Journal of Physics: Condensed Matter 26.26 (2014), p. 265401.

[167] Y. M. Jin and Y. U. Wang. “Diffuse scattering intensity distribution associated with static and dynamic atomic position fluctuations.” In: JOM 64 (2012), pp. 161–166.

[168] X. Guo, Y. Ren, Y. M. Jin, and Y. U. Wang. “3D Diffuse Scattering and Displacement Short-Range Ordering in Pre-martensitic State: A Computational Study.” In: Shape Memory and Superelasticity (2023), pp. 1–13.

[169] H. Seiner, O. Heczko, P. Sedlák, L. Bodnárová, M. Novotný, J. Kopeek, and M. Landa. “Combined effect of structural softening and magneto-elastic coupling on elastic coefficients of NiMnGa austenite.” In: Journal of Alloys and Compounds 577 (2013). SI :ICOMAT2011, S131–S135. ISSN: 0925-8388.

[170] Q. Zhang, M. Qian, and X. Zhang. “Magneto-Structural Transition and Refrigeration Property in All-D-Metal Heusler Alloys: A Critical Review.” In: Journal of Solar Energy Research Updates 9 (2022), pp. 52–69.

[171] X. Moya, L. Mañosa, A. Planes, T. Krenke, M. Acet, V. O. Garlea, T. A. Lograsso, D. L. Schlagel, and J. L. Zarestky. “Lattice dynamics and phonon softening in $Ni-Mn-Al$ Heusler alloys.” In: Phys. Rev. B 73 (6 2006), p. 064303.

[172] S. Ener, J. Neuhaus, W. Petry, R. Mole, K. Hradil, M. Siewert, M. E. Gruner, P. Entel, I. Titov, and M. Acet. “Effect of temperature and compositional changes on the phonon properties of Ni-Mn-Ga shape memory alloys.” In: Phys. Rev. B 86 (14 2012), p. 144305.

[173] L. Mañosa, A. Planes, J. Zarestky, T. Lograsso, D. L. Schlagel, and C. Stassis. “Phonon softening in $Ni - Mn - Ga$ alloys.” In: Phys. Rev. B 64 (2 2001), p. 024305.

[174] M. Siewert, M. E. Gruner, A. Dannenberg, A. Hucht, S. M. Shapiro, G. Xu, D. L. Schlagel, T. A. Lograsso, and P. Entel. “Electronic structure and lattice dynamics of the magnetic shape-memory alloy Co_2NiGa.” In: Phys. Rev. B 82 (6 2010), p. 064420.

[175] B. Chakravarti, E. Starke, C. Sparks, and R. Williams. “Short range order and the development of long range order in Ni4Mo.” In: Journal of Physics and Chemistry of Solids 35.9 (1974), pp. 1317–1326. ISSN: 0022-3697.

[176] B. Schönfeld, G. Ice, C. Sparks, H.-G. Haubold, W. Schweika, and L. Shaffer. “X-ray study of diffuse scattering in Ni–20 at% Cr.” In: physica status solidi (b) 183.1 (1994), pp. 79–95.

[177] A. N. Khan, L. M. Moreno-Ramírez, Á. Díaz-García, J. Y. Law, and V. Franco. “All-d-metal Ni(Co)-Mn(X)-Ti (X = Fe or Cr) Heusler alloys: Enhanced magnetocaloric effect for moderate magnetic fields.” In: Journal of Alloys and Compounds 931 (2023), p. 167559. ISSN: 0925-8388.

[178] W. Ruland. “The separation of coherent and incoherent Compton X-ray scattering.” In: British Journal of Applied Physics 15.11 (1964), p. 1301.

[179] B. Schönfeld, C. R. Sax, J. Zemp, M. Engelke, P. Boesecke, T. Kresse, T. Boll, T. Al-Kassab, O. E. Peil, and A. V. Ruban. “Local order in Cr-Fe-Co-Ni: Experiment and electronic structure calculations.” In: Phys. Rev. B 99 (1 2019), p. 014206.

[180] P. Neibecker, M. Leitner, G. Benka, and W. Petry. “Increasing the achievable state of order in Ni-based Heusler alloys via quenched-in vacancies.” In: Applied Physics Letters 105.26 (2014), p. 261904. ISSN: 0003-6951.